

University of Alberta

**Surface Charge Heterogeneities and  
Shear-Induced Coalescence of Bitumen Droplets**

by

**Feng Lin**

A thesis submitted to the Faculty of Graduate Studies and Research in partial  
fulfillment of the requirements for the degree of

Doctor of Philosophy  
in  
Chemical Engineering

Department of Chemical and Materials Engineering

©Feng Lin  
Fall 2012  
Edmonton, Alberta

Permission is hereby granted to the University of Alberta Libraries to reproduce single copies of this thesis and to lend or sell such copies for private, scholarly or scientific research purposes only. Where the thesis is converted to, or otherwise made available in digital form, the University of Alberta will advise potential users of the thesis of these terms.

The author reserves all other publication and other rights in association with the copyright in the thesis and, except as herein before provided, neither the thesis nor any substantial portion thereof may be printed or otherwise reproduced in any material form whatsoever without the author's prior written permission.

For my loved parents

## Abstract

The coalescence of emulsified liquid drops is critically important to many separations processes. It is, for example, central to the extraction of bitumen (a form of extra heavy crude oil) from the Alberta oil sands. This research concerns the colloidal interactions between bitumen droplets in water, and how these interactions affect the coalescence of bitumen droplets under static (or at least quasi-static) and dynamic conditions. Experiments utilizing fine capillary pipettes were designed to create controlled *oblique shear contacts* involving a small oil drop (approx. 250  $\mu\text{m}$  in diameter) sliding along the surface of a much larger droplet (effectively a flat surface). Procedures were developed to allow direct quantification of the probabilities of coalescence between the two oil drops. The experimental parameters include: zeta potential ( $\zeta$ ) of the bitumen drops (through manipulation of solution pH and calcium ion concentration in the electrolyte), distance of shear contact, and shear speed. These parameters were varied to observe their effects on the probabilities of drop coalescence. Contrary to traditional DLVO theory, it was demonstrated that the coalescence of bitumen droplets was stochastic, and that the process can be characterized by only a probability. This probability of coalescence was shown to dramatically increase with larger contact areas and/or longer distances of shear (i.e. sliding) contact. Regarding the dynamics of contact, our results suggested that the probability of coalescence was slightly lowered with higher shear speeds. Experimental evidence from this study has pointed to significant departures from the classical DLVO theory, which predicts deterministic and contact-area-independent coalescence behaviors.

In addition, a theoretical model was developed to explain our observations. The proposed model adopts a statistical approach, combining familiar results of the DLVO theory (which is

deterministic in nature) with surface charge heterogeneities (SCH) introduced as the stochastic element. It was demonstrated that our proposed SCH model was remarkably successful in predicting both the trend *and* the magnitude of the observed coalescence probabilities under quasi-static shearing conditions. It was also shown that the aqueous phase pH not only affected the average zeta potential of the bitumen drops (something that is already known), but also modified the degree of surface charge heterogeneity (in the context of our SCH model). More precisely, an increase in pH of the aqueous solution led to two effects: (i) reduction in zeta potential uniformity (i.e. a larger standard deviation for the local  $\zeta$ ), and (ii) reduction in the size of the ‘domains’ over which local zeta potentials were effectively uniform. These two effects contributed to a more random distribution of zeta potentials on the bitumen droplet surfaces. Ultimately, it is the randomness of  $\zeta$ -potential, together with its average value (measured, for example, by electrophoresis), that determine the probability of bitumen droplet coalescence.

Finally, the validity of our theoretical model was verified by directly mapping surface charge heterogeneities at the bitumen-water interface using atomic force microscopy (AFM). Local zeta potentials were obtained from force curves quantified at different locations, and the results clearly indicated that charges on the bitumen-water interface were heterogeneously distributed. In addition, it was found that the average zeta potential and the important charge heterogeneity parameter (namely, the local domain size), as determined by direct AFM measurements, were comparable to those obtained based on the SCH model (i.e. from fitting the SCH model to observed coalescence probabilities).

## **Acknowledgements**

First of all, I would like to express my sincere gratitude and appreciation to my supervisor, Dr. Anthony Yeung. His invaluable guidance, encouragement and inspiration, together with his sharp insight into interfacial science, deeply motivated me throughout this research and will continue to influence on me in the long run.

I am indebted to Drs. Qi Liu, Hongbo Zeng, Tian Tang, and Boxin Zhao for their reviewing my thesis and constructive comments. Many thanks are extended to Payman, Lili, Mehdi, Amin and other members of our research group, for their selfless help and enjoyable discussions during my research work. Special thanks to Saina and Mohammad for their friendship and assistance. I also take this opportunity to acknowledge Drs. Anqiang He and Jun Long for their willingness to provide me technical training of AFM instrument and to answer many of my “dumb questions.”

And, I could not complete this thesis without plentiful support from my family, especially my beautiful wife and daughter for their endless love without asking for anything in return.

I am also deeply thankful to the financial supports from Syncrude Canada Ltd, University of Alberta Provost Doctoral Entrance Award, and Profiling Alberta's Graduate Students Award.

# Table of Content

<b>Chapter 1: Introduction.....</b>	<b>1</b>
<b>1.1 Oil sands.....</b>	<b>1</b>
<b>1.2 Bitumen extraction.....</b>	<b>3</b>
<b>1.3 Problem definition.....</b>	<b>9</b>
<b>1.4 Specific objectives.....</b>	<b>12</b>
<b>1.5 Document layout.....</b>	<b>13</b>
<b>Chapter 2: Literature Review.....</b>	<b>15</b>
<b>2.1 Colloidal Interactions.....</b>	<b>15</b>
2.1.1 Van der Waals (VDW) interactions.....	16
2.1.1.1 Molecular origins of VDW interactions.....	17
2.1.1.2 VDW interactions between colloidal particles.....	18
2.1.2 Electrostatic interactions.....	19
2.1.2.1 Origin of surface charge.....	19
2.1.2.2 Electric Double Layer (EDL).....	20
2.1.2.3 Zeta ( $\zeta$ ) potential.....	24
2.1.2.4 EDL interactions between two planar surfaces.....	26
2.1.3 Classical DLVO theory.....	30
2.1.4 More recent developments.....	33
2.1.4.1 Surface heterogeneities.....	33
2.1.4.1.1 Effect of surface roughness on DLVO interactions.....	33
2.1.4.1.2 Effect of charge heterogeneity on DLVO interactions.....	36
2.1.4.2 Non-DLVO forces.....	42
<b>2.2 Aggregation kinetics.....</b>	<b>44</b>
2.2.1 Collision frequency.....	44
2.2.2 Collision efficiency.....	47
<b>2.3 Studies on bitumen coalescence.....</b>	<b>49</b>
2.3.1 Prediction from classical DLVO theory.....	52
2.3.2 Surface charge heterogeneity model.....	61
<b>Chapter 3: Experimental.....</b>	<b>67</b>
<b>3.1 Materials.....</b>	<b>67</b>
<b>3.2 Micropipette technique.....</b>	<b>68</b>
3.2.1 Introduction of micropipette.....	68
3.3.2 Suspension preparation.....	70
3.3.3 Oblique contact experiment.....	71
<b>3.3 Atomic Force Microscopy (AFM) technique.....</b>	<b>72</b>
3.3.1 Introduction of AFM.....	73
3.3.2 Bitumen substrate preparation.....	78
3.3.3 Force mapping measurements.....	82

<b>3.4 Electrophoresis technique .....</b>	<b>83</b>
3.4.1 Introduction of electrophoresis .....	83
3.4.2 Suspension preparation .....	85
3.4.3 Zeta potentials measurement.....	86
<b>Chapter 4 : Results and discussion.....</b>	<b>87</b>
<b>4.1 Determining average <math>\zeta</math> potentials of suspended particles in electrolytes with</b>	
<b>ZetaPALS .....</b>	<b>87</b>
4.1.1 Bitumen-in-water suspensions .....	87
4.1.2 Si <sub>3</sub> N <sub>4</sub> -in-water suspensions .....	90
<b>4.2 Quantifying shear-induced coalescence of bitumen droplets in water with</b>	
<b>micropipette .....</b>	<b>93</b>
4.2.1 General observations.....	93
4.2.2 Constant shear distance.....	96
4.2.3 Constant shear speed.....	98
4.2.4 Data fitting and interpretation.....	103
<b>4.3 Ascertaining surface charge heterogeneity on bitumen-water interface with</b>	
<b>AFM.....</b>	<b>119</b>
4.3.1 Colloidal force mapping and calculated surface charge distributions .....	119
4.3.2 Autocorrelation functions of heterogeneous charge distributions .....	130
4.3.3 Comparison between heterogeneous parameters obtained in two approaches.....	140
<b>Chapter 5 : Conclusions and Recommendations .....</b>	<b>142</b>
<b>References:.....</b>	<b>145</b>
<b>Appendix A: Contact mechanics of two distinctly-sized droplets pressed together in</b>	
<b>oblique contact experiments.....</b>	<b>155</b>
<b>Appendix B: AFM force analysis.....</b>	<b>157</b>
<b>Appendix C: Theoretical equations of DLVO forces between the AFM tip and the</b>	
<b>bitumen substrate in a SPW electrolyte.....</b>	<b>160</b>
<b>Appendix D: Note on the Ornstein-Uhlenbeck Process.....</b>	<b>162</b>

## List of Tables

Table 4-1:	The two modeling parameters $\sigma_\zeta$ and $L$ obtained with best fitted to the corresponding experimental data by assuming their primary dependence on $[\text{Ca}^{2+}]$ .....	107
Table 4-2:	The effect of pH on the two modeling parameters $\sigma_\zeta$ and $L$ . Those parameters were obtained with best fitted to the corresponding experimental data by assuming their primary dependence on pH.....	112
Table 4-3:	Summary of the two parameters calculated from local $\zeta$ -Potentials data and correlogram charts with repeated sets of experiments at different pH values. Here, the mean value $\zeta_{ave}$ of the $\zeta$ potential signals was calculated from the signal data in Figure 4-20 to Figure 4-22, and the correlation length $\lambda$ was approximately equivalent to the decay constant of the fitted exponential equation to the ACF data in Figures 4-23 through 4-25. ....	139
Table 4-4:	Comparison between the two parameters based on two different approaches of quantifying surface charge heterogeneity on the bitumen droplet immersed in the SPW electrolyte in absence of calcium ion at different pH values. Here, the parameters of model were quoted from the Figure 4-1 and Table 4-2, being fit to the oblique contact experiments. The parameters of AFM study were collected from the Table 4-3.....	139

## List of Figures

Figure 1-1: A generalized scheme for water-based bitumen extraction process for the surface mined oil sands .....	9
Figure 2-1: The three proposing models for an Electrical Double Layer (EDL): (a) Helmholtz model, (b) Gouy-Chapman model, and (c) Stern-Grahame model....	23
Figure 2-2: The three potential distributions leading to the same $\zeta$ -potential, however, the state of the interface and the inner stern layer is vastly different in the three types of ions: (a) potential determining ions; (b) indifferent electrolytes; (c) specifically adsorbed ions. Here, the horizontal axis represents the distance away from the particle surface and the vertical axis shows the potential [Adapted from Hunter 1981].....	26
Figure 2-3: Schematic representation of the change in potential distribution when two similar planar surfaces approach to the distance of separation $h$ . $\psi_{h/2}$ is the potential at the mid-plane. [Adapted from Hunter 1986].....	27
Figure 2-4: Typical image of showing two bitumen droplets ( $\sim 0.1$ and $1$ mm in radius) pressed together using micropipettes. The suspending medium is “simulated process water” (SPW) of varying $[Ca^{2+}]$ and pH. The amount of deformation of the droplets, shear distance and shear speed can be precisely controlled. This typical “oblique” (or sliding) contact may or may not result in the coalescence of the droplets; the process is, in essence, stochastic.....	53
Figure 2-5: Series of curves showing colloidal forces ( $F$ , in unit of $\mu N$ ) versus distance ( $h$ , in nm) between two distinct bitumen spheres (with radii $0.1$ mm and $1$ mm) in aqueous electrolytes ( $\kappa^{-1}=1.45$ nm). The calculation is based on classical DLVO theory using eqn 2.28. Zeta potentials of bitumen droplets $\zeta_1$ and $\zeta_2$ are the only adjustable parameters. $F > 0$ implies a net repulsion, while $F < 0$ denotes attraction. The insert shows the very weak attractive force (secondary force minimum) at very large distances. The peaks of the two force curves (approx. $103$ nN in case b; $6 \times 10^3$ nN in case a) are the two extreme force barriers that must be overcome for coalescence to occur in the current problem. The curves (a) and (b) are plotted using the minimum and maximum absolute values of zeta potentials of bitumen droplets in simulated process water (see Chapter 4). In order to overcome the force barrier, which is shown in curve c, the zeta potentials of opposing surfaces must satisfy equation 2.33 in which $(\zeta_1 \zeta_2)^{1/2} < 8.2$ mV.....	57
Figure 2-6: Schematic of modeling (b) heterogeneously distributed charges on surface of a bitumen sphere containing (a) surface-averaged potential $\zeta_{ave}$ . Each patch possesses unique local zeta potential ( $\zeta_i$ ) for characteristic length scale ( $L$ ). The value $\zeta_{ave}$ can be determined from electrophoresis (see Chapter 3 for detailed procedure and Chapter 4 for results).....	61
Figure 2-7: The 3D picture depicts the probability density function of two Gaussian variables. The horizontal axes are $\zeta_1$ and $\zeta_2$ denoting the zeta potentials of the two interacting patches, and the vertical axis is $f(\zeta_1 \zeta_2)$ signifying the joint probability density function quoted in eqn. 2.34. The red hyperbola line sketches the local destabilization criterion quoted in eqn 2.33. The volume under the joint	

	probability density within the red hyperbolic region is regarded as the local probability ( $\phi$ ) of coalescence. (Adapted from Esmaeili et al. 2012).....	63
Figure 3-1:	Schematics of the micropipette experimental setup. The bitumen-in-water suspension is placed in the glass cell (as illustrated in the blown-up view). Two individual bitumen droplets are grasped and controlled precisely into oblique contact by the micromanipulators.....	70
Figure 3-2:	Schematics of an Atomic Force Microscope. (Adapted from Butt et al. 2003).....	74
Figure 3-3:	Typical AFM force curves: (a) photodiode current vs piezo-displacement curves, recorded from AFM; (b) force vs distance curves, converted from (a).....	77
Figure 3-4:	XPS spectra of (A): the clean silicon substrate (black line) and (B): the bitumen-coated silicon substrate (red line). A blow-up view of sulfur-element peaks is also included.....	80
Figure 3-5:	A typical three-dimensional image of the $20\mu\text{m} \times 20\mu\text{m}$ area of bitumen substrate in a SPW electrolyte obtained with tapping mode. Image with $256 \times 256$ resolutions was captured with using a Veeco SNP-10 cantilever at a scan rate of 1 Hz. The manufacturer-given data of the cantilever shows a spring constant of 0.58 N/m, a tip with radius of curvature of about 10 nm, and a resonance frequency in air of about 60 kHz. The resonance frequency of the cantilever in an electrolyte was about 30-50 % of the value in air. The cantilever was cleaned by UV irradiation for at least 2 hours and the bitumen substrate was immersed in the electrolyte for at least 30 min prior to imaging.....	81
Figure 3-6:	Schematic of ZetaPALS analyzer. [Adapted from Instruction Manual].....	84
Figure 4-1:	$\zeta$ -potentials of suspended bitumen droplets in the SPW-based aqueous solutions at different pH and $[\text{Ca}^{2+}]$ . The potentials were measured using electrophoresis. The experiments were conducted at room temperature. The average size of bitumen droplet was estimated to be of order $1\mu\text{m}$ .....	89
Figure 4-2:	Comparison of surface potentials of Si <sub>3</sub> N <sub>4</sub> in 1mM KCl solution of varying pH in this study with similar value reported in literature [Yin & Drelich 2008]. We measured the electrophoretic mobility of powdered Si <sub>3</sub> N <sub>4</sub> as received and calculated the surface potentials (shown in the square symbols with error bars) assuming the zeta potentials as surface potentials. Yin & Drelich measured the Si <sub>3</sub> N <sub>4</sub> - Si <sub>3</sub> N <sub>4</sub> colloidal forces using AFM and curve fitted them to obtain surface charge densities and zeta potentials, which are shown in the solid line with small dots.....	91
Figure 4-3:	Surface potentials of Si <sub>3</sub> N <sub>4</sub> powders in SPW-based aqueous electrolytes of varying pH in absence of calcium ion, assuming equality between $\zeta$ potentials and surface potentials. The potentials were measured using electrophoretic experiments. The experiments were conducted at room temperature. The average bitumen droplet size was estimated to be of about $1\mu\text{m}$ .....	92
Figure 4-4:	Series of photos showing oblique contact experiments between bitumen droplets. The experimental conditions in the left and right columns were identical: the medium was SPW in absence of $\text{Ca}^{2+}$ ; the temperature of medium was 22°C; distance and speed of shear contact were controlled at $100\mu\text{m}$ and $150\mu\text{m/s}$ , respectively; the sizes of small and large drops were around $250\mu\text{m}$ and $2.5\text{mm}$ ; the deformation ratio of small drop was 1.1. Nevertheless, the outcomes of the	

	two contact events were different: coalescence occurred on the left, but not on the right (despite sweeping the small droplet multiple times over the big drop).....	95
Figure 4-5:	Experimental probability of bitumen coalescence as function of shear speed. The electrolyte medium was SPW in the absence of $\text{Ca}^{2+}$ ions and at pH = 8. The temperature of medium was 22°C; the size of the small droplet was around 250 $\mu\text{m}$ , and the larger drop was 2.5 mm. The deformation ratio of the small droplet was 1.1.....	97
Figure 4-6:	Experimental probability of coalescence between bitumen droplets as function of shear distance. The electrolyte media were SPW solutions at pH = 10 with varying $[\text{Ca}^{2+}] = 0, 0.1, \text{ and } 0.5 \text{ mM}$ ; the speed of shear was held constant at 1.5 $\mu\text{m/s}$ ; the temperature of media was 22°C; the size of small droplet was around 250 $\mu\text{m}$ , and the larger one 2.5 mm; the deformation ratio of the small droplet was 1.1.....	100
Figure 4-7:	Experimental probability of coalescence between bitumen droplets as function of shear distance. The electrolyte media were SPW solutions at pH = 8 with varying $[\text{Ca}^{2+}] = 0, 0.1, \text{ and } 0.5 \text{ mM}$ ; the speed of shear was held constant at 1.5 $\mu\text{m/s}$ ; the temperature of media was 22°C; the size of small droplet was around 250 $\mu\text{m}$ , and the larger one 2.5 mm; the deformation ratio of the small droplet was 1.1.....	101
Figure 4-8:	Experimental probability of coalescence between bitumen droplets as function of shear distance. The electrolyte media were SPW solutions at pH = 6 with varying $[\text{Ca}^{2+}] = 0, 0.1, \text{ and } 0.5 \text{ mM}$ ; the speed of shear was held constant at 1.5 $\mu\text{m/s}$ ; the temperature of media was 22°C; the size of small droplet was around 250 $\mu\text{m}$ , and the larger one 2.5 mm; the deformation ratio of the small droplet was 1.1.....	102
Figure 4-9:	Bitumen coalescence probability $\Phi$ as function of surface-averaged zeta potential $\zeta_{\text{ave}}$ (in magnitude) with varying shear distance H. Here, the symbols are experimental results of coalescence probabilities (also see Figure 4-6 to 4-8); different symbols correspond to different shear distances $\blacklozenge$ : H = 0, $\blacktriangle$ : H = 50 $\mu\text{m}$ , $\bullet$ : H = 100 $\mu\text{m}$ , $\times$ : H = 200 $\mu\text{m}$ . The solid lines are theoretical model predictions based on the two fitting parameters: $\sigma_{\zeta} = 30 \text{ mV}$ and $L = 0.6 \mu\text{m}$ . The fitting was based on the assumption that these parameters are independent of both pH and $[\text{Ca}^{2+}]$ . The magnitude of $\zeta_{\text{ave}}$ were controlled by the two variables pH and $[\text{Ca}^{2+}]$ , see Figure 4-1. The background electrolytes were SPW solutions with varying $\text{Ca}^{2+}$ addition and pH; temperature of media was 22°C; the speed of shear was controlled at 1.5 $\mu\text{m/s}$ ; the size of small drop was around 250 $\mu\text{m}$ , larger one 2.5 mm, the deformation ratio of small drop was 1.1.....	108
Figure 4-10:	Bitumen coalescence probability $\Phi$ as function of shear distance H in the SPW background electrolytes with varying pH values at fixed $[\text{Ca}^{2+}] = 0$ . The symbols are experimental results of coalescence probabilities; different symbols correspond to different pH conditions $\blacklozenge$ : pH = 6, $\blacksquare$ : pH = 8, $\blacktriangle$ : pH = 10. The solid lines are theoretical modeling predictions based on the two fitting parameters: $\sigma_{\zeta} = 28 \text{ mV}$ ; $L = 1 \mu\text{m}$ ; the fitting was based on the assumption that these parameters were dependent on $[\text{Ca}^{2+}]$ but independent on pH. The temperature of electrolyte media	

was 22oC; the speed of shear was controlled at 1.5  $\mu\text{m/s}$ ; the size of small droplet was around 250  $\mu\text{m}$ , larger one 2.5 mm, the deformation ratio of small droplet was 1.1.....109

Figure 4-11: Bitumen coalescence probability  $\Phi$  as function of shear distance H in the SPW background electrolytes with varying pH values at fixed  $[\text{Ca}^{2+}] = 0.1 \text{ mM}$ . The symbols are experimental results of coalescence probabilities; different symbols correspond to different pH conditions  $\blacklozenge$ : pH = 6,  $\blacksquare$ : pH = 8,  $\blacktriangle$ : pH = 10. The solid lines are theoretical modeling predictions based on the two fitting parameters:  $\sigma_{\zeta} = 25 \text{ mV}$ ;  $L = 0.14 \mu\text{m}$ ; the fitting was based on the assumption that these parameters were dependent on  $[\text{Ca}^{2+}]$  but independent on pH. The temperature of electrolyte media was 22oC; the speed of shear was controlled at 1.5  $\mu\text{m/s}$ ; the size of small droplet was around 250  $\mu\text{m}$ , larger one 2.5 mm, the deformation ratio of small droplet was 1.1.....110

Figure 4-12: Bitumen coalescence probability  $\Phi$  as function of shear distance H in the SPW background electrolytes with varying pH values at fixed  $[\text{Ca}^{2+}] = 0.5 \text{ mM}$ . The symbols are experimental results of coalescence probabilities; different symbols correspond to different pH conditions  $\blacklozenge$ : pH = 6,  $\blacksquare$ : pH = 8,  $\blacktriangle$ : pH = 10. The solid lines are theoretical modeling predictions based on the two fitting parameters:  $\sigma_{\zeta} = 25 \text{ mV}$ ;  $L = 0.14 \mu\text{m}$ ; the fitting was based on the assumption that these parameters were dependent on  $[\text{Ca}^{2+}]$  but independent on pH. The temperature of electrolyte media was 22oC; the speed of shear was controlled at 1.5  $\mu\text{m/s}$ ; the size of small droplet was around 250  $\mu\text{m}$ , larger one 2.5 mm, the deformation ratio of small droplet was 1.1.....111

Figure 4-13: Bitumen coalescence probability  $\Phi$  as function of shear distance H in the SPW background electrolytes with varying  $[\text{Ca}^{2+}]$  values at fixed pH = 6. The symbols are experimental results of coalescence probabilities; different symbols correspond to different  $[\text{Ca}^{2+}]$  conditions  $\blacklozenge$ :  $[\text{Ca}^{2+}] = 0$ ,  $\blacksquare$ :  $[\text{Ca}^{2+}] = 0.1 \text{ mM}$ ,  $\blacktriangle$ :  $[\text{Ca}^{2+}] = 0.5 \text{ mM}$ . The solid lines are theoretical modeling predictions based on the two fitting parameters:  $\sigma_{\zeta} = 24 \text{ mV}$ ;  $L = 1 \mu\text{m}$ ; the fitting was based on the assumption that these parameters were dependent on pH but independent on  $[\text{Ca}^{2+}]$ . The temperature of electrolyte media was 22oC; the speed of shear was controlled at 1.5  $\mu\text{m/s}$ ; the size of small droplet was around 250  $\mu\text{m}$ , larger one 2.5 mm, the deformation ratio of small droplet was 1.1.....113

Figure 4-14: Bitumen coalescence probability  $\Phi$  as function of shear distance H in the SPW background electrolytes with varying  $[\text{Ca}^{2+}]$  values at fixed pH = 8. The symbols are experimental results of coalescence probabilities; different symbols correspond to different  $[\text{Ca}^{2+}]$  conditions  $\blacklozenge$ :  $[\text{Ca}^{2+}] = 0$ ,  $\blacksquare$ :  $[\text{Ca}^{2+}] = 0.1 \text{ mM}$ ,  $\blacktriangle$ :  $[\text{Ca}^{2+}] = 0.5 \text{ mM}$ . The solid lines are theoretical modeling predictions based on the two fitting parameters:  $\sigma_{\zeta} = 26 \text{ mV}$ ;  $L = 0.7 \mu\text{m}$ ; the fitting was based on the assumption that these parameters were dependent on pH but independent on  $[\text{Ca}^{2+}]$ . The dashed lines are theoretical modeling predictions based on the values of three parameters ( $\sigma_{\zeta}$ ,  $L$ , and  $\zeta_{ave}$ ) obtained previously by Esmaeili et al. 2010.

The temperature of electrolyte media was 22oC; the speed of shear was controlled at 1.5  $\mu\text{m/s}$ ; the size of small droplet was around 250  $\mu\text{m}$ , larger one 2.5 mm, the deformation ratio of small droplet was 1.1.....114

Figure 4-15: Bitumen coalescence probability  $\Phi$  as function of shear distance  $H$  in the SPW background electrolytes with varying  $[\text{Ca}^{2+}]$  values at fixed  $\text{pH} = 10$ . The symbols are experimental results of coalescence probabilities; different symbols correspond to different  $[\text{Ca}^{2+}]$  conditions  $\blacklozenge$ :  $[\text{Ca}^{2+}] = 0$ ,  $\blacksquare$ :  $[\text{Ca}^{2+}] = 0.1 \text{ mM}$ ,  $\blacktriangle$ :  $[\text{Ca}^{2+}] = 0.5 \text{ mM}$ . The solid lines are theoretical modeling predictions based on the two fitting parameters:  $\sigma_{\zeta} = 28 \text{ mV}$ ;  $L = 0.3 \mu\text{m}$ ; the fitting was based on the assumption that these parameters were dependent on  $\text{pH}$  but independent on  $[\text{Ca}^{2+}]$ . The temperature of electrolyte media was 22oC; the speed of shear was controlled at 1.5  $\mu\text{m/s}$ ; the size of small droplet was around 250  $\mu\text{m}$ , larger one 2.5 mm, the deformation ratio of small droplet was 1.1.....115

Figure 4-16: Examples of force-distance curves obtained at different tip locations on the bitumen surface in the SPW electrolyte without calcium ion at  $\text{pH} = 6$ . Here, symbols represent the converted force data from AFM measurements; the cantilever tip with a manufacturer's nominal spring constant of 0.12 N/m was used. Solid lines show the theoretical fitting plots based on the DLVO equation of constant charge boundary condition in eqn (C.2) of Appendix C; the surface potential and charge density were related by the Grahame equation (C.3), the values of the related fitting parameters are given as follows: radius of the tip end  $r_s = 10 \text{ nm}$ , angle for the tip  $\beta = 10^\circ$ , Debye length  $\kappa^{-1} = 1.45 \text{ nm}$ , Hamaker constant  $A_{123} = 2.7 \times 10^{-20} \text{ J}$ , surface potential of the tip  $\zeta_1 = -36.6 \text{ mV}$ , surface potentials of bitumen  $\zeta_2$  are respectively shown in the graph.....121

Figure 4-17: Examples of force-distance curves obtained at different tip locations on the bitumen surface in the SPW electrolyte without calcium ion at  $\text{pH} = 8$ . Here, symbols represent the converted force data from AFM measurements; the cantilever tip with a manufacturer's nominal spring constant of 0.58 N/m was used. Solid lines show the theoretical fitting plots based on the DLVO equation of constant charge boundary condition in eqn (C.2) of Appendix C; the surface potential and charge density were related by the Grahame equation (C.3), the values of the related fitting parameters are given as follows: radius of the tip end  $r_s = 10 \text{ nm}$ , angle for the tip  $\beta = 10^\circ$ , Debye length  $\kappa^{-1} = 1.45 \text{ nm}$ , Hamaker constant  $A_{123} = 2.7 \times 10^{-20} \text{ J}$ , surface potential of the tip  $\zeta_1 = -52.7 \text{ mV}$ , surface potentials of bitumen  $\zeta_2$  are respectively shown in the graph..... 122

Figure 4-18: Examples of force-distance curves obtained at different tip locations on the bitumen surface in the SPW electrolyte without calcium ion at  $\text{pH} = 10$ . Here, symbols represent the converted force data from AFM measurements; the cantilever tip with a manufacturer's nominal spring constant of 0.58 N/m was used. Solid lines show the theoretical fitting plots based on the DLVO equation of constant charge boundary condition in eqn (C.2) of Appendix C; the surface potential and charge density were related by the Grahame equation (C.3), the values of the related fitting parameters are given as follows: radius of the tip end

$r_s = 10$  nm, angle for the tip  $\beta = 10^\circ$ , Debye length  $\kappa^{-1} = 1.45$  nm, Hamaker constant  $A_{123} = 2.7 \times 10^{-20}$  J, surface potential of the tip  $\zeta_1 = -64.5$  mV, surface potentials of bitumen  $\zeta_2$  are respectively shown in the graph.....123

Figure 4-19: The ten examples of force-distance curves obtained at the same tip locations on the bitumen surface in the SPW electrolyte without calcium ion at pH = 8. Here, symbols represent the converted force data from at least 10 AFM measurements; the cantilever tip with a manufacturer’s nominal spring constant of 0.58 N/m was used. Solid lines show the theoretical fitting plots based on the DLVO equation of constant charge boundary condition in eqn (C.2) of Appendix C; the surface potential and charge density were related by the Grahame equation (C.3), the values of the related fitting parameters are given as follows: radius of the tip end  $r_s = 10$  nm, angle for the tip  $\beta = 10^\circ$ , Debye length  $\kappa^{-1} = 1.45$  nm, Hamaker constant  $A_{123} = 2.7 \times 10^{-20}$  J, surface potential of the tip  $\zeta_1 = -52.7$  mV, surface potentials of bitumen  $\zeta_2$  are respectively shown in the graph. These curves indicate that less than 20 % variations of colloidal forces (around 5 % changes in surface potentials) were commonly observed in the AFM measurements repeated on the same substrate location.....124

Figure 4-20 (a) and (b): The two plots of random potential signal from bitumen-water interface at pH = 6 (SPW,  $[Ca^{2+}] = 0$ ). The x-axis represents the lateral position of bitumen sample relative to the AFM tip (40 nm per step offset adjustment); y-axis is the local potential, which is determined by the parameter to be fit AFM-obtained force vs. separation curve at a local position, assuming that  $\zeta$  equals to surface potential.....126

Figure 4-21 (a) - (d): The four plots of random potential signal from bitumen-water interface at pH = 8 (SPW,  $[Ca^{2+}] = 0$ ). The x-axis represents the lateral position of bitumen sample relative to the AFM tip (40 nm per step offset adjustment); y-axis is the local potential, which is determined by the parameter to be fit AFM-obtained force vs. separation curve at a local position, assuming that  $\zeta$  equals to surface potential.....128

Figure 4-22 (a) and (b): The two plots of random potential signal from bitumen-water interface at pH = 10 (SPW,  $[Ca^{2+}] = 0$ ). The x-axis represents the lateral position of bitumen sample relative to the AFM tip (40 nm per step offset adjustment); y-axis is the local potential, which is determined by the parameter to be fit AFM-obtained force vs. separation curve at a local position, assuming that  $\zeta$  equals to surface potential.....129

Figure 4-23 (a) and (b): The two correlograms of random  $\zeta$  potential signal from bitumen-water interface at pH = 6 (SPW,  $[Ca^{2+}] = 0$ ), in which the series of the autocorrelation function (ACF) values were plotted against the location displacement (x). Here, symbol points represent the calculated ACF data from the AFM study; solid lines show the fitted exponential decay functions. The decay lengths of the fitted equations were listed in Table 4-3.....134

Figure 4-24 (a) - (d): The four correlograms of random  $\zeta$  potential signal from bitumen-water interface at pH = 8 (SPW,  $[Ca^{2+}] = 0$ ), in which the series of the autocorrelation function (ACF) values were plotted against the location displacement (x). Here, symbol points represent the calculated ACF data from the AFM study; solid lines

	show the fitted exponential decay functions. The decay lengths of the fitted equations were listed in Table 4-3.....	136
Figure 4-25	(a) and (b): The two correlograms of random $\square$ potential signal from bitumen-water interface at pH = 10 (SPW, $[Ca^{2+}] = 0$ ), in which the series of autocorrelation function (ACF) values were plotted against the location displacement (x). Here, symbol points represent the calculated ACF data from the AFM study; solid lines show the fitted exponential decay functions. The decay lengths of the fitted equations were listed in Table 4-3.....	137
Figure 4-26	(a) and (b): The two examples of showing the effect of the number of processing data on the correlogram of Ornstein-Uhlenbeck (OU) signal. The formula of OU signal is shown in the equation (D.2) in Appendix D. Here, symbols represent the calculated ACF data from the same OU signal with increasing number of processing data while keeping interval of steps the same (= 40 nm); “*”: 51 points, “+”: 501 points, “ $\square$ ”: 5001 points. Solid lines show the fitted exponential decayed function.....	138
Figure A-1:	Depiction of the droplet shape profile in this study. A spherical drop (representing a small drop), held by a suction pipette, is brought against a planar surface in red (modeling a much bigger drop).....	156
Figure B-1:	Schematic of graphs showing the conversion procedure of a force curve obtained by AFM.....	159
Figure C-1:	Geometry of the system where the cantilever tip interacts with the flat substrate.....	161

## Nomenclature

$A$	Hamaker constant (J)
$AC$	Area of droplet-droplet contact ( $\text{m}^2$ )
$ACF$	Autocorrelation function of local potentials (-)
$C$	Intermolecular energy coefficient ( $\text{J}\cdot\text{m}^4$ )
$c$	Concentration of the electrolyte ( $\text{mol}/\text{m}^3$ )
$Cov$	Auto-covariance coefficient of local potentials ( $\text{V}^2$ )
$d$	Diameter of the particle (m)
$DR$	Deformation ratio of the particle (-)
$E$	Strength of electric field ( $\text{V}/\text{m}$ )
$e$	Fundamental electrical charge (J)
$F$	Force (N)
$f$	Joint probability density function (-)
$fc$	Frequency of collision ( $\text{m}^{-3}\text{s}^{-1}$ )
$fr$	Fraction of the charged region (-)
$G$	Shear rate ( $\text{s}^{-1}$ )
$g$	Acceleration due to gravity ( $\text{m}/\text{s}^2$ )
$H$	Distance of shear contact (m)
$h$	Distance of separation (m)
$I$	Ionic strength of electrolyte ( $\text{mol}/\text{L}$ )
$I$	Photodiode current (V)
$K$	Collision constant ( $\text{m}^{-3}\text{s}^{-1}$ )
$k_B$	Boltzman constant (J/K)
$k_c$	Spring constant of the cantilever (N/m)
$L$	Patch size (m)
$n$	Number concentration of ion ( $1/\text{m}^3$ )
$n^0$	Number concentration of ion in bulk ( $1/\text{m}^3$ )
$p$	Pressure (Pa)
$q$	Strength of dipole charge (V)
$r$	Radius of spherical droplet or segment (m)

$T$	Absolute temperature ( $^{\circ}\text{C}$ )
$U$	Electrophoretic velocity of particle (m/s)
$V$	Interaction energy per unit area ( $\text{J}/\text{m}^2$ )
$W$	Stability ratio (-)
$z$	Valence of the ion specie (-)
$Z_p$	Displacement of piezo (m)
$Z_c$	Deflection of cantilever (m)

### **Greek**

$\alpha$	Geometrical angle of cantilever tip (-)
$\beta$	Geometrical angle of cantilever tip (-)
$\chi$	Collision efficiency (-)
$\delta$	Charge density ( $\text{C}/\text{m}^2$ )
$\varepsilon$	Dielectric permittivity of the medium ( $\text{C}^2/\text{Nm}^2$ )
$\Phi$	Coalescence probability (-)
$\gamma$	Interfacial tension ( $\text{N}/\text{m}$ )
$\eta$	Viscosity ( $\text{Pa}\cdot\text{s}$ )
$\phi$	Local coalescence probability (-)
$\kappa$	Inverse Debye length ( $\text{m}^{-1}$ )
$\lambda$	Correlation length of autocorrelation function (m)
$\mu$	Dipole moment ( $\text{C}\cdot\text{m}$ )
$\nu$	Frequency of vibration (-)
$\Pi$	Disjoining pressure (Pa)
$\theta$	Polarizability of molecule ( $\text{m}^3$ )
$\rho$	Density ( $\text{kg}/\text{m}^3$ )
$\sigma_{\zeta}$	Standard deviation of local potentials (V)
$\upsilon$	Speed of shear contact (m/s)
$\varpi$	Reduced diffusion correlation factor (-)
$\Omega$	Least square function (-)

$\Psi$	Electric potential (V)
$\Psi_0$	Surface potential (V)
$\Psi_d$	Stern potential (V)
$\Psi_{h/2}$	Mid-plane potential (V)
$\zeta$	Zeta potential (V)
$\zeta_{ave}$	Surface averaged zeta potential (V)

# Chapter 1 : Introduction

## 1.1 Oil sands

The Canadian oil sands, with a proven reserve (i.e. crude oil that is recoverable using current technologies) of 175 billion barrels, is the second largest oil deposit in the world (behind Saudi Arabia; Radler 2002). Much of the oil sand deposits are found in northern Alberta in the Athabasca, Cold Lake and Peace River regions, covering an area of over 141,000 km<sup>2</sup>. Typically, the Albertan oil sands comprises about 6-16% bitumen<sup>†</sup> — depending on the mine location, depth and ore grade, while the remaining compositions of the ore are mainly coarse silica sands, water, fine clays and other minerals [Kasperski 2001]. The common definition of bitumen, according to the United Nations Institute for Training and Research, is that it is a heavy and extremely viscous hydrocarbon with a viscosity greater than 10 Pa·s at deposit temperatures, and with a density of over 10<sup>3</sup> kg/m<sup>3</sup> at 15.6°C [Shaw et al. 1996]. Based on its solubility in an alkane solvent, the components of bitumen are classified roughly as asphaltenes (highest-molecular-weight fraction which is insoluble in an alkane) and maltenes (the soluble fraction). From an elemental point of view, bitumen in Alberta is typically composed of 83.5 wt% carbon, 10.5 wt% hydrogen, 0.4 wt% nitrogen, 1.1 wt% oxygen and 4.5 wt% sulphur—regardless of the ore grades [Speight 1991]. After bitumen in an oil sand ore is separated from the solids (a process known as *extraction*), it is upgraded to a ‘synthetic crude oil’ (SCO) product and sold to the refineries. From there, the SCO is converted into usable fuels, such as gasoline and diesel, by using conventional refinery technologies.

---

<sup>†</sup> Bitumen, in this context, refers to an extra heavy form of crude oil.

In over one hundred years past and the time ahead, the immense Albertan oil sands have sparked great anticipations and opportunities, although their development has encapsulated many challenges and complexities. In 1778 it was the fur trader Peter Pond that first discovered the Athabasca oil sands. In 1889, the chronicler of Laird expedition mentioned that the oil sands were of “non-doubtable great economic value that would make this region be prosperous in the matter of time” [Masliyah 2007]. The early pursuit of the oil was thwarted by the lack of technical know-how. In the 1920s, under the auspices of the Albertan government, Dr. Karl Clark successfully found a way of extracting bitumen from the sand on the bench scale. It then took another four decades for the first large-scale commercial oil sands operation to be established, based on the pioneering work of Clark. Even then, the initial production of SCO from the oil sands was cost-intensive and the commercial operations were straddled by very little profitability. By 2000, the oil sands industry just achieved the production capacity of 0.6 million barrels per day (mbd) [Yergin et al. 2009]. But in the period from 2000 to 2008, the industry was greatly vitalized and achieved rapid expansions in oil supply output, primarily driven by dramatically rising oil prices, impressive technology advances, and attractive fiscal and investment policies. By 2008, the oil sand production rate more than doubled to 1.3 mbd<sup>‡</sup>, which accounted for 1.5% of global oil demand [Yergin et al. 2009]. Periodically, due to financial crisis and “global recession,” the collapse in oil prices in late 2008 and early 2009 cast a shadow over the oil sands industry; billions of dollars of planned projects were postponed in Alberta [Vanderklippe 2009]. With strong global cooperation and government interventions, the industry had come through the worst of this downturn and “global recovery” began to show; the price of oil increased markedly, resulting in substantial profits for the oil sands industry in the second half of 2009.

---

<sup>‡</sup> Total Canadian oil production was 2.72 mbd in 2000, and 3.41 mbd in 2008 (1 barrel ≈ 159 L).

Despite the recent economic downturn, the global demand for oil is still high and will be even stronger in the long term, especially driven by the likely robust growth of new economies<sup>§</sup>. The world's oil demand is expected to reach in the range of 105 mbd by 2030, 25% higher than the 2008 level [Yergin et al. 2009]. On the other hand, the supply of conventional oil is being depleted at an aggregate average of 4.5% annually, equivalent to about 3.8 mbd depletion<sup>\*\*</sup> [Jackson 2007]. In view of the above factors, it is projected that by 2030, the world will need to identify new resources to produce around 96 mbd of oil supply that was not in production in 2008. Bitumen from the oil sands is one of the obvious choices as a key supplement for petroleum feedstock. In a moderately optimistic scenario, the Alberta oil sands production is projected to increase to 2.2 mbd by 2015, and to 4.3 mbd by 2030 [McColl 2009]. The enormity of the oil sands resource will undoubtedly enable Canada to become one of the top global petroleum providers in the coming decades.

## **1.2 Bitumen extraction**

Conventional oil is a liquid that flows spontaneously or is easily forced to mobilize via enhanced recovery techniques even from deep deposits. However, bitumen, like cold molasses, is an extremely viscous liquid that does not flow readily at reservoir conditions. As a result of combining physical properties of bitumen with geology and environment, the resource of the Albertan oil sands is unique. Highly specialized methods have been developed for the recovery of bitumen, among which the two most common approaches are: open-pit surface mining and in-situ thermal technologies. Similar to coal mining, the surface

---

<sup>§</sup> Mainly China, India, Brazil, and Russia.

<sup>\*\*</sup> The calculation of 3.8 mbd of depletion is based on 2008 world's oil production (excluding processing gains) of 83.9 mbd. The amount of oil required to be replaced will vary with future production levels.

-mining method is practical for recovering oil sands that lie less than 75 m beneath the ground; this accounts for about 20% of the recoverable reserves, which is mainly located north of Fort McMurray, with an area of about 1,350 square miles [Yergin et al. 2009]. The ore of oil sands is excavated using massive “trucks and shovels” and then transported to separation units using water-based extraction technology (the process is described below). On average, two metric tonnes of oil sand ore is required to produce one barrel of SCO. For mines deeper than 75 m, in-situ thermal process is method of choice for recovering bitumen from the sand that is still in place. This is commonly achieved by injection of steam or solvent into deep deposits to lower the viscosity of bitumen, allowing it to flow to the surface through pipelines. Currently, some projects, mostly located in the Athabasca region, use steam-assisted gravity drainage (SAGD) method whereas others, primarily in the Cold Lake and Peace River areas, employ cyclic steam stimulation (CSS) [Masliyah 2007]. The choice of technology for separating bitumen from the sands is based on a number of factors, including geological and economical situations. Up to now, almost all significant oil sand ores are either near ground surface or relatively shallow; their easy accessibility has caused very little motivation to obtain bitumen from deeper reserves. In the meanwhile, comparatively much higher recovery rates of bitumen (over 90%) and lower energy spending create economically favourable conditions open-pit surface mining. Therefore, a majority of oil sands operation is currently achieved through surface mining, followed by a *water-based* extraction process.

The hot water extraction (HWE) process, first patented by Dr. Clark and subsequently implemented commercially by Suncor Energy Inc. and Syncrude Canada Ltd., is the early

and most typical example of water-based (i.e. aqueous) extraction of bitumen from mined oil sands. The process is as follows: mined oil sand ore is first “slurried” in hot water and caustic at a temperature of 80°C. The slurry is gently agitated in tumblers and/or pipelines before pumping into large separation vessels (i.e. flotation tanks) [Clark 1966]. To reduce energy consumption, major efforts are being conducted to separate bitumen at increasingly lower temperatures. The Warm Water Extraction (WWE) process, operating at 50°C, and Low Energy Extraction (LEE) operating at 25°C, are two new exciting technologies that have been developed at Syncrude since the 1990s [Mankowski et al. 1996; Spence et al. 1996]. The current trend is to replace tumblers (which provide mechanical agitations) with pipeline transport systems in which the oil sand slurry is made to flow over several kilometres of pipes, providing the necessary agitation along the way. This is the key component in enabling lower temperatures operations. Air bubbles and flotation aids are sometimes introduced into the pipelines to enhance conditioning of the slurry feed.

Despite some variations in operating parameters with different aqueous extraction processes, their main and fundamental steps illustrated in Figure 1-1 are similar and described here. First, mined oil sands lumps are broken up into small pieces by crushers and blended with recycled or fresh process water and other chemical additives (such as sodium hydroxide) in mixing boxes, cyclo-feeders, stirred tanks or rotary breakers to form a slurry. The slurry is then directed to hydro-transport pipelines or agitating tumblers, where the oil sands lumps are mechanically sheared and the complex structure of the slurry undergoes important transformations — a process known as **slurry conditioning**. Slurry conditioning facilitates the separation of bitumen from the sand grains by breaking the bonds that hold the bitumen, water and sand together. The consequent slurry is a dispersion mixture consisting of water,

coarse sand grains, fine clays, and dispersed bitumen droplets with sizes ranging from micrometers to millimetres. Upon close examination on smaller length scales regarding the dimensions of the mixture constituents, the slurry conditioning step can be divided into the following components:

- *Ablation* of oil sand lumps: After being warmed, the outer layers of the sand lumps are easily peeling off by mechanical agitation, and a fresh lump surface becomes exposed to the dispersing condition and repeated the process until the whole lumps are completely ablated.
- *Liberation* of bitumen from the sand particles: Once a three-phase contact point is formed, the bitumen recedes from the sand grain surface to create an aggregate or a globule and then detaches itself from the solid surface.
- *Coalescence* of bitumen droplets: Owing to hydrodynamic shear, the bitumen droplets are able to approach one another and collide. Under favourable conditions, the colliding droplets will coalesce into larger droplets.
- *Aeration* of bitumen droplets: Because bitumen has a density almost identical to that of water, the liberated droplets cannot float on their own in the flotation tank. To correct for this, the bitumen droplets are made to collide with dispersed air bubbles, resulting in the engulfment of bitumen around the air bubble — a structure that is much lighter than water and can readily float and form a froth.

Here, it should be pointed out that there is no reason for the aforementioned components of slurry conditioning occur in sequence and it is most likely that they take place simultaneously.

After being properly conditioned, the slurry is fed into a large flotation vessel (known as the primary separation vessel or PSV) that is maintained under quiescent condition in order to allow for the slurry to separate into three layers. Additional water is added as the slurry additive to improve the rate of separation. The aerated bitumen droplets, being much less dense than the surrounding water, float to the top and form a primary froth. Meanwhile, the sand grains with higher density sink to the bottom and are withdrawn as the “tailings steam.” At the middle section of the vessel, a portion of the slurry known as the “middlings” is collected and further processed to recover the significant amount of bitumen that it still contains. The resident time of slurry in the PSV is approximately 45 minutes [Shaw et al. 1996]. This step is referred as *primary separation*.

The “middlings” steam from the primary separation vessel (PSV) is a suspended mixture of solid fines, water and small bitumen droplets. In order to recover additional bitumen, the middlings is further introduced into a flotation cell or hydro-cyclone where air is injected and strong agitation is applied. This added air in high shear encourages the creation of additional bitumen-air attachment that will rise on the top of the vessel and form a secondary froth. Steam is used to de-aerate the secondary froth, from which the bitumen is usually recycled back to add into the primary froth in the PSV. This step is referred as *secondary flotation*.

Bitumen froth collected from either the primary or secondary stage is far from pure: it contains typically 30 wt% water and 10 wt% solids; such a froth must be ‘cleaned’ (i.e. remove the unwanted water and solids) before the bitumen can be sent to downstream upgrading facilities. To achieve this, a diluent (i.e. organic solvent) is added to the froth to make it flow easily and facilitate the separation of water and solids from the bitumen-

continuous phase. The two main commercial processes of froth cleaning are identified based on the type of diluent used; these are the naphtha-based and paraffin-based froth-cleaning processes. In the former method, the bitumen froth is diluted with naphtha, and then goes through a combination of inclined plate settlers (IPS) and centrifuges. Inclined plate settlers allow for the solid particles to settle efficiently under gravity, in a relatively small vessel by increasing settling area with inclined surfaces. The diluted bitumen from the IPS is claimed as a finished product. The tailings stream from the IPS is injected into scroll centrifuges to spin out most of the water and coarse particles. From here, the hydrocarbon portion (i.e. product stream) further goes through disc centrifuges where finer solids and small water droplets are removed. In the paraffin-based method, the froth is diluted with a paraffinic solvent in counter-current decantation vessels, where asphaltene precipitation is induced. Centrifugation is unnecessary in the paraffin-based method as the unwanted solids and water drops are captured by the asphaltene precipitates and settle together under gravity [Tipman & Shaw 1993]. The above steps are referred as *froth treatment*.

The “tailings” streams from primary and secondary separations are discharged to a pond where the water is recycled and the solids are allowed to settle. While coarse solids segregate rapidly, the fine particles (predominantly clays) remain in suspension and are the main cause for the problem of reclaiming tailings ponds [Masliyah et al. 2004].

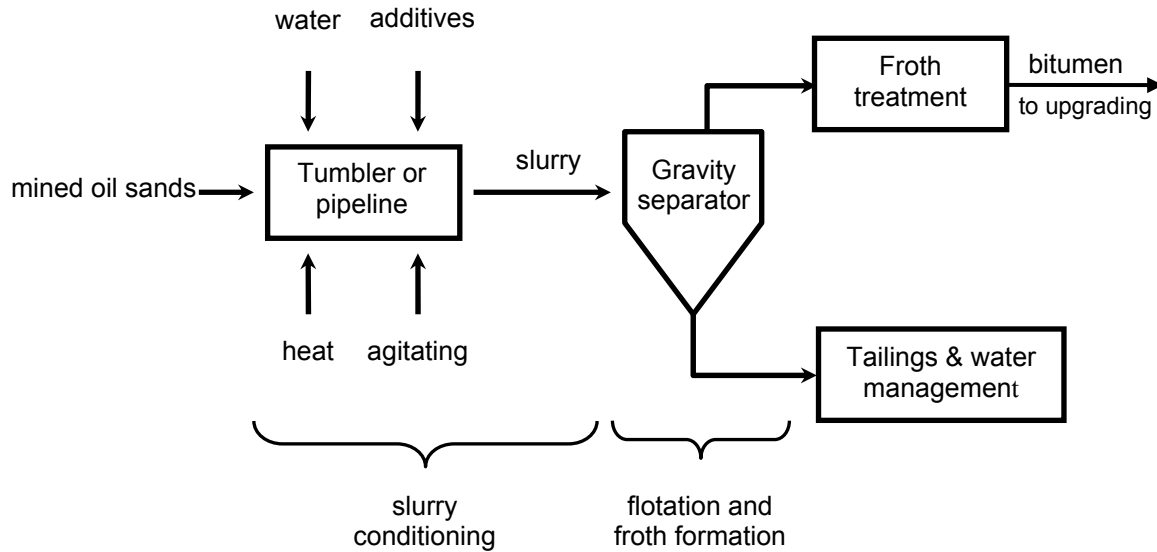


**Figure 1-1: A generalized scheme for water-based bitumen extraction process for the surface mined oil sands.**

### 1.3 Problem definition

There is no doubt that optimizing the efficiency of bitumen extraction (i.e. increasing bitumen recovery rate and product quality) is the paramount goal that oil sands operators wish to achieve, for the sake of minimizing operational cost and environmental impact. Currently, for good processing ore, the oil sands operation is quite successful and bitumen recovery can exceed 93%. However, for poor processing ore, low bitumen recovery rate of less than 70% and poor froth quality is often experienced. From an economic point of view, a 1% reduction in bitumen recovery is equivalent to about half a million dollar loss daily at current operation scale<sup>††</sup>. In terms of the environment, the lost bitumen, eventually to be discharged into the tailings ponds, is a crucial threat to wildlife. For example, media reports

<sup>††</sup> This estimation is based on the fact that the average sale price of bitumen was 35-40 dollar per barrel, half price of light crude oil and the operation capability of oil sands was 1.3 mbd in the second half of 2009 [Yergin et al. 2009].

of an estimated 1,600 ducks perishing in a tailings pond in April 2008 placed this issue in the forefront. The ducks were killed by being covered with the layer of bitumen, not because of other toxic material in the pond [O'Donnell 2009].

Understanding fundamentally the steps of bitumen extraction (discussed in Section 1.2) is critical to improving the recovery efficiency. Among those steps, slurry conditioning is no doubt the most important and has thus been the center of many past and current research works. To promote high bitumen recovery, the oil sands slurry must be well conditioned. Some key process parameters are known to influence the degree of conditioning, including process water chemistry, operating temperature, conditioning time, and stirring or tumbling rate applied to the slurry. In the past decades, intense studies had been carried out at the macroscopic and microscopic scales on correlating these factors with the various elements of slurry conditioning (particularly bitumen liberation and aeration) [Kasperski 2001; Masliyah 2007]. Here, we are much concerned with the microscopic mechanisms of conditioning elements, which involve examining the interactions of interfaces (such as bitumen-water, sand-water, and bitumen-air). For example, from direct surface force measurements between bitumen and silica substrate, it was observed that the electrostatic repulsive force increased — and the adhesive forces decreased — with increasing solution pH or temperature. This finding suggests that bitumen liberation from sand grains is well promoted at optimal pH (~8.5) and higher temperature [Liu et al. 2003]. Regarding bitumen aeration, it was found that while the electrostatic repulsion between an air bubble (air-water interface) and a bitumen droplet (oil-water interface) was decreased significantly with increasing salinity — resulting in the facilitation of bitumen-air engulfment — the presence of clay fines hinders

bitumen-air attachment due to steric repulsive effects [Moran et al. 2000b]. A comprehensive review of related research can be found in the papers by Kasperski [2001] and Masliyah [2007].

In comparison with bitumen liberation and aeration, the importance of bitumen coalescence has been underestimated and the basic coalescence mechanism is not well understood. To highlight the importance of bitumen droplet coalescence, it is observed from experience that the fraction of fine bitumen droplets, particularly those less than 50  $\mu\text{m}$  in diameter, are less ready to be aerated and more likely to go into the middlings or eventually lost to the tailings stream. Moreover, the flotation efficiency is believed to enhance significantly with bigger sized droplets. Therefore, bitumen coalescence, which serves to grow micron-sized droplets into much larger ones, is indeed critical to the bitumen extraction process [Shaw et al. 1996]. Earlier studies had shown that, under conditions of industrial relevance, the electrostatic repulsion between dispersed bitumen droplets was much larger than the attractive van der Waals forces, thus making droplet-droplet coalescence completely unattainable — at least in theory [Wu et al. 1999]. Recent investigations, however, had demonstrated that coalescence between bitumen droplets did occur, albeit randomly [Esmaeili 2009]. Moreover, from empirical observation, the coalescence process appeared to be greatly enhanced when the droplets were brought into oblique (i.e. sliding) contact [Yeung et al. 2003]. This, however, was just qualitative information — quantitative investigation of the role of shear on the coalescence phenomena, and the fundamental mechanism behind the shear-induced bitumen coalescence, has not yet been reported in the literature.

## 1.4 Specific objectives

The objective of this thesis is to understand the basic science which underlies the coalescence of bitumen droplets in aqueous environments under equilibrium and dynamic conditions; the practical motivation is to minimize oil loss to the tailings stream during water-based bitumen extraction. More specific objectives are:

- To measure the (average) zeta potential of bitumen droplets in aqueous media in order to provide the basis for subsequent investigations of electrostatic double layer interaction between bitumen droplets.
- To develop novel micropipette technique to extend the coalescence probability study from head-on contact to oblique contact under precisely controlled experimental conditions.
- To investigate the coalescence phenomenon between two individual bitumen droplets directly and quantitatively using a modified micropipette technique.
- To investigate the effects of various parameters, such as aqueous phase pH, divalent ions concentration, and the distance and speed of controlled shear contact, on the probability of coalescence.
- To develop a theory to explain the experimental observations; the model will be based on surface charge heterogeneity at the oil-water interface. The theory will be of value to water-based bitumen extraction in particular, and to colloidal interactions between non-ideal (heterogeneous) surfaces in general.
- To directly measure local potential fluctuations along the bitumen-water interface using Atomic Force Microscopy (AFM) and to compare the results with those calculated based on our proposed theory of surface heterogeneity.

## 1.5 Document layout

This thesis is organized as follows:

**Chapter 1** is an introduction and overview of the Canadian oil sands development and the water-based bitumen extraction process. This is followed by the motivations (shown in problem definition), objectives and organization of this thesis.

**Chapter 2** has two primary tasks. The first one aims to give comprehensive reviews from the existing literature on colloidal interactions and transport kinetics that govern droplet-droplet coalescence. Application of coalescence theories to aqueous bitumen recovery is also discussed. The other purpose of this chapter is to develop the relevant theories and their respective governing equations used in this thesis work; this is the novel contribution of the present research.

**Chapter 3** describes the experimental methods used in this thesis. Electrophoresis was used to measure the surface potentials of bitumen droplets in aqueous solutions. The micropipette technique, originally developed for studying the behaviour of individual emulsified drops, was modified by using video camera instead of microscopy to observe and record the coalescence process between relatively large bitumen droplets. Moreover, AFM was applied for directly mapping surface potential variations along the bitumen-water interface.

**Chapter 4** discusses the experimental and theoretical modeling results. Experimentally, the quantified probabilities of bitumen-bitumen coalescence were obtained in different conditions by varying several parameters. Theoretically, the probabilities were predicted by

using the proposed model of surface heterogeneity and compared with the experimental observations. Likewise, the mean and standard deviation values of zeta potentials “random signal,” along the distance over bitumen-water interface, were directly calculated by one dimensional AFM scanning; the characteristic length of their autocorrelation functions was also obtained. The comparison between the relevant parameters from AFM study and proposed heterogeneity model showed that their results were in good agreement.

In **Chapter 5**, concluding remarks are made, along with recommendations for further work.

## **Chapter 2 : Literature Review**

Coalescence is a process by which two (or more) liquid droplets join together to form a larger drop. The coalescence process is often considered to be comprised of three sequential stages: approach of two droplets toward each other, drainage of a thin liquid film between the two drops, and finally, rapid rupture of the film at a critical thickness [Hiemenz & Rajagopalan 1997]. The rupture of the thin liquid film involves complex colloidal interactions and transport phenomena; it is often believed to be the rate-limiting mechanism in the overall coalescence process. In order to understand the mechanistic picture of a coalescence event in a bitumen-in-water emulsion system, we will first review the fundamental science behind colloidal stability in a broader variety of colloidal systems, and then narrow down to previous studies on bitumen coalescence in aqueous media. Generally, this chapter is organized as follows: Section 2.1 will be mainly concerned with colloidal interactions and the theoretical interpretation of coagulation and coalescence mechanism. In Section 2.2, we turn to the question of transport phenomena and the kinetics of droplets coagulation and coalescence. Section 2.3 gives a discussion of the role of colloidal interactions in water-based bitumen extraction. Specifically included in this section are the relevant theories and equations related to this thesis, which will be proposed and demonstrated in much more detail.

### **2.1 Colloidal Interactions**

It is well recognized that, even though coalescence is favoured thermodynamically, the liquid drops are often stabilized kinetically by colloidal and hydrodynamic interactions between the

drop surfaces. When two droplets (colloidal size or larger) approach one another at very close distances (on the order of 100 nm), colloidal interactions will come into play. Such interactions will ultimately determine whether coalescence will occur. Clearly, the effect of any thermodynamic “driving force” can become irrelevant if there exists strong repulsion between the droplets. In such cases, the coalescence rate is effectively zero and the emulsion is considered stabilized (in a kinetic sense) by the colloidal forces. There are a number of colloidal forces in Nature. Extensive studies and review articles have appeared in this area in the last century, contributing to the development of colloid science and physical chemistry. Excellent references on colloidal interactions can be found, for example, in the books by Israelachvili [1992], Hiemenz & Rajagopalan [1997], Adamson [1990] and van Oss [2006].

In this review, the two colloidal interactions which will be discussed in detail are the *van der Waals* (VDW) and *electric double layer* (EDL) interactions.

### **2.1.1 *Van der Waals* (VDW) interactions**

*Van der Waals* (VDW) interactions exist between any two materials across any medium. These forces, for instance, not only contribute to the non-ideality of gases and gas adsorption, but also relate to many interfacial phenomena such as surface tension, adhesion, cohesion, wetting and coalescence. This section is primarily concerned with the strengths of the VDW attractions between colloidal particles, initiated by molecular-level description of such interactions.

### 2.1.1.1 Molecular origins of VDW interactions

Van der Waals (VDW) forces originate from the permanent or induced dipole interactions at the atomic and molecular levels. Generally, such forces can be classified into three main categories: *Keesom* interactions between two permanent dipoles; *Debye* interactions between a permanent dipole and an induced dipole; and *London* interactions between a pair of induced dipoles [Hiemenz & Rajagopalan 1997]. Interactions between dipoles, whether permanent or induced, are the result of the electrical field produced by one dipole acting on the second one. For polar molecules, this electrical field ( $E$ ) at large distances (compared with the length of dipole) depends on the permanent or induced dipole moment. The magnitude of permanent dipole moment,  $\mu$ , is given by the product of the dipole charge ( $q$ ) and the separation distance ( $h$ ) between the two charges (i.e.  $\mu = q \cdot h$ ), while the induced dipole moment ( $\mu'$ ) is the strength of the electrical field  $E \times$  the polarizability  $\theta$  of the induced molecule (i.e.  $\mu' = \theta \cdot E$ ). Even for non-polar molecules, an instantaneous electric field is created by the rapid fluctuations of the electron clouds in the molecule. In such a case,  $\mu = 0$ , and the London interactions are related to the vibrational frequency of the electron  $\nu$  and the polarizabilities ( $\theta$ ) of the molecules involved. Here, it is important to note that all three types of VDW potentials share, as a common feature, an inverse sixth-power dependence on the separation distance between the molecules (assuming the electromagnetic retardation effect is negligible). As such, the total intermolecular VDW interactions ( $V_{VDW}$ ) can be expressed as:

$$V_{VDW} = -\frac{C_T}{h^6} = -\frac{C_K + C_D + C_L}{h^6} \quad (2.1)$$

where  $C$  represents intermolecular VDW energy coefficient, and the subscripts  $T$ ,  $K$ ,  $D$ ,  $L$  represent total, Keesom, Debye, and London-type VDW interactions, respectively.

Among the three types of VDW forces, the London-VDW (LVDW) interaction, also known as the dispersion interaction, is always present between any two molecules — whether or not they possess permanent dipoles (it is somewhat like gravitational forces in terms of its ubiquitous nature). Moreover, when looking at the relative magnitude of the three interaction contributions, the dispersion component is the most dominant in almost all cases, except in cases of highly polar molecules such as water. As such, the dispersive part of VDW interactions is often considered its most important component.

#### **2.1.1.2 VDW interactions between colloidal particles**

Generally, there are two main approaches to calculating the VDW interaction between colloidal particles (as function of their separation distance). The first, microscopic, approach is based on the Hamaker theory; the interaction energy is obtained through pairwise summation of VDW interactions between every pair of particles (i.e. atoms or molecules). The second, macroscopic, approach is known as the Lifshitz theory. Its calculation of the interaction potential is entirely related to bulk macroscopic properties of materials, such as dielectric permittivity and refractive indices (of the dispersed particles and intervening medium). Regardless of the approach, it is noted that the final forms of interaction potentials between particles of different geometries remain similar; the only difference is the way that the constant in the formula, known as the Hamaker constant, is obtained. For example, the VDW interactions between two infinite parallel plates is given by

$$V_{VDW}(h) = -\frac{A_H}{12\pi h^2} \quad (2.2)$$

where  $V_{VDW}$  is the VDW interaction energy per unit area,  $h$  is the distances between the two plates, and  $A_H$  is the Hamaker constant. Accounting for the effect of the medium leads to the useful combining relation for Hamaker constants. Specifically, the Hamaker constant  $A_{ijk}$  for dispersed particles  $i$  and  $k$  separated by medium  $j$  can be obtained from the relation

$$A_{ijk} = (A_{ii}^{1/2} - A_{jj}^{1/2})(A_{kk}^{1/2} - A_{jj}^{1/2}) \quad (2.3)$$

where  $A_{ii}$  is the Hamaker constant representing two  $i$ -particles interacting across vacuum.

## 2.1.2 Electrostatic interactions

Electrostatic interactions arise from electrical charges; they play a very important role in predicting electro-kinetic phenomena and the stability of a variety of colloids. This section is to introduce some basic concepts in the theory of electrostatics, and to describe the electrostatic interactions between two particle surfaces in a simple geometric situation.

### 2.1.2.1 Origin of surface charge

When dispersed in an electrolyte, the surface of a particle or droplet is normally charged. Several charging mechanisms are classified into the following [Hunter 1981]:

- Differential affinities of electron between two phases, exemplified by the contact potentials that develop between liquid mercury in an aqueous electrolyte [Sparnaay 1972].
- Differential dissolution, adsorption of ions between two phases, such as the charge of silver iodide (AgI) surface in aqueous solutions because silver ions ( $\text{Ag}^+$ ) dissolve

in water preferentially; negative surface charges of air bubbles or oil droplets in pure water since hydroxyl ions ( $\text{OH}^-$ ) from water molecules adsorb at their interface [Marinova et al. 1996].

- Dissociation of surface moieties, commonly observed with carboxylic acid, sulfonic acid, amine and oxide surfaces. The surface groups may be naturally occurring complexes or adsorbed surfactants.
- Physical entrapment of non-mobile charge in one phase, which often occurs in solids where  $n$  and  $p$  type defects in crystal. One specific example is the isomorphous substitution of  $\text{Si}^{4+}$  by  $\text{Al}^{3+}$  on the clay surface, generating a negative charge.
- Differentially charged surface sites in one phase, for example, when a kaolinite platelet is broken in acidic pH, the positively charged edge coexists with the negatively charged basal plane, resulting in specific properties [Hunter 1986].

### 2.1.2.2 Electric Double Layer (EDL)

A charged surface due to one or more of the above mechanisms would generate an electric field and influence the distribution of ions in solution, where ions of opposite sign (the counter-ions) are attracted toward the substrate, while charges of the same sign (co-ions) are pushed away. The layer of surface charge and attracted counter-ions in solution are known to form the *electric double layer* or EDL [Hunter 1986]. To describe the charge or potential distribution in the EDL, much effort was carried out. Helmholtz, in 1879, proposed a model of a parallel plate capacitor. This simplest model assumed that the counter-ions were immobilized on the charged surface, thus balancing the charge (Figure 2-1a). (In reality, there always exists thermal motion of the ions in the solution.) Next, in the 1910s, Gouy

(1910) and Chapman (1913) accounted for the effect of unbound charges and developed the well-known model of diffuse double layer within which counter-ions were less associated but “smeared out” from the surface (Figure 2-1b). With this model, the very important *Poisson-Boltzmann* (P-B) equation was derived. The following is the P-B equation in Cartesian coordinates:

$$\nabla^2\psi = \frac{\partial^2\psi}{\partial x^2} + \frac{\partial^2\psi}{\partial y^2} + \frac{\partial^2\psi}{\partial z^2} = -\frac{1}{\varepsilon} \sum_i n_i^0 z_i e \exp\left(\frac{-z_i e \psi}{k_B T}\right) \quad (2.4)$$

where  $\psi$  is the electric potential in the EDL,  $\varepsilon$  is the dielectric permittivity of the solvent,  $n_i^0$  is the concentration of type- $i$  ions in the bulk,  $z_i$  is the valence of positive or negative ions,  $e$  is the fundamental charge,  $k_B$  is the Boltzmann constant, and  $T$  is the temperature of the solution. In general, for complex geometries of charged surfaces, the expression (2.4) cannot be integrated analytically without approximation of the exponential term. Numerous solutions of this equation have to be presented [Loeb et al. 1961].

For simplicity, if the charged surface is treated as planar, assuming the potential  $\psi$  only vary with  $x$ , the P-B equation is reduced to

$$\frac{d^2\psi(x)}{dx^2} = -\frac{1}{\varepsilon} \sum_i n_i^0 z_i e \exp\left(\frac{-z_i e \psi(x)}{k_B T}\right) \quad (2.5)$$

Because the counter-ions tend to be more accumulated and produce greater significance within the EDL than the co-ions, it turns out to be possible to approximate an asymmetric electrolyte as symmetric, assuming the valence of the counter-ions while incurring little error [Verwey 1948]. Such a simplification leads to  $n^0 = n_+^0 = n_-^0$ , and  $z = z_+ = z_-$ . In such a case, using the integration procedure with respect to  $x$ , from some point in the bulk

(where  $x = \infty$ ,  $\psi(x) = 0$  and  $\frac{d\psi(x)}{dx} = 0$ ) up to a point in the EDL, allows eqn (2.5) to be

written as

$$\frac{d\psi(x)}{dx} = -\frac{2\kappa kT}{ze} \sinh\left(\frac{ze\psi(x)}{2k_B T}\right) \quad (2.6)$$

where

$$\kappa = \left(\frac{2e^2 n_0 z^2}{\epsilon k_B T}\right)^{1/2} \quad (2.7)$$

The inverse of this parameter,  $\kappa^{-1}$ , is called the *thickness of the double layer* or the *Debye length*; this parameter strongly depends on the concentration and valence of the dissolved ions in the bulk. The solution of eqn (2.6), with the boundary condition  $\psi(0) = \psi_0$  (potential at the surface), can be expressed as

$$\tanh\left(\frac{ze\psi}{4k_B T}\right) = \tanh\left(\frac{ze\psi_0}{4k_B T}\right) \exp(-\kappa x) \quad (2.8)$$

In the case that  $\psi(x)$  has fallen to a small value regardless of its initial value  $\psi_0$ , i.e., when

$p = \frac{ze\psi}{4k_B T} \ll 1$  (with  $\frac{k_B T}{e} = 25.7 \text{ mV}$  at  $25^\circ\text{C}$ ), we will have  $\tanh p \approx p$  and eqn (2.8)

becomes

$$\psi(x) = (4k_B T / ze) \tanh\left(\frac{ze\psi_0}{4k_B T}\right) \exp(-\kappa x) \quad (2.9)$$

If we make one further simplification — that the surface potential  $\psi_0$  is also small compared to  $k_B T / e$  — then eqn (2.8) will take on the linearized form

$$\psi(x) = \psi_0 \exp(-\kappa x) \quad (2.10)$$

This is known as the solution of the Debye-Hückel approximation. This equation suggests that, for low surface potentials, the potential  $\psi(x)$  within the EDL decays exponentially with

the distance from the charged surface. For highly charged systems, however, the Debye-Hückel approximation is inapplicable and often overestimates the potential.

In the preceding Gouy-Chapman model, the dissolved ions were treated as point charges and the solvent as a dielectric continuum of constant permittivity. However, as the separation distance between the ion and the charged surface reduces to the angstrom scale, the finite size of the ions, whether hydrated or not, must be taken into account. In addition to the finite sizes of ions, a higher electric field near the charged surface could yield considerable ordering of solvent molecules, leading to modifications of the dielectric permittivity. Recognizing these effects, Stern (1924) and Grahame (1947) developed a modern theory in which the EDL was divided into separate regions (Figure 2-1c):

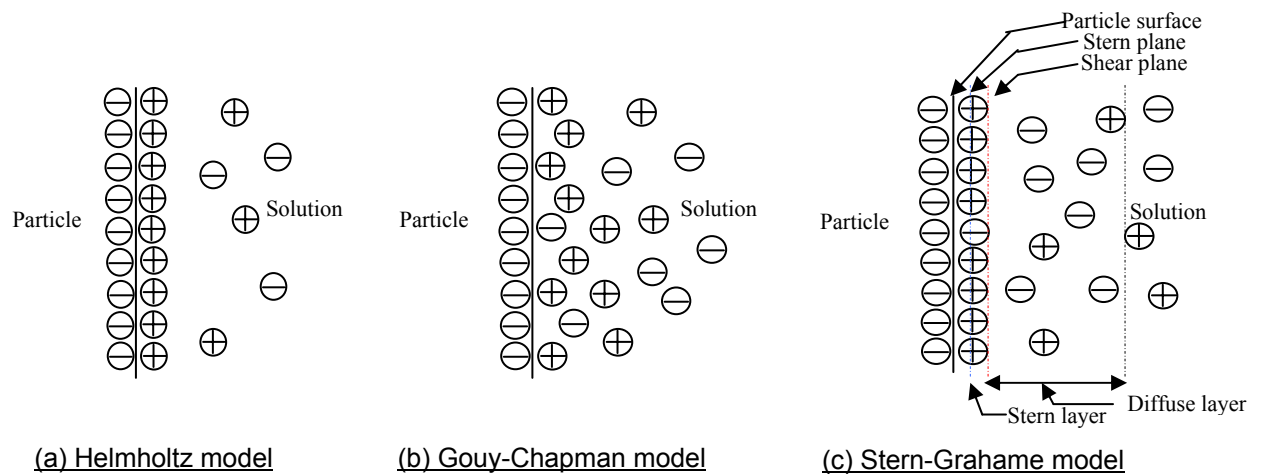


**Figure 2-1: The three proposing models for an Electrical Double Layer (EDL):**

(a) Helmholtz model, (b) Gouy-Chapman model, and (c) Stern-Grahame model.

- The inner *Stern* layer, also referred to as Helmholtz plane, in which the counter-ions are bound/immobilized on the surface and the potential distribution is decided

primarily by the geometrical constraints of ionic and molecular sizes, as well as short range interactions between the ions. Typically, the thickness of this layer is about one radius of an ion directly away from the charged surface. The electric potential at the Stern layer is called the Stern potential  $\psi_d$ .

- The outer *diffuse* layer, treated as Gouy-Chapman section. The starting point of the diffuse double layer is the so-called plane of shear, which is about one to two ionic radii away from the surface. The potential at the shear plane is the well-known *zeta potential* (denoted  $\zeta$ ), which will be singled out for further discussion in the next section. The zeta potential  $\zeta$  is marginally different in magnitude from the Stern potential  $\psi_d$  and it is customary to approximate  $\psi_d$  as  $\zeta$  [Shaw 1980]. Away from the shear plane, the above-mentioned P-B equation (2.4), or one of its approximations, may be expected to give a reasonable representation of the potential distribution. Two simplifications are often made when analysing the diffuse layer: (1) the distance  $x$  from the charged surface is measured from the shear plane rather than from the actual solid surface, and (2) the  $\zeta$ -potential, instead of surface potential  $\psi_0$ , is taken as the potential at the inner boundary condition [Hiemenz 1997].

### **2.1.2.3 Zeta ( $\zeta$ ) potential**

The zeta potential ( $\zeta$ ) is one of the most important characteristics of a charged surface, as it determines many electro-kinetic phenomena and controls colloidal stability. Generally,  $\zeta$  is a measurable quantity and there are various methods for doing that. The most common

approach is called *electrophoresis*, which is based on measuring the drift velocity of a suspended charged particle under the influence of an electric field.

Here, it should be noted that the sign and magnitude of  $\zeta$  are commonly dependent on the inherent surface ions of a particle, the adsorbed ions at the interface, and the nature and composition of the surrounding medium in which the particle is dispersed. According to their degree of influence on the potentials, as illustrated in Figure 2-2, the types of ions or electrolytes are classified into the following [Hunter 1981; Butt et al. 2003]:

- *Potential determining ions* (PDI), which are the ionic species that effectively control the surface potential  $\psi_0$  and the  $\zeta$ -potential. This type of ions is generally a component of the surface, either dissociated from the surface moieties or adsorbed from the solvent onto the surface.  $H^+$  and  $OH^-$  ions are typical examples. The solution pH is often the fundamental PDI concentration scale, and there exists a particular concentration of PDI which makes the  $\zeta$ -potential zero; this is called the *isoelectric point* (IEP).
- *Indifferent electrolyte ions* (IEI) are the ions that generally control the thickness of the electric double layer (see eqn 2.7) but do not exert any specific interaction with the surface. Usually, a change of indifferent ion concentration will mildly alter the  $\zeta$ -potential by varying the Debye length  $\kappa^{-1}$ , while keeping surface potential  $\psi_0$  unchanged.
- *Specifically adsorbed ions* (SAI) are any ions that are able to penetrate the inner Stern layer and undergo the specific interactions with the surface. These specific interactions may be “chemical” (i.e. involving covalent bonding with surface atoms)

or “physical” (e.g. attachment onto the surface via VDW forces). While not changing surface potential  $\psi_0$ , the SAIs are identified by their ability to affect significantly — even reverse the sign of — the  $\zeta$ -potential. By contrast, indifferent electrolyte ion can only decrease  $\zeta$ -potential asymptotically to zero.

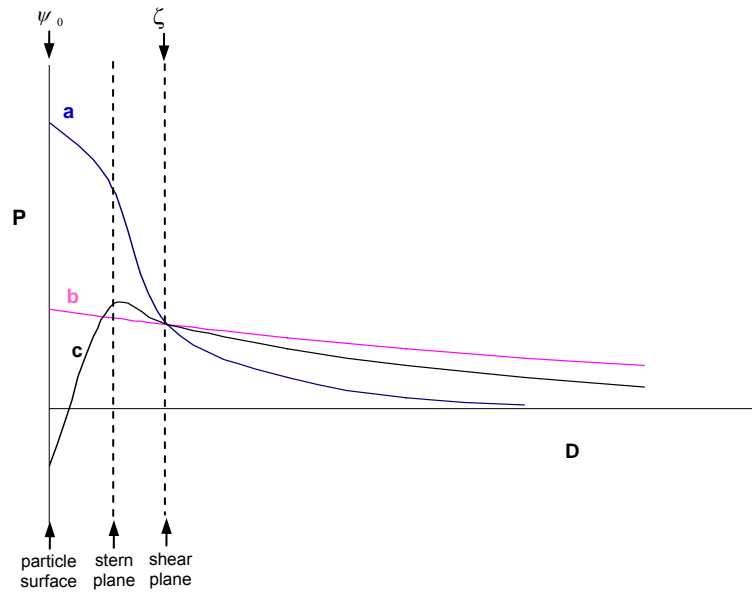


**Figure 2-2: The three potential distributions leading to the same  $\zeta$ -potential, however, the state of the interface and the inner stern layer is vastly different in the three types of ions: (a) potential determining ions; (b) indifferent electrolytes; (c) specifically adsorbed ions. Here, the horizontal axis represents the distance away from the particle surface and the vertical axis shows the potential [Adapted from Hunter 1981].**

#### 2.1.2.4 EDL interactions between two planar surfaces

As mentioned above, for a charged surface in an electrolyte, an electric double layer will form and the potential will decrease with the distance from the surface. Here, our focus is on the electrostatic interactions between two charged surfaces. As seen in Figure 2.3, the

dashed lines indicate the potential profiles of each plate if the other (opposing) plate were absent. However, as two similar surfaces approach each other, the two double layers will “overlap” when the separation is several Debye lengths or smaller. When this occurs, the potential profile in the gap will appear as the solid line in Figure 2-3, and there will be a higher concentration of counterions in the gap relative to the bulk. The osmotic pressure created by the increased counterion concentration is what gives rise to the EDL or “electrostatic” repulsion between the plates.

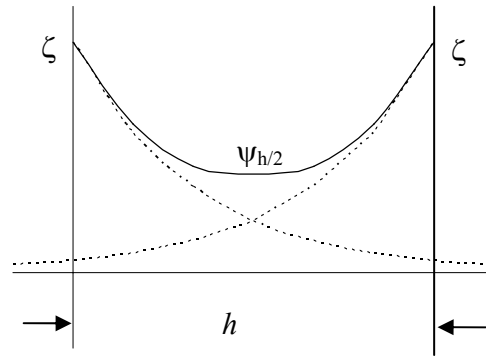


**Figure 2-3: Schematic representation of the change in potential distribution when two similar planar surfaces approach to the distance of separation  $h$ .**  $\psi_{h/2}$  is the potential at the mid-plane. [Adapted from Hunter 1986].

To obtain the repulsive force (or energy) in the gap between two identical plates, we would consider the hydrostatic equation governing fluid pressure in the electrical field. At equilibrium, and neglecting gravity, the pressure force  $F_p$  is balanced against electrical force  $F_e$ . In a one-dimensional system,

$$F_p = \frac{dp}{dx} = F_e = -\delta \frac{d\psi(x)}{dx} \quad (2.11)$$

where  $\delta$  is the charge density. Combining with the Poisson equation

$$\frac{d^2\psi(x)}{dx^2} = -\frac{\delta}{\varepsilon} \quad (2.12)$$

for electrostatics, eqn (2.11) becomes:

$$\frac{dp}{dx} - \varepsilon \frac{d^2\psi(x)}{dx^2} \frac{d\psi(x)}{dx} = 0 \quad (2.13)$$

or

$$\frac{d}{dx} \left[ p - (\varepsilon/2) \left( \frac{d\psi(x)}{dx} \right)^2 \right] = 0$$

Integration of this equation leads to:

$$p - (\varepsilon/2) \left( \frac{d\psi(x)}{dx} \right)^2 = P \quad (2.14)$$

where  $P$  is the integration constant which physically is the pressure in the gap. The first term in eqn (2.14) describes the osmotic pressure caused by the excess ions in the gap, and the second, known as the Maxwell stress, is due to electrostatic forces between the two charged surfaces. Equation (2.14) implies that the net “electrostatic repulsion” is due to the increase in osmotic pressure force as the two electric double layers overlap. For identical plates in  $z$ :  $z$  electrolyte, in the middle the gradient should be zero because of symmetry, i.e.  $\frac{d\psi(x=h/2)}{dx} = 0$ . Then, the additional osmotic pressure  $\Pi_{h/2}$  created by excess ions in the mid-plane (shown in Figure 2-3) is equal to:

$$\Pi_{h/2} = k_B T \left[ n^0 \exp\left(\frac{ze\psi_{h/2}}{k_B T}\right) + n^0 \exp\left(-\frac{ze\psi_{h/2}}{k_B T}\right) - 2n^0 \right] \quad (2.15)$$

This is an expression for the repulsion force per unit area  $\Pi(h)$  between two charged plates. If the diffuse layers only slightly overlap, the approximation given by eqn (2.9) can be applied to the potential form of each plate, and the potential in mid-plane becomes

$$\psi_{h/2} = \psi_1 + \psi_2 = 2(4k_B T / ze) \tanh\left(\frac{ze\zeta}{4k_B T}\right) \exp(-\kappa h/2) \quad (2.16)$$

Since this result applies to conditions that are well away from the surface, and the potential is low at the mid-plane, we can further simplify eqn (2.15) or  $\Pi(h)$  to obtain

$$\Pi(h) = \Pi_{h/2} = k_B T n^0 \left( \frac{ze\psi_{h/2}}{k_B T} \right)^2 = 64k_B T n^0 \tanh^2 \left( \frac{ze\zeta}{4k_B T} \right) \exp(-\kappa h) \quad (2.17)$$

In order to calculate the electrostatic interaction per unit area,  $V_{EDL}$ , we integrate the interaction force over distance to obtain

$$V_{EDL}(h) = \int_h^\infty \Pi(x) dx = 64k_B T n^0 \kappa^{-1} \tanh^2 \left( \frac{ze\zeta}{4k_B T} \right) \exp(-\kappa h) \quad (2.18)$$

The above expression is often called the *linear superposition approximation* (LSA) and it is most widely used for calculating the electrostatic repulsion energy between two identical plates [Butt et al. 2003]. For interaction between curved surfaces, the electrostatic repulsion can be obtained by using the *Derjaguin approximation*. In general, the geometry of colloidal particles can be very complicated; the associated calculations of interaction potentials (both analytical and numerical) would be very difficult and tedious. However, when the droplet sizes are more than 10  $\mu\text{m}$  — several orders of magnitude larger than the range of most colloidal forces — it is possible to integrate analytically the curvature effects and relate the colloidal forces to the interaction potential between two parallel planes [Deshiikan & Papadopoulos 1995]. At the same time, it must be pointed out that while applying different boundary conditions, the solution to the P-B equation and the resulting approximation for electrostatic potential between droplets should be somehow distinguished for either similar or unequal double layers [Frens & Overbeek 1972]. It is quite challenging to find the proper boundary condition to fit the specific system correctly (due to lack of relevant knowledge regarding to the generation mechanism of surface charge of each interacting surface). For the purpose of computation, the following two types of boundary condition are usually assumed:

(1) *constant charge* (CC), assuming the surface charge densities of the two particles to remain constant as they approach one another; (2) *constant potential* (CP), in the case that the surface potentials are assumed to unchanged as two particles come near one another (the surfaces will need to discharge in such a scenario). The results from CC and CP boundary conditions are thought of as upper and lower limits of EDL interactions, and the real situation may be somewhere between these two limits. It is suggested that the very simple expression in the LSA model (eqn 2.18), giving intermediate predictions, might serve as a good midway compromise between the CC and CP limits. It should also be remembered, however, that the LSA equation is only valid for situations when the potential everywhere between the particles is fairly low [Gregory 1975].

### **2.1.3 Classical DLVO theory**

During the Second World War, four prominent scientists Derjaguin & Landau, and Verwey & Overbeek originated a theory to give quantitative explanation of colloidal stability [Derjaguin & Landau 1945; Verwey & Overbeek 1948]. In recognition of their work, the theory has been named “DLVO.” In the classic version of the DLVO theory, the total colloidal interactions are comprised of the electric double layer (EDL) and van der Waals (VDW) interactions. Theoretical discussion and derivation of the two interactions can be found in the book by Hunter [1986] and were also briefly discussed in the previous two sections. Taking into account both DLVO components, we can approximate the total energy per unit area ( $V_T$ ) between two identical planar materials (labelled by subscript 2) across an intervening electrolyte medium (subscript 1) as function of their separation distance  $h$  by summing up the results of equations (2.18) and (2.2), i.e.

$$V_T(h) = 64n_0k_B T\kappa^{-1} \cdot \tanh^2\left(\frac{ze\zeta}{4k_B T}\right) \cdot \exp(-\kappa h) - \frac{A_{212}}{12\pi h^2} \quad (2.19)$$

Equation 2.19 enables calculation of the resultant EDL and VDW energy, from which one is able to determine the nature (i.e. attractive or repulsive) and strength of the colloidal interaction. A negative  $V_T$  value implies attractive interaction, which in turn promotes coalescence of the droplets. Conversely, a positive  $V_T$  value suggests repulsive interaction which can prohibit coalescence.

The DLVO theory was a breakthrough in the understanding of colloidal stability and has withstood several decades of scrutiny. It provides accurate prediction of the coalescence behavior of dispersed droplets — at least for systems that conform to the ideal assumptions inherent in the model [Masliyah & Bhattacharjee 2006]. In the earlier generalization, it was well-documented that, the colloidal particle in an aqueous dispersion precipitated by adding a salt, and the critical concentration of an electrolyte required to precipitate the colloidal particle was dominated by the valence of the counter-ion. This was a consequence observed by the Schulze-Hardy rule (1900); the essence of such a rule was readily derived from the DLVO theory [Heimenz & Rajagopalan 1997]. For the purpose of confirming the validity of the DLVO theory, it was first acknowledged by Tabor & Winteron [1969] that the molecularly smooth mica surface is one of most ideal for conducting such force measurements. Israelachvili & Adams [1978] used an early version of the surface force apparatus (SFA) to measure the long-rang forces (within 1-100 nm) between two cross cylinder plates of mica (1  $\mu\text{m}$  thick and 12 mm radius curvature) immersed in aqueous electrolytes. With a spectrometer, the separation between two mica surfaces was able to be

controlled and measured to better than 0.1 nm. Their results indicated that the experimental data points showed very good agreement with the force curve predicted by the DLVO theory. Deshiikan et al. [1995] reported visual microscopic observations of interactions of *n*-hexadecane oil drops inside fine glass capillaries filled with water of varying pH and ionic strengths. All the observed coalescence or non-coalescence of oil drops were in qualitative and quantitative agreement with the calculated DLVO curve, together with measured critical thickness of rupture. Several studies in the literature also suggested that bitumen appeared to be an ideal system for the application of DLVO theory using different experimental techniques. In the study of Sanders et al. [1995], an impinging jet cell was used to investigate the effect of colloidal forces on the mass transfer of bitumen to a planar collector surface. The deposition experiments were modeled by solving the governing mass transfer and flow field equations and using analytical expressions from the DLVO theory [Sanders et al. 1995]. They reported that the behaviour of bitumen droplets could be predicted from the DLVO theory. Dai and coworker studied the bitumen-sand interaction as a function of temperature using bitumen pickup test method [Dai & Chung 1995]. They concluded that temperature not only reduced the viscosity of bitumen to facilitate hydrocarbon liberation, but also increased the zeta potential of silica to enhance the repulsion between silica and bitumen (which was consistent with prediction using the DLVO theory). Rodriguez-Valverde et al. [2003] directly examined the coalescence behaviour of distilled bitumen droplets in water by visual observation from a settling test. In their study, the bitumen was obtained by the distillation of crude petroleum; it is not natural bitumen. Surface potential of distilled bitumen in water (for calculating EDL forces) was accessible by means of the Ionizable Surface Group (ISG) model [Takamura & Chow 1985], and the Hamaker constant

for the VDW force calculation was computed by means of the Lifshitz theory. The stability results suggested that the distilled bitumen dispersions did obey the DLVO theory and non-DLVO forces were not observed.

#### **2.1.4 More recent developments**

Despite its historical significance and success in explaining dispersion stability, the classical DLVO theory often fails to make accurate predictions in many practical situations due to at least two reasons: First, the boundary conditions used in the original model, which assume the interacting surfaces to be perfectly homogeneous, will likely not apply to many colloidal systems of interest. Real surfaces often show surface heterogeneities, either in the form of surface roughness or uneven charge distribution [Walz 1998]. Second, the model does not account for all the forces in a system, such as steric, hydration, and hydrophobic forces.

##### **2.1.4.1 Surface heterogeneities**

While both surface roughness and charge heterogeneities are equally “guilty” in creating substantial discrepancies between classical DLVO predictions and experimental results, their effects on DLVO forces have mostly been investigated separately. Extensive reviews on the effects of surface heterogeneities (roughness or charge non-homogeneity) on colloidal interactions were given by Czarnecki [1986] and Walz [1998].

###### **2.1.4.1.1 Effect of surface roughness on DLVO interactions**

All physical surfaces, especially solid ones, are rough on a sufficiently small scale due to the intrinsic material properties or as a consequence of the synthesis process. Over the last three

decades, theoretical models and experimental measurements have been developed to account for the presence of surface roughness and its impact on DLVO forces between rough surfaces. To describe surface roughness, the general methods in the prior work involve the arrangement of protrusive or depressive asperities (some idealized shapes are hemispheres, cones or sinusoidal waves) on a smooth surface. It is commonly found that surface roughness causes great reduction in the potential energy barrier and its effect becomes insignificant when the characteristic height of asperity is much smaller than the separation distance. Van Bree et al. [1974] derived simple expressions for calculating the correction factor of surface irregularity on non-retarded and retarded VDW forces for both plane-plane and plane-sphere configurations using pairwise summation. The irregularity was assumed to be a single harmonic oscillation with a roughness of root-mean-square (RMS) deviation from an ideally smooth plane and zero average value. They concluded that the contribution factor of surface roughness on VDW forces was about 10-50%. Sparnaay [1983] weighted the role of surface asperities on the non-retarded VDW interaction between a circular cone and a flat plate. He showed that the obvious influence of asperities became important when their characteristic heights were 10-20% of plate-plate distance. Kostoglou & Karabelas [1995] evaluated the EDL interactions between two rough parallel surfaces. The surface asperities were conceived as a sinusoidal function with an assigned wavelength and smaller-than-double-layer-thickness amplitude. By solving the linearized P-B equations, the EDL repulsion between rough surfaces were noted to be larger than that between smooth surfaces and increased with increasing asperity amplitude. Herman & Papadopoulos [1990] considered the importance of asperity shapes on EDL and non-retarded VDW interactions between two planes characterized by an asperity on each one plate. The asperity was assumed

to be conical or spherical. The EDL interaction was computed by Derjaguin approximation, while the VDW by the Hamaker pairwise summation method. They concluded that surface roughness had much more substantial impact on EDL interaction than on VDW interaction; this phenomenon would eventually affect the changing direction of suspension stability or deposition rate, depending on which interaction was dominant. Suresh & Walz [1996] studied the sensitivity of surface roughness on the total DLVO energy profile between a rough sphere and a smooth plane. The presence of small asperities was verified by scanning electron microscopy (SEM) morphology on polystyrene latex spheres. The asperities were further assumed to be protruding hemispheres that were uniformly distributed on the sphere with fixed height and low number density coverage. The VDW interaction was calculated by the general pairwise summation approach, together with the correction of retardation effects. The total EDL interaction was summed by the interaction of asperity-smooth plate and smooth plate-smooth plate with linear superposition approximation. Bhattacharjee et al. [1998] investigated the DLVO interaction between a rough sphere and a smooth plane by using the surface element integration (SEI) technique. The roughness was modeled as a normal distribution of hemispherical asperities (protrusions and depressions) with zero mean and unit standard deviation on the planar surface. It was suggested from the above two investigations [Suresh & Walz 1996; Bhattacharjee et al. 1998] that the height of the total energy barrier to particle flocculation and deposition would be substantially lowered by even a small amount of roughness, consistent with many experimental observations [Gregory & Wishart 1980; Kallay et al. 1983; Elimelech & O'Melia 1990; Litton & Olson 1993]. With the appearance of the surface force microscope, direct study of the impact of roughness on DLVO forces was also possible. For example, Ducker et al. [1991] employed an atomic

force microscope (AFM) to measure the forces between a planar silica surface and a silica colloidal probe in aqueous solutions of sodium chloride. The measured forces at very small separations (2-3 nm) deviated from the prediction of DLVO theory; such discrepancies were attributed to surface roughness. Suresh & Walz [1997] used a technique known as total internal reflectance microscopy (TIRM) to directly measure the DLVO forces between a polystyrene latex sphere and a planar glass surface immersed in different concentrations of sodium chloride. It was found that the measured secondary energy minima were much lower than those predicted from smooth surfaces, but were in good agreement with their previously proposed roughness model [Suresh & Walz 1996].

#### **2.1.4.1.2 Effect of charge heterogeneity on DLVO interactions**

Because of the finite size of ions and the coexistence of different ion types, local variations in surface charge density can potentially occur. The effects of this charge heterogeneity on the electric double layer interactions have been studied by several researchers for the last decades [Richmond 1974 and 1975; Kuin 1990; Miklavic et al. 1994; Miklavic 1995; Grant & Saville 1994 and 1995; Holt & Chan 1997; Velegol & Anderson 1996; Thwar & Velegol 2002]. To describe charge heterogeneity, the common approaches involve periodic patterns of charge distribution and normal surface charge distribution. It is also commonly shown from those studies that surface charge heterogeneity leads invariably to smaller electrostatic repulsion, lower stability ratio, and higher rates of particle deposition (compared to cases with uniformly charged surfaces). Some early studies in this area were carried out by Richmond [1974 and 1975], who proposed expressions for calculating EDL interaction between two plates in an aqueous electrolyte. The charge on each plate was expressed as arbitrary

Fourier-series distribution with zero net charge in Richmond's first article, and as discrete periodic square lattice structure in his second. The linearized P-B equation, along with constant charge boundary condition, was used to calculate the potential profile. Richmond pointed out that the relative configuration of two plates had profound impact on the direction and magnitude of the EDL interaction. Prieve & Lin [1982] examined how the stability ratio of sol particles in ionic solutions was affected by the statistical distribution of three parameters: particle size, Stern potential and charge density. To facilitate comparison, the probability distribution of any of the parameters, denoted generically as  $p(y)$ , was similarly assumed to follow a one-dimensional Gaussian, i.e.

$$p(y) = \frac{1}{\sqrt{2\pi} \sigma_y} \exp \left[ -\frac{(y - y_{ave})^2}{2\sigma_y^2} \right] \quad (2.20)$$

where  $y_{ave}$  is the mean and  $\sigma_y$  the standard deviation of the parameter  $y$ . Simple superposition approximation was used to evaluate the DLVO interaction term in the stability ratio formula. It was shown that a distribution in either the Stern potential or charge density predominantly reduced the stability ratio and its sensitivity to ionic strength, while the influence of size distribution was not important. Vaidyanathan & Tien [1991] proposed a patched surface model to satisfactorily explain the hydrosol deposition behaviors on silica substrate in most situations. Based on two extreme cases of dissociation tendencies of SiOH sites, the silica surface was assumed to be randomly covered with charged and neutral patches of uniform circular geometry. The two unknown parameters in their proposed model were the patch size  $L$  and the fraction of charged regions  $fr$ ; values of these parameters were calculated by fitting theory to experimental data. It was found that optimum values for the two parameters were:  $L = 0.5 \mu\text{m}$  and  $fr = 0.2-0.3$ . Vreeker et al. [1992] investigated the role

of nonhomogeneous surface potential on the colloidal stability of nickel hydroxyl carbonate particles in base dispersions of varying sodium nitrite concentrations. It was demonstrated experimentally that the critical flocculation concentration was much lower than that in the case of uniformly charged particle. The authors explained this lowered stability behavior by assuming sinusoidal surface charge distributions whose amplitude and period were decided by fitting to a group of experimental data curves. Song et al. [1994] introduced the notion of nominal surface potential to rationalize the empirical observations of much higher deposition rate of latex particles into a soda-lime glass collector under unfavorable conditions (low ionic strength). The nominal potential of a heterogeneous surface was defined as the potential of a homogenous surface that would generate the same EDL interaction as the heterogeneous surface with a particle at an identical separation. The surface of the latex particle was assumed to be uniformly charged, while that of the collector was heterogeneously charged with two different models. The first model was based on patchwise distribution of equipotential surface sites on the entire surface, similar to the geometry of Vaidyanathan & Tien [1991]. The second model was similar to that of Prieve & Lin [1982], in which sites of locally uniform potential were normally distributed over the entire surface. Grant & Saville [1995] developed a boundary element technique based on the method of images to evaluate the electrostatic potential between a sphere with heterogeneous and weak charges and a flat plane. The sphere was assumed to be only charged on a cap occupying one quarter of total surface, while the plane had three possibilities: uncharged, similarly charged (as the sphere), and oppositely charged. By making the linear Debye-Hückel approximation, Grant & Saville had determined that the interaction was strongly dependent on the orientation of the sphere. For instance, a significantly stronger interaction occurred for the case with the charged cap

facing the uncharged plane, compared to the case when the cap was facing away from the plate. At the same time, they had extended a similar methodology to successfully interpret the effect of non-uniform charge distribution on the model protein (lysozyme) crystal growth patterns. Many shallow minima in the protein-crystal interaction curve were consistent with experimental observation of the protein's ability to crystallize in different forms [Grant & Saville 1994].

With the advent of the AFM, direct evidence of charge heterogeneity became possible. For example, Rotsch & Radmacher [1997] presented a two-dimensional AFM force mapping method to study small positively charged bilayers of surfactant adsorbed onto the negatively charged mica substrate in aqueous electrolytes. Fluctuation in the local electrostatic interactions in the adsorbate and substrate regions, due to variations of ion charges, was clearly detected. Fleming et al. [1999] applied the in-situ soft-contact mode of AFM imaging on mixed adsorption of anionic surfactant sodium dodecyl sulfate (SDS) and nonionic polymer polyvinylpyrrolidone (PVP) on graphite. Heterogeneously adsorbed domains, consisted of ordered surfactant-rich aggregate and disordered polymer-rich adsorbate, were apparently distinguished by the results of stark contrast deflection images and very different (attractive or repulsive) force profiles. A similar observation was reinforced by Tan et al. [2005], who used AFM phase imaging technique to investigate the surface heterogeneity of polystyrene latex particles. Distinct phase domains of 50-100 nm on the smooth latex surface, possibly due to the split of ion-rich and ion-poor compositions of the polymer, appeared by high contrast in the phase image. Although it has been used to characterize patchwise charge heterogeneity, several limitations were associated with the AFM technique:

(1) the particles should be deposited onto a flat surface; (2) accessible area is restricted due to slide-off tendency of the AFM tip, scanning only on the top of particle; (3) the effective size of the tip is often too large to acquire high resolution; (4) the tip is very easily contaminated by a soft sample, especially after many cycles of scanning. Thus, the use of AFM can be very challenging in its application to individual colloidal particles suspended in a fluid.

With respect to suspended colloidal particles, Velegol and coworkers [Velegol et al. 2000; Feick & Velegol 2002 and 2003; Jones et al. 2005] had performed much significant work in this area by developing two unique techniques for quantifying the charge heterogeneity. The first one, termed *rotational electrophoresis*, involved the use of video microscopy to track the trajectory of colloidal doublets and then to acquire their angular velocity, which can in turn be related to surface charge heterogeneity. The essential physics behind this technique was that a heterogeneously charged particle would on average rotate in an electric field while a uniformly charged particle would not. The surface of each sphere in the doublet was assumed by the authors to be covered with many equal-area patches, each containing a unique *local potential* ( $\zeta_i$ ) and *patchy length* ( $L$ ). Velegol et al. [2000] also derived a straightforward equation that related the rate of rotation to the heterogeneity parameter  $\sigma_\zeta^2/N$ , where  $\sigma_\zeta$  was the standard deviation of local potential  $\zeta_i$  away from the average zeta potential ( $\zeta_{\text{ave}}$ , was measured by standard *translational electrophoresis*), and  $N$  was the number of patches on each spheroid ( $N = 8r^2/L^2$ , where  $r$  was the spherical radius and, for convenience, the patchy length was chosen as:  $L = \sqrt{r\kappa^{-1}}$ , with  $\kappa^{-1}$  being the Debye length). After measuring the doublet rotation rate and knowing other parameters in the equation (i.e. electrical field, fluid permittivity and viscosity, sphere radius, and ionic strength), the

standard deviation ( $\sigma_\zeta$ ) would be easily estimated. By using this technique, it was found that dramatic charge heterogeneity of polystyrene latex particles ( $\sigma_\zeta = 0.5\text{-}0.7 \zeta_{\text{ave}}$ ) occurred in all experimental conditions [Feick & Velegol 2002]. Later, the researchers also indicated that, for the purpose of altering colloidal stability, charge heterogeneity of colloidal particles could be significantly modified through chemical or physical methods — by adding surfactants [Feick et al. 2004] or annealing [Feick & Velegol 2004]. Although a very clever means of detecting surface charge heterogeneity, rotational electrophoresis experiment has some major drawbacks: (1) operating difficulty and time consumption; (2) relatively low resolution of optical microscopy; (3) challenge in distinguishing rotation due to electrophoresis from rotation due to Brownian motion for micron-sized particles. These three problems were avoided by introduction of a *charge non-uniformity light scattering* (CNLS) technique by Velegol and coworkers [Jones et al. 2005]. Based on visualizing rotational electrophoresis with light scattering and interpreting the outcomes with an electrokinetic model, the CNLS technique was much more efficient and could be extended to sub-micron particles (those invisible to optical light). To verify the validity of CNLS, the heterodoublets, which consisted of two different spheres with zeta potentials  $\zeta_1$  and  $\zeta_2$ , were synthesized. The best value of  $\zeta_1 - \zeta_2$  was obtained by fitting to the intensity variation of CNLS measurement; this number was compared to and shown to be in good agreement with that from translational velocity measurements or Zeta PALS measurements.

Despite their many advantages, a common weakness of the two techniques developed by Velegol et al. is that there is no direct information available on the extent of charge heterogeneity (i.e. the “patchy length”); knowing this parameter may be essential for some

applications [Feick & Velegol 2002]. Here, the following question remains: how far do the patches extend? One may expect that the size of a patch is of the same order as the ion size due to ionic origin of creating surface charges. Nevertheless, it was indicated that the answer of patch length scale turned out to be surprisingly much greater [Kozlova & Santore 2006 and 2007].

#### **2.1.4.2 Non-DLVO forces**

Numerical studies have suggested that deviations between the classical DLVO theory and experiment are ascribed to the existence of other colloidal forces, often known as “non-DLVO forces” — including steric, hydration, and hydrophobic forces.

Repulsion due to steric barriers provides another important mechanism of colloidal stability. Generally speaking, a steric repulsive force arises from the adsorption of large molecules or species (e.g. polymers, surfactants, submicron solids) onto the colloidal particles in dispersion. Reduction in the number of possible configurations of the adsorbed molecular chains when two particles are in close proximity, and the resulting decrease in entropy and increase in free energy, eventually create the repulsion (hence stabilization) effect [Butt et al. 2003]. It is further believed that the length of large molecular chains determines the thickness of the steric barrier and the strength of steric repulsion. Therefore, with low surface coverage and/or short adsorbed chains (relative to the particle size), it is possible for van der Waals attraction to overcome the steric barriers and result in colloidal destabilization. For example, it was reported that polystyrene latex particles, with a diameter of over 250 nm, would easily flocculate with an adsorbed 2.5 nm-thickness layer of nonionic surfactant which

otherwise functioned as a stabilizer for smaller particles [Ottewill & Walker 1974]. Napper [1970] also demonstrated that flocculation of sterically stabilized dispersions could be induced by a decrease in solvency of the medium for the stabilizing polyethylene oxide chains using two methods: addition of salt or increase of temperature. Similarly, in this research, we always removed the fine solids in the bitumen as received originally before each experiment. This was to eliminate the effect of steric stabilization which could result from formation of close-packed structures of fine solids or clays at the bitumen-water interface. It is also interesting to note that, when the adsorbed polymers are insufficient to fully cover the particle surface, the same molecular phenomenon can lead to an entirely opposite effect on the macroscopic scale. This is the so-called “polymer-bridging” flocculation, and is another typical scenario of inducing steric destabilization in which a polymer chain can adsorb onto two or more discrete colloidal particles and “bridge” them together to cause aggregation [Gregory 1989].

Regarding the other classes of “non-DLVO” forces, hydration and hydrophobic forces are the ones that have drawn particular attention. Earlier work on force measurement between cleaved mica sheets immersed in various aqueous electrolytes clearly showed the presence of strong short-range repulsive force at high salt concentrations ( $\geq 1.0$  M); this was attributed to the adsorbed hydrated cations [Pashley & Israelachvili 1984]. Other phenomena such as the swelling of clays [Pashley 1985], reptization [Healy et al. 1978], thin-film soap stability [Waltermo et al. 1996], and the prevention of bubble coalescence at high ionic strength [Lessard & Zieminski 1971] were also explainable in term of hydration forces. On the other hand, when hydrophobic surfaces approach one another in water, the resulting attractive

force between them was found to be surprisingly much stronger and of quite longer range than the VDW force calculated from classical DLVO theory; this was attributed to a so-called hydrophobic force [Israelachvili 1992]. The first hydrophobic force measurement was performed by Israelachvili & Pashley [1982 and 1984] using the surface force apparatus (SFA) on mica surfaces hydrophobized with cetyltrimethylammonium bromide (CTAB). This hydrophobic force had been central to various applications involving surfactant solutions [Yoon & Askoy 1999; Song et al. 2000]. Although it appears that hydration and hydrophobic forces are important in many systems of interest, the origins and physics behind these two forces, together with many other non-DLVO interactions, still remain mysterious and yet to be understood. These forces are not of the same theoretical rigor as the DLVO interactions (EDL and VDW forces). In this research, we attempted to “salvage” the DLVO theory by incorporating it with a model of randomly charged surfaces.

Thus far, we have reviewed the relevant theories of colloidal interactions. As mentioned earlier, the prerequisite for coalescence is that two colloidal particles must first collide with one another; this is the transport step. In what follows, we turn to a brief account of the various phenomena which determine this transport step; these mechanisms which cause particle-particle collision are called aggregation kinetics.

## **2.2 Aggregation kinetics**

### **2.2.1 Collision frequency**

The formation of aggregates (and coalesced drops in our case) originates from the collisions of particles or droplets. In practice, such collisions can be an outcome of three different

mechanisms: (1) Brownian motions (random particle trajectories due to thermal agitation) inherent in colloidal particles bring them together into the formation of an aggregate; this process is known as *perikinetic aggregation*. (2) Velocity gradients due to fluid flow allow particles to attain unequal velocities and eventually collide; this mechanism is classified as *orthokinetic aggregation*. (3) Particle collision can also result from the differential settling (or flotation) rates of suspended particles of different sizes and densities under gravity; this is often named *differential sedimentation*. It is seen from Stokes law (quadratic dependence of velocity on particle size) that larger particles settle (or float) much quicker and thus will collide with the smaller, slower-moving particles.

If each collision leads to an irreversible aggregation and coalescence, the rate of aggregation/coalescence would simply be equated to the collision rate. Generally, the collision rate is expressed in term of the collision frequency. After listing the three important mechanisms of collision, it is worthwhile to discuss here the dependence of collision frequency on particle size. The landmark work in this area was carried out by von Smoluchowski [1917], who considered diffusion-controlled (i.e. perikinetic) collisions of two spherical particles. Based on his theory, the binary collision frequency  $f_{ij}$  between type- $i$  and type- $j$  particles is given by:

$$f_{ij} = K_{ij} n_i n_j \quad (2.21)$$

In this equation,  $f_{ij}$  represents the total number of collisions between two particles in unit volume per unit time, with  $n_i$  and  $n_j$  being the number concentrations of the two particle types. The term  $K_{ij}$  is the collision constant, which relies on the specific mechanism

accountable for the collisions. Respective to the above three mechanisms, the collision constants can be written as [Elimelech et al. 1995]:

$$\text{Perikinetic:} \quad K_{ij} = (2k_B T / 3\eta)(d_i + d_j)^2 / (d_i d_j) \quad (2.22)$$

$$\text{Orthokinetic:} \quad K_{ij} = (G / 6)(d_i + d_j)^3 \quad (2.23)$$

$$\text{Sedimentation:} \quad K_{ij} = (\pi \Delta\rho g / 72\eta)(d_i + d_j)^3 (|d_i - d_j|) \quad (2.24)$$

In the above equations,  $d_i$  and  $d_j$  denote the diameters of type- $i$  and type- $j$  particles,  $k_B T$  is the thermal energy,  $\eta$  is the viscosity of the surrounding fluid,  $G$  is the mean shear rate due to mechanical agitation,  $\Delta\rho$  the density difference between the particle and the fluid, and  $g$  is the acceleration due to gravity.

From comparison of the general trends of equations 2.22-24, it is obvious that the perikinetic collision constant is decided by the size ratio but not the absolute size of the particles. In contrast, collision constants in the orthokinetic and sedimentation cases show very strong size-dependence — varying roughly as  $d^3$  in the case of orthokinetics and  $d^4$  for differential settling. Therefore, although the choice of different values for shear rate and density can change the outcome of calculating collision rate constants, the general rules would be that: Brownian motion is predominant for submicron particles; the growth of medium-size aggregates is dominated by orthokinetic effects; and differential sedimentation may become dominant for even larger particles.

### 2.2.2 Collision efficiency

It is important to point out that the discussions in Section 2.2.1 were predicated on the assumption that, without interaction barriers, every collision is effective and results in so-called *rapid aggregation*. In practice, *slow aggregation* often occurs at a much lower rate due to the existence of interaction barriers which prevent particles from actual contacts. As such, only a fraction of the collisions will lead to aggregate formation; this fraction is defined as the *collision efficiency* ( $\chi$ ). In many textbooks, the reciprocal of the collision efficiency, referred to as the *stability ratio*  $W$ , is often used. Therefore, the analysis of slow aggregation kinetics involves incorporation of an additional collision efficiency factor into the collision frequency expression (eqn 2.21):

$$f_{ij}(\text{slow}) = \chi_{ij} f_{ij}(\text{rapid}) = \chi_{ij} K_{ij} n_i n_j \quad (2.25)$$

It is obvious that the collision efficiency shall depend on the form and height of the interaction barrier. Generally, two forms of interaction barriers come into effect: (1) colloidal interactions; (2) hydrodynamic interactions. Many attempts have been made to predict collision efficiency on the basis of colloidal interactions (such as VDW and EDL interactions). The work in their relationship was first treated by Fuchs [1934] and later confirmed by Higashitani et al. [1978], who proposed a mechanism of slow perikinetic aggregation of non-deformable and spherical particles in dilute dispersions and derived the following formulation for the  $\chi$  (or  $W$ ):

$$W = 1/\chi = d \int_0^{\infty} \frac{\exp[V_T(h)/k_B T]}{(h+d)^2} dh \quad (2.26)$$

Here,  $d$  is the particle diameter,  $h$  is the particle separation distance,  $k_B T$  is the thermal energy, and  $V_T$  is the total potential energy barrier. As rough estimates, maximum  $V_T$  values of 0 and  $15 kT$  would produce collision efficiency  $\chi$  of 1 and  $10^{-5}$ , respectively. A lower value of  $\chi$  implies a more stable system. When  $V_T$  is calculated by the appropriate expressions on basis of classic DLVO theory, a plot of  $\log(1/\chi)$  vs  $\log c$  (where  $c$  is the bulk electrolyte concentration) would be obtained. It was shown that this plot should be linear and its slope should be proportional to the particle size [Reerink & Overbeek 1954]. However, in practice, it is very difficult to reconcile the measured  $\log(1/\chi)$ - $\log c$  plots with DLVO theoretical predictions. In particular, the measured  $\chi$  values were either much lower or much higher than what classic DLVO theory predicts; the proportionality of  $d[\log(1/\chi)]/d(\log c)$  with particle size was not observed; the critical aggregation concentration significantly depended on particle size [Prieve & Lin 1982; Penners & Koopal 1987; Shulepov & Frezs 1995]. These discrepancies can be attributed to the presence of surface roughness and charge heterogeneity and/or to other colloidal interactions.

Here, it should also be pointed out that another important contribution to slow aggregation is from hydrodynamic drag forces related to the viscous nature of the suspending fluid [Vandeven & Mason 1976; Chung & Hogg 1985; Danov et al. 1993]. When two approaching particles come into close proximity, the viscous dissipation of the fluid in between the gap creates a resistance which slows down the velocity of approach; this is the so-called *hydrodynamic force* which could decrease the diffusion rate and therefore collision efficiency [Cameron 1981]. In the case of perikinetic aggregation, such hydrodynamic effects are often taken into account as the reduced diffusion correction factor  $\varpi(h)$  that was

incorporated into the above Fuchs expression (eqn 2.26), and the collision efficiency would be obtained through integration [Spielman 1970; Honig et al. 1971]. If other transport mechanisms — such as fluid motion or sedimentation — are considered, there will be even greater challenges in the theoretical calculation of collision efficiencies, and sometimes it becomes impossible due to the complex interplay of many factors (such as hydrodynamic and colloidal interactions) [Gregory 1989]. In this study, collision efficiency was equated to the probability of coalescence between two bitumen droplets under quiescent conditions (i.e. in the absence of hydrodynamics). In order to simplify the situations (e.g. avoiding transport effect), we grasped two individual droplets and cause them to make oblique contact with precise motion control.

### **2.3 Studies on bitumen coalescence**

The aforementioned discussion dealt with the broad subject of general colloids. Here, we are interested in bitumen-in-water dispersion. We will focus on the existing studies on the coalescence mechanisms of bitumen droplets in aqueous medium; there are very few such studies. Among them, Wu et al. investigated the interactions between micron-sized bitumen droplets in water by employing two novel force measurement techniques: *colloidal particle scattering* (CPS) [Wu et al. 1999a] and *hydrodynamic force balance* (HFB) [Wu et al. 1999b], which have the capability of determining extremely weak colloidal forces (1 pN). Measurements from the two methods suggested the Hamaker constant for bitumen-water-bitumen systems to be roughly  $3.2 \times 10^{-21}$  J, which agreed well with the calculated value based on DLVO theory (suggesting no other colloidal forces were involved). However, they detected a larger repulsive force than expected from the classical DLVO theory, assuming

smooth interacting surfaces. The extra force was attributed to the effect of heterogeneous protrusions on the bitumen surface that were 50-100 nm in diameter and 0 to 20 nm in thickness, according to SEM images. Laroche et al. [2000] used the two same methods and reported even more repulsive forces than what was predicted by the disk-protrusion model [Wu et al. 1999a and 1999b]. Instead, the data could be explained adequately by a steric interaction model due to the existence of hair-like structures on the bitumen surface. To investigate the effect of adding asphaltene-modified clay, they also found that an additional steric layer outside the clay shell was required to explain the even larger repulsive forces. A similarly strong non-DLVO repulsive force was found in the impinging jet experiments conducted with bitumen droplets and bitumen-coated collectors [Sanders et al. 2003]. Aksoy [1997] and Yoon et al. [1995] used a surface force analyzer to quantify bitumen-bitumen interactions in water and the corresponding “induction times.” They concluded that, even though very strong repulsive forces were detected at separation distances of less than 70 nm, drop coalescence did occur at very slow rates. It was suggested that the mechanisms which promoted coalescence were attractive van der Waals interactions and short-range (1-2 nm) hydrophobic forces. Salou et al. [1998] also applied the non-DLVO force model to bitumen emulsions, with extra solvent-structural terms due to the hydration and hydrophobic interactions. They postulated that these different interactions were due to the bare and surfactant-covered regions which coexisted on the bitumen surface. The regions covered with surfactants displayed a hydrophilic character, whereas the bare regions maintained the hydrophobic character of bitumen.

Another important mechanism behind bitumen coalescence in water had recently been suggested by Yeung and coworkers [Yeung et al. 2003; Esmaeili 2009], who introduced the model of surface charge heterogeneity in the study of bitumen-water interface. They had shown in the two relevant studies using micropipettes that, despite overwhelmingly large electrostatic repulsive forces, coalescence between the oil droplets did occur. Furthermore, the coalescence process was not deterministic. It was first observed that two identical drops in head-on contact coalesced very occasionally but their coalescence was much more likely in the case that they were brought into an oblique contact. But this first work was basically on qualitative observation, with very little quantitative detail [Yeung et al. 2003]. Later, by conducting “head-on” contact experiments, the probabilities of coalescence between two droplet pairs with identical size were quantified at room temperature. From this work, it was evident that the tendency for coalescence was strongly dependent on the degree of deformation and drop size (larger drops were more likely to coalesce). Findings from this study also suggested that the traditional DLVO theory remained sound for explaining the coalescence behavior, but surface charge heterogeneities at the oil-water interface must be considered [Esmaeili 2009]. This previous analysis, however, did not account for the motions created by oblique collision (which are important in practice, especially during slurry transport).

The aim of this work is to develop experimental methods for examining the role of shear on the coalescence of bitumen droplets immersed in an aqueous environment (of varying ionic strengths and pH). Also, we will apply the probabilistic model that incorporated charge heterogeneity into the DLVO-based theory for interpreting the observed shear-induced

coalescence phenomena. The next sections which immediately follow will be devoted to a review of the classical DLVO prediction of the coalescence behaviors between two bitumen droplets in aqueous media. It will be seen that this classical theory fails rather miserably in explaining the coalescence behavior in our systems. We will then modify the theory by including charge heterogeneities in the bitumen-water interface, and develop a new probabilistic model.

### **2.3.1 Prediction from classical DLVO theory**

Details of applying the classical DLVO theory to analyze “head-on” contacts between two *similarly sized* bitumen droplets (both  $\sim 10\ \mu\text{m}$  in diameter) in water were outlined by Yeung et al. [2003]. In this present study, two *distinctly sized* bitumen droplets ( $\sim 0.1$  and  $1\ \text{mm}$  in radius) are brought together and made “oblique contact,” and the probability of coalescence is examined. This oblique contact experiment will be discussed in the next chapter (Section 3.3) and it is simply illustrated here in Figure 2-4.

The two bitumen droplets are subjected to various forces (external and colloidal) that determine the nature of their interaction with each other. The possible forces that are at play, and their order-of-magnitude estimates in the current system, are listed in the following [Masliyah 2007]:

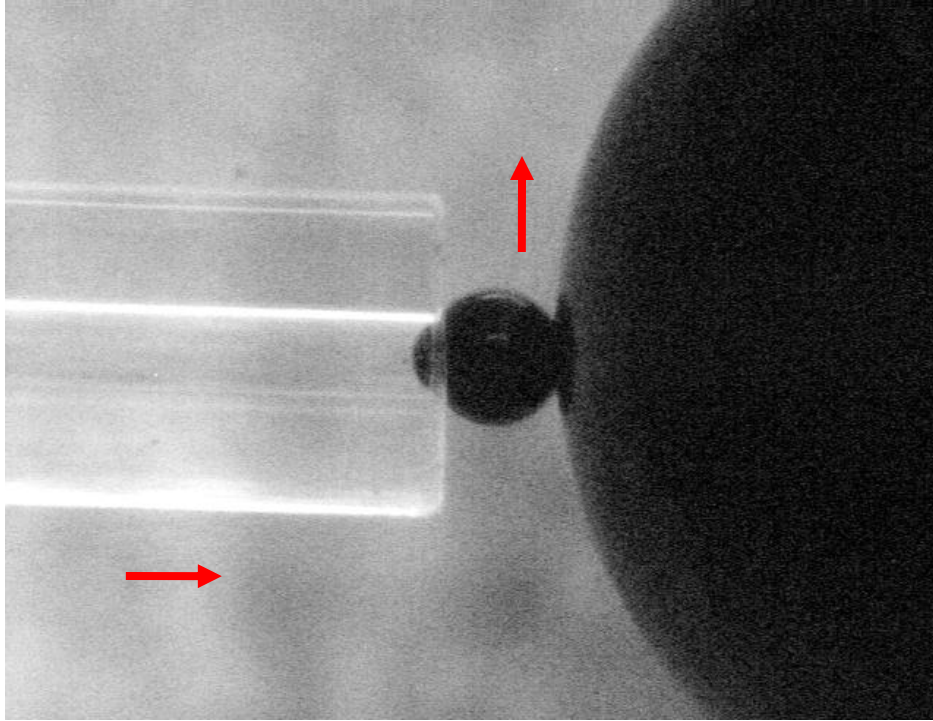


**Figure 2-4: Typical image of showing two bitumen droplets (~0.1 and 1 mm in radius) pressed together using micropipettes.** The suspending medium is “simulated process water” (SPW) of varying  $[Ca^{2+}]$  and pH. The amount of deformation of the droplets, shear distance and shear speed can be precisely controlled. This typical “oblique” (or sliding) contact may or may not result in the coalescence of the droplets; the process is, in essence, stochastic.

(1) *Buoyancy force*: This is proportional to  $\Delta\rho g r^3$ , where  $r$  is the radius of the bitumen droplets ( $\sim 100 \mu\text{m}$  for small droplet);  $\Delta\rho$  is the differential density between bitumen and water ( $\sim 10^2 \text{ kg/m}^3$ ); and  $g$  is gravitational acceleration ( $\sim 10 \text{ m/s}^2$ ). As such, the gravity force is estimated to be 1 nN. Note that the gravity force is perpendicular to the direction of contact between two droplets and would not exert direct impact on the coalescence process.

(2) *Inertial force*: This is due to the movement of oblique contact and is given by  $\Delta p r^2 v^2$ , where  $v$  is the speed of shear contact ( $\sim 150 \mu\text{m/s}$  maximum). As such, the inertial force is order of  $10^{-5}$  nN.

(3) *Viscous force*: This is due to the viscous nature of fluid that drags the oblique movement and is presented as  $\eta r v$ , where  $\eta$ , the viscosity of the aqueous solution, is  $\sim 10^{-3}$  Pa·s; the resulting viscous force is order of  $10^{-2}$  nN.

(4) *Brownian force*: It is due to thermal agitation of bitumen molecules and estimated as  $k_B T / r$ , where  $k_B T$ , the thermal energy, is  $4.17 \times 10^{-21}$  J at room temperature, which result in Brownian forces of order  $10^{-8}$  nN.

(5) *Compressive force*: This is certainly of importance to the current system. This force, which is created by pressing together two liquid spheres (bitumen drops) using micropipettes, depends on the interfacial tension and the amount of deformation; it can be estimated to be of order  $\Delta p r_c^2$ , where  $r_c$  is the radius of the contact region ( $\sim 5 \mu\text{m}$  for the small droplet having radius of  $100 \mu\text{m}$  and deformation ratio (DR) of 1.1; see Appendix A) and  $\Delta p$ , the pressure difference across the bitumen-water interface, is calculated from the Young–Laplace equation

$$\Delta p = 2\gamma / r_1 \quad (2.27)$$

where  $r_1$ , the radius of the small drop, is  $\sim 100 \mu\text{m}$ . The bitumen-water interfacial tension  $\gamma$  is of order  $\sim 10^{-2}$  N/m [Moran et al. 2000a]. Therefore, the compressive force is estimated to

be 10 nN. Comparing with the aforementioned forces, the compressive force is clearly the most significant. To determine if this compression is strong enough to cause coalescence, we should compare it with the threshold value set by the colloidal forces. This will be done in what follows.

(6) *Colloidal forces*: In this study, the van der Waals and electrical double layer forces are considered to be the only two colloidal forces involved. In accordance with this classical DLVO picture, the LSA result for the DLVO forces  $F_T(h)^{\ddagger\ddagger}$  between two distinctly sized bitumen spheres with radii  $r_1 \sim 100 \mu\text{m}$  and  $r_2 \sim 1 \text{mm}$ , zeta potentials  $\zeta_1$  and  $\zeta_2$ , and at very close separation distance  $h$  ( $h \ll r_1$  or  $r_2$ ) can be derived using Derjaguin's approximation from eqn 2.19 with the multiplication of the factor  $2\pi r_1$ ; it can be approximately written as [Butt et al., 2003]

$$F_T(h) \approx 128\pi \cdot \kappa^{-1} r_1 n^0 k_B T \cdot \tanh\left(\frac{ze\zeta_1}{4k_B T}\right) \cdot \tanh\left(\frac{ze\zeta_2}{4k_B T}\right) \exp(-\kappa h) - \frac{A_{212} r_1}{6h^2} \quad (2.28)$$

where  $z$ , the ionic valence, is equal to 1 (the concentration of divalent ions in this study is relatively small and can be neglected);  $n^0$ , the number concentration of positive or negative ions in solution, is  $\sim 2.4 \times 10^{25} / \text{m}^3$  (neglecting the concentration of divalent and pH-determining ions);  $e$ , the elementary charge, is  $1.6 \times 10^{-19} \text{C}$ ; the thermal energy  $k_B T$  is  $4.17 \times 10^{-21} \text{J}$  at room temperature; the Debye length  $\kappa^{-1}$  for a 1:1 electrolyte at room temperature is given by

---

<sup>‡‡</sup> Retardation effect of VDW force is not considered due to sufficiently small separation distance.

$$\kappa^{-1} = \frac{0.304}{\sqrt{I}} \text{ (nm)} \quad (2.29)$$

where the ionic strength  $I$  of the electrolyte is in mol/L. For a typical electrolyte of  $I = 44$  mM, the resulting Debye length is  $\sim 1.45$  nm. (The ionic strength  $I$  of the electrolyte increased only slightly — from 44 mM in absence of  $\text{Ca}^{2+}$  ion to 46 mM at the maximum  $\text{Ca}^{2+}$  concentration.) The Hamaker constant  $A_{212}$  for bitumen-water-bitumen system is typically one  $k_B T$  [Hunter, 1986]. (Note that the Hamaker constant can be calculated based on the optical properties of the suspended material and is basically insensitive to the type and concentration of ions in the electrolyte; Gregory 1989.) Using the above values and leaving zeta potentials  $\zeta_1$  and  $\zeta_2$  as adjustable parameters, the curves of the total DLVO forces  $F_T(h)$  as function with the separation distance  $h$  are plotted in Figure 2-5.

In general, it is shown from Figure 2-5 that the DLVO force curves can be described by three important regimes: (1) very weak attraction occurring at large distances (the *secondary force minimum*, shown in the insert). This secondary minimum may result in weak and reversible aggregation without substantial drainage of the thin liquid film between the droplets. (2) The electrostatic repulsion outweighs the van der Waals attraction at intermediate ranges of separation, giving a *force barrier height* (maximum in the repulsion force curve). This barrier would provide colloidal stability; coalescence will occur only if an external force can overcome this threshold. (3) If the barrier is overcome, a strong attraction depth would be seen at very close distances (the *primary force minimum*). This primary minimum would make the aggregation irreversible, and re-dispersion is unlikely to occur from this point.

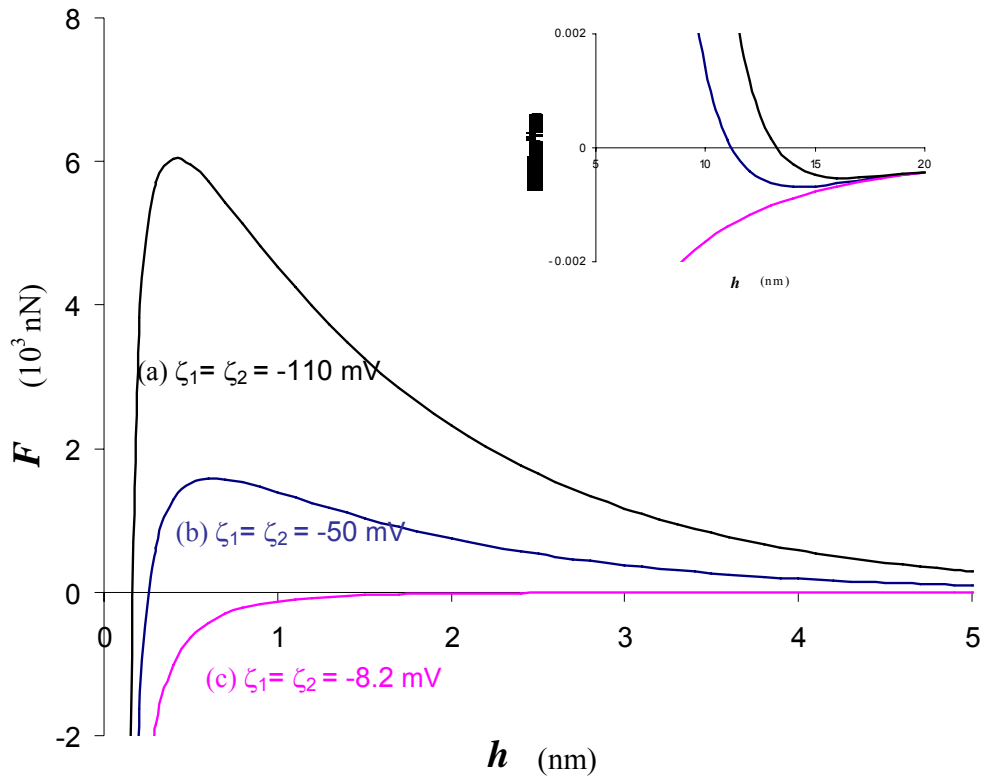


**Figure 2-5: Series of curves showing colloidal forces ( $F$ , in unit of  $\mu\text{N}$ ) versus distance ( $h$ , in nm) between two distinct bitumen spheres (with radii 0.1 mm and 1 mm) in aqueous electrolytes ( $\kappa^{-1} = 1.45 \text{ nm}$ ). The calculation is based on classical DLVO theory using eqn 2.28. Zeta potentials of bitumen droplets  $\zeta_1$  and  $\zeta_2$  are the only adjustable parameters.  $F > 0$  implies a net repulsion, while  $F < 0$  denotes attraction. The insert shows the very weak attractive force (secondary force minimum) at very large distance. The peaks of the two force curves (approx.  $10^3 \text{ nN}$  in case  $b$ ;  $6 \times 10^3 \text{ nN}$  in case  $a$ ) are the two extreme force barriers that must be overcome for coalescence to occur in the current problem. The curves ( $a$ ) and ( $b$ ) are plotted using the minimum and maximum absolute values of zeta potentials of bitumen droplets in simulated process water (see Chapter 4). In order to overcome the force barrier, which is shown in curve  $c$ , zeta potentials of opposing surfaces must satisfy equation 2.33 in which  $(\zeta_1 \zeta_2)^{1/2} < 8.2 \text{ mV}$ .**

As seen in all three force curves, the trend is that the repulsive force barrier height decreases with decreasing zeta potentials. Therefore, in order to eliminate the barrier and allow coalescence (primary force minimum) to achieve, the practical way is to decrease the electrostatic repulsion so that the VDW force is strong enough to overtake the repulsive term; and as shown in the figure 2.5, this can be obtained by decreasing zeta potentials of opposing surfaces (in absolute magnitudes). As these potentials are lowered, there comes a point below which the total DLVO force  $F_T$  would be negative and monotonically decreasing with the separation distance  $h$  (see curve  $c$  in Figure 2.5). Mathematically, below this point, the following two formulas must be satisfied for all the separation distance  $h$  in accord:

$$F_T(h) < 0 \quad (2.30)$$

$$\frac{dF_T(h)}{dh} < 0 \quad (2.31)$$

For convenience, we incorporate the approximate expression of eqn 2.28 into the above two formulas for calculating the necessary “smallness” of these potentials (note that the zeta potentials do not need to vanish for destabilization to occur). After some algebra, one arrives at the following expression [Yeung et al. 2003]:

$$\tanh\left(\frac{ze\zeta_1}{4k_B T}\right) \cdot \tanh\left(\frac{ze\zeta_2}{4k_B T}\right) < \frac{(2.718)^4 A_{212} / k_B T}{32768\pi n_0 \kappa^{-3}} \quad (2.32)$$

Regarding the physical quantities on the two sides of eqn 2.32, we will apply the same values as quoted previously in this subsection. By making the approximation  $\tanh x \approx x$  in eqn 2.32, it can be shown that, for the net DLVO force to be attractive over the entire distance range, the interacting zeta potentials should satisfy the condition

$$\zeta_1 \zeta_2 < 66.5 \text{ mV}^2 \quad (2.33)$$

In other word, assuming there are only DLVO forces (i.e. only EDL repulsion and VDW attraction), coalescence between bitumen droplets would occur if  $(\zeta_1 \zeta_2)^{1/2}$ , the geometric average of the zeta potential, is less than approximately 8.2 mV<sup>§§</sup>

Note that the compressive force is applied to the thin aqueous film between droplets in this study. Let us have a close look at Figure 2-5 again. Another important feature of the figure is the force barrier height for the current problem. As will be shown in Chapter 4, the zeta potentials on the bitumen drop surfaces in simulated process water (SPW) is roughly between 50 and 110 mV (absolute values — the  $\zeta$  's are in fact negative); these two numbers are used to plot the curves (b) and (a) in Figure 2-5. The curves clearly suggest that the force barrier heights are at least of order  $10^3$  nN; such a barrier is the threshold which the compressive force must overcome to attain coalescence. Yet, the compressive force, as discussed earlier, is no more than 10 nN — at least two orders of magnitude weaker than the threshold barrier. As such, the compressive force is far too weak to cause any coalescence. It should also be pointed out that, if the bitumen-water interface were indeed homogeneous (classical DLVO assumption), “oblique contact” between the bitumen surfaces would not help at all in promoting coalescence — sliding one surface over the other will not alter the compressive force. Hence, we come to conclusion that, according to classical DLVO theory, there should be no coalescence at all under all experimental conditions in this study (i.e. for  $|\zeta|$  between 50 and 110 mV). However, it is known from experiments that bitumen droplets *do* coalesce stochastically, with the coalescence probability increasing dramatically with larger contact areas (e.g. as a result of longer distance of oblique contact; see Chapter 4). In order to

---

<sup>§§</sup> Note that the LSA boundary condition was used to approximate this value. If using CC or CP boundary condition for DLVO calculation, very similar number would be obtained.

explain such significant discrepancies, we will “relax” the implicit restrictions placed on models which conform to the classic DLVO theory — that the surfaces are homogeneous in terms of both geometric smoothness and uniform charge distribution. For liquid-liquid interfaces, as it is in this case, the assumption of geometric smoothness is likely acceptable [Walz 1998]. However, claiming uniform surface charge on a very viscous (essentially solid) interface is perhaps no more than “wishful thinking”; charge heterogeneity on the bitumen-water interface will likely arise due to different local distributions of ionized or adsorbed functional molecules and compounds. In this regard, the  $\zeta$ -potential obtained from electrophoresis (see Chapter 4) is in fact the averaged value over the whole surface. Despite the apparently large *surface averaged*  $\zeta$ -potential, it is very likely that sufficiently low  $\zeta$ -potential domains (or “patches”) will exist over the surface. It follows that coalescence between bitumen droplets may easily be induced by surface charge heterogeneity: we can imagine when two opposing patches, with local  $\zeta$  potentials satisfying condition (2.33), get the chance of “meeting” each other, the net interaction would become attractive across these two patches. This will lead to local rupture of the thin water film and the formation of an oil bridge connecting the two bitumen drops (called here a *local breach*). Once this connection forms, coalescence will evolve irreversibly as two bitumen droplets fuse into one to minimize the surface free energy. It is also noted that sliding one surface over the other will create larger contact area, which in turn significantly increases the chances of local breaches. As discussed earlier in Section 2.2.4.1 (II), this assumption of charge heterogeneity will aid in capturing many behaviors of the coalescence process that appears to be in direct contradiction with the classical DLVO theory. In what follows, we will put forward a quantitative model of surface charge heterogeneity.

### 2.3.2 Surface charge heterogeneity model.

Yeung and coworkers (including the present author) have developed a theoretical model of surface charge heterogeneities for bitumen-water interfaces [Esmaeili et al. 2012]. In this model, the bitumen drop surface is assumed to be covered with many *local patches* of equal area; the size of each patch is characterized by a length  $L$ . It is further assumed that the zeta potential on each patch, represented by the symbol  $\zeta_i$ , is a *random variable* that is statistically uncorrelated with the zeta potentials of the neighboring patches. A schematic of this model is shown in Figure 2-6:

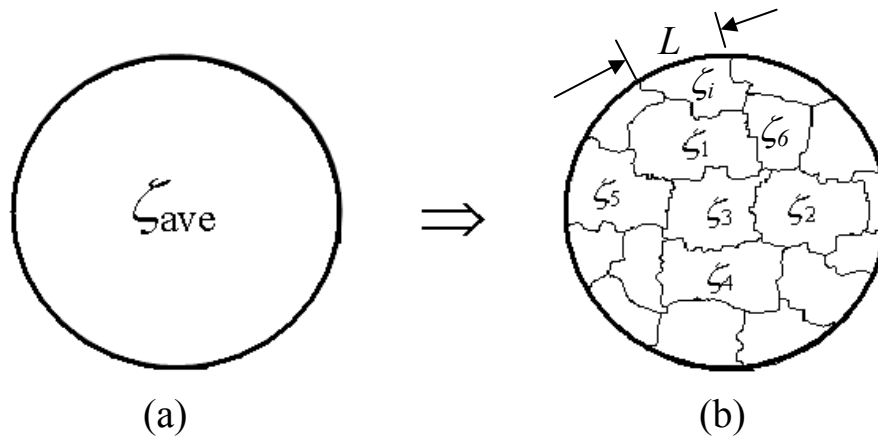


**Figure 2-6: Schematic of modeling (b) heterogeneously distributed charges on surface of a bitumen sphere containing (a) surface-averaged potential  $\zeta_{ave}$ .** Each patch possesses unique *local* zeta potential ( $\zeta_i$ ) for characteristic *length scale* ( $L$ ). The value  $\zeta_{ave}$  can be determined from electrophoresis (see Chapter 3 for detailed procedure and Chapter 4 for results).

As a simplest representation, we assume the random variable  $\zeta_i$  to be Gaussian, characterized by a mean  $\zeta_{\text{ave}}$  and a standard deviation  $\sigma_\zeta$ . For two such random variables  $\zeta_1$  and  $\zeta_2$ , the *joint probability density function*  $f$  is given by the standard form

$$f(\zeta_1, \zeta_2) = \frac{1}{2\pi\sigma_\zeta^2} \exp\left[-\frac{(\zeta_1 - \zeta_{\text{ave}})^2 + (\zeta_2 - \zeta_{\text{ave}})^2}{2\sigma_\zeta^2}\right] \quad (2.34)$$

Inherent in equation (2.34) is the assumption that  $\zeta_1$  and  $\zeta_2$  are statistically uncorrelated. The function  $f(\zeta_1, \zeta_2)$  is just the three-dimensional analogue of a simple Gaussian; a plot of this axisymmetric probability density function is shown in Figure 2-7. Equation (2.34) is normalized in that the volume under the bell-shaped dome in Figure 2-7 is unity.

Imagine now a situation where two bitumen droplets are pressed together; the flattened region is effectively two planar bitumen slabs separated by a thin layer of aqueous film. According to our patchy surface model, there will be many pairs of charged patches — one from each bitumen drop — interacting across the water film. We insist that the colloidal interaction between two opposing patches obey the classical DLVO theory. Let us recall relation (2.33), which is the condition for a *local breach* to occur. Geometrically, relation (2.33) is represented by a hyperbola in the  $\zeta_1 - \zeta_2$  plane; this is depicted as the red region in Figure 2-7.

We now define  $\varphi$  to be *the probability that a local breach occurs*. Combining relations (2.33) and (2.34), one can readily write

$$\varphi = \int_{\zeta_1 \zeta_2 < 66.5 \text{mV}^2} f(\zeta_1, \zeta_2) d\zeta_1 d\zeta_2 \quad (2.35)$$

Graphically,  $\varphi$  is the volume under the joint probability density function within the red hyperbolic region in Figure 2-7 ( $\varphi$  is the 3-D analogue of the error function).

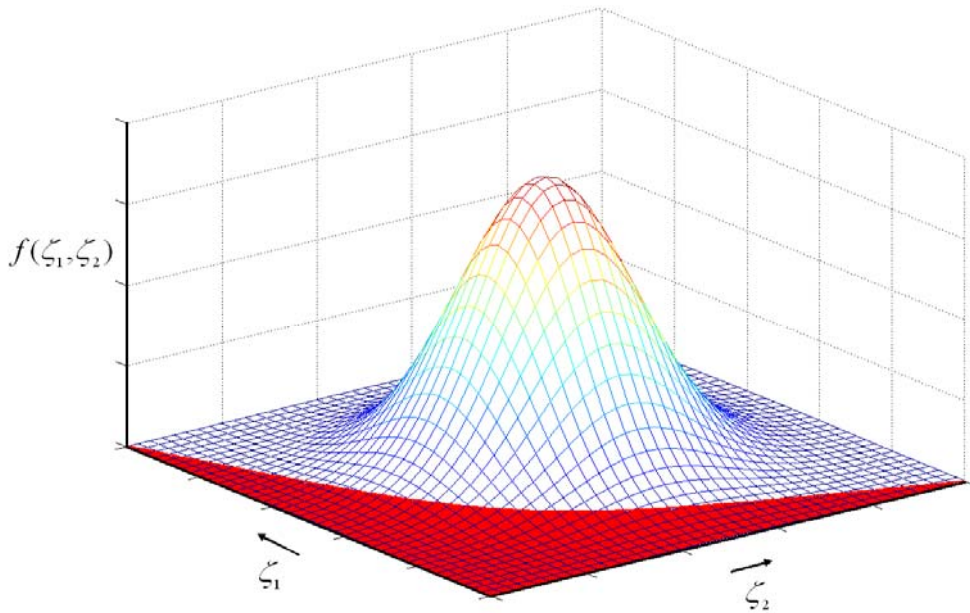


**Figure 2-7: The 3D picture depicts the probability density function of two Gaussian variables.**

The horizontal axes are  $\zeta_1$  and  $\zeta_2$  denoting the zeta potentials of the two interacting patches, and the vertical axis is  $f(\zeta_1, \zeta_2)$  signifying the joint probability density function quoted in eqn. 2.34. The red hyperbola line sketches the local destabilization criterion quoted in eqn. 2.33. The volume under the joint probability density within the red hyperbolic region is regarded as the local probability ( $\varphi$ ) of coalescence. (Adapted from Esmacili et al. 2012)

Now image that a small bitumen droplet is pushed against a much bigger drop (e.g. using micropipettes) and is made to slide along the big drop's surface (see Figures 2-4 and 4-1).

Because the bigger drop is much more deformable (due to a much lower Laplace pressure across the bitumen-water interface), we may assume that only the large drop deforms to any appreciable extent, while the small droplet maintains its shape of spherical cap throughout the gliding process (up to the moment of coalescence, if it occurs). With these assumptions, it is possible to estimate the droplet-droplet contacted area  $AC$  (see Figure A-1) based on (1) the deformation ratio DR of the small droplet (defined as  $a/b$  in Figure A-1), and (2) the distance of shear contact  $H$ , given by eqn A.1 in Appendix A. (A longer sliding distance would lead to more accumulated contact over the sliding process.) Noting that every charged patch has a characteristic dimension  $L$ , we estimate that the area of each patch is given roughly by  $L^2$ . As such, a contact process between two bitumen drops (in our case, the sliding of one drop over the other) would give rise to  $N$  “colloidal interactions” (between charged patches facing each other across a water film), where  $N$  is expressed simply as

$$N = AC/L^2 . \quad (2.36)$$

Out of the  $N$  pairs of opposing patches, if only *one* pair were “locally breached,” the stable thin film would collapse and the two droplets would coalesce irreversibly. To capture this fact, we further define a *global probability* of coalescence  $\Phi$  as follows:

$\Phi \equiv$  the probability that, out of the  $N$  pairs of opposing patches, *any one or more* pairs will *locally breach*.

Given that the  $N$  patch-pairs are statistically independent, the relation between local and global probabilities can be easily derived as:

$$\Phi = 1 - (1 - \varphi)^N . \quad (2.37)$$

With  $N$  given by eqn 2.36, the theoretical probability of coalescence  $\Phi(\text{theo})$  can be written as

$$\Phi(\text{theo}) = 1 - (1 - \varphi)^{AC/L^2} \quad (2.38)$$

where the local probability  $\varphi$  is obtained from numerical integration of eqn (2.35).

Regarding the four parameters that are required to calculate  $\Phi(\text{theo})$ : the value  $\zeta_{\text{ave}}$  is equated to experimentally determined zeta potential (e.g. by electrophoresis), and  $AC$  is estimated from droplet contact mechanics (described in Appendix A); the parameters  $\zeta_{\text{ave}}$  and  $AC$  are thus considered known. This leaves the present model with two remaining undetermined parameters, namely, the zeta potential standard deviation  $\sigma_\zeta$  and the patch size  $L$ . If given the values of  $\sigma_\zeta$  and  $L$  on trial runs, one can readily calculate  $\Phi(\text{theo})$  under different experimental conditions and compare them to their experimental counterparts  $\Phi(\text{exp})$ .<sup>\*\*\*</sup> For such a comparison, it is convenient to define the following least squares functional (denoted  $\Omega$ ):

$$\Omega \equiv \sum_{i=1}^M [\Phi_i(\text{theo}) - \Phi_i(\text{exp})]^2 \quad (2.39)$$

The summation of eqn 2.39 is from 1 to  $M$ , where  $M$  is the number of experimental data points that should be compared to theory. A vanishing  $\Omega$  would mean there is perfect agreement between theory and experiment; this, unfortunately, will never occur. By minimizing  $\Omega$  with respect to  $\sigma_\zeta$  and  $L$ , we will obtain “optimal” values of the unknown parameters ( $\sigma_\zeta$  and  $L$ ) and thereafter predict coalescence probabilities  $\Phi(\text{theo})$  between bitumen droplets under a variety of conditions (e.g.  $[\text{Ca}^{2+}]$ , pH, distance of shear contact).

---

<sup>\*\*\*</sup> The values  $\Phi(\text{exp})$  will be determined experimentally as the number of successful coalescence divided by the total number of contact events; see Chapter 3 and 4.

It had clearly been seen that, in order to calculate the theoretical coalescence probabilities, two important heterogeneity parameters,  $\sigma_{\zeta}$  and  $L$ , need to be indirectly determined by fitting theory to experiment. In order to verify their actual existence, direct determination of these parameters using, for example, atomic force microscopy (AFM) is also worthwhile. The relevant AFM measurement procedures and results will be given in Chapter 3 and 4, respectively.

## Chapter 3 : Experimental

### 3.1 Materials

In this study, bitumen-in-water dispersions were prepared for experimental investigation. In this dispersion, the dispersed phase was the so-called solids free bitumen as treated with removing submicron clay particles from the “coker-feed” bitumen which was supplied by Syncrude Canada. The solids removal procedure was done first by diluting the “coker feed” bitumen in toluene (reagent grade, Fisher Scientific) with 1:9 weight ratio, and centrifuging the solution (Thermo Electron Corporation, model RC 6 Plus) at an acceleration of  $5 \times 10^5$   $\text{m/s}^2$  for one hour. All solid particles bigger than 30 nm were reasonably considered to be settle to the bottom of the solution (according to the simple calculation based on Stokes law). The removal of toluene was achieved by leaving the solids free supernatant in clean fume hood for evaporation until the initial weight of bitumen was recovered.

The continuous phase, an aqueous background electrolyte, was the so-called simulated process water (SPW) which comprised 25 mM NaCl (>99% purity), 15 mM  $\text{NaHCO}_3$  (99.9% purity), and 2 mM  $\text{Na}_2\text{SO}_4$  (99% purity) into ultra pure deionized water to mimic the actual water chemistry in commercial oil sand processing; its pH values was determined to be  $8.2 \pm 0.2$ . Dilute NaOH solution (0.1 M) was added into the above electrolyte to increase its pH to 10, while 0.1 M HCl solution to adjust to 6. The measurement of pH values was conducted in a digital pH probe (Accumet Research 20, Fisher Scientific). The amount of base or acid required to get the desired pH had negligible effects on the ionic strength of the final aqueous electrolyte. The concentration of  $\text{Ca}^{2+}$ , by doping with  $\text{CaCl}_2$  (anhydrous, 4-20

mesh), was also chosen as the adjustable parameter; its small addition was found not to affect the ionic strength and pH of the final solution. The above-mentioned salts and chemicals were obtained from Fisher Scientific. Sub-micron silicone nitride particle (particle size < 50 nm, with purity > 98 %) was purchased from Sigma-Aldrich and used as received.

## **3.2 Micropipette technique**

The micropipette technique, initially adopted from the field of biophysics for studying biology cells [Evans & Needham 1987], provides a means of examining the interactions between individual suspended droplets *in situ*. This technique was since introduced by Yeung and coworkers (our research group) to the research on emulsions and other engineering applications [Yeung et al. 1999 and 2003]. Here, the micropipette setup was further modified to suit the requirements of the present study (e.g. incorporation of digitally-controlled micromanipulators). Details of the present setup are described below.

### **3.2.1 Introduction of micropipette**

A basic schematic of the present experimental micropipette equipment setup is shown in Figure 3-1. A fine capillary tube (140  $\mu\text{m}$  i.d.  $\times$  500  $\mu\text{m}$  o.d.  $\times$  32 mm L, Microcaps, Aldrich), was glued in the centrally straightforward manner with a bigger capillary (800  $\mu\text{m}$  i.d.  $\times$  1200  $\mu\text{m}$  o.d.  $\times$  100 mm L, Microcaps, Aldrich) to make a suction pipette used in this study. For good accuracy, the finer end of pipette was truncated by hand cut to be a simple cylindrical geometry with no jagged imperfection under the view of video camera. To prevent contamination, the pipette was well rinsed with toluene, soaked in HCl solution for hours, and rinsed with pure water several times before filling aqueous electrolyte. To ensure

that bitumen drops and pipette surfaces were equilibrated with ion adsorption of a fresh aqueous medium, the pipettes were made for each condition studied.

A “sample cell,” namely, two parallel glass slides with a gap in between and two open faces on both ends, was constructed on the suitably designed sample stand (see blow-up view of Figure 3-1). Two suction pipettes were extended into the sample cell from opposite sides, such that their tips were facing each other. The pipettes were connected to plastic syringes via flexible tubing to allow for pressure control and also mounted on hydraulic micromanipulators. Both micromanipulators (one of which was manual, Narishige, model EMM-3SV; the other digitally controlled, SD Instruments, model MC2000), were able to enable accurate and smooth motions on the micron-scale. The video recording of the observed phenomena inside the sample cell was made using a video camera (Navitar) that had up to 15× magnifications and vertically mounted on three-axis movable stages. The Fta32 video and Image J software was uploaded on a personal computer linked to a LCD monitor, and the camera. Using this system, it was possible to clearly view the drops with over 50  $\mu\text{m}$ , to measure the size of drops and the distance of travel inside the sample, and to record the experimental observations in real time.

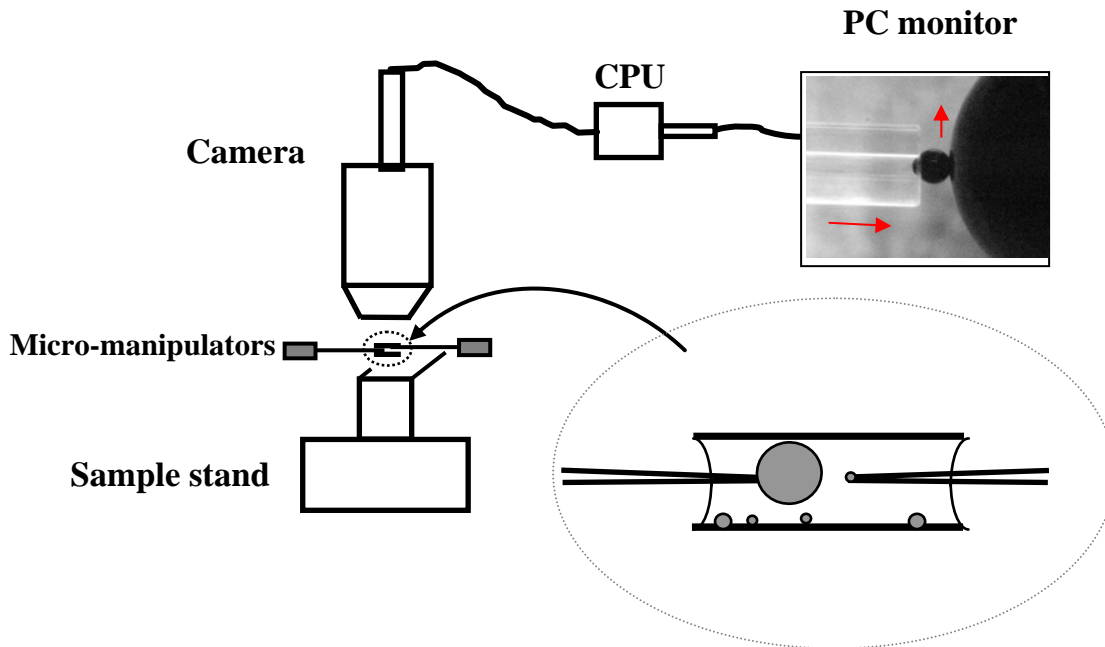


**Figure 3-1: Schematics of the micropipette experimental setup.** The bitumen-in-water suspension is placed in the glass cell (as illustrated in the blown-up view). Two individual bitumen droplets are grasped and controlled precisely into oblique contact by the micromanipulators.

### 3.3.2 Suspension preparation

The bitumen-in-water suspension for oblique contact experiment was prepared using the following procedures: (1) uniformly spread a small amount of “solids-free” bitumen (about 0.1-1.0 g) on the sidewall of a 20-mL vial by a clean and dry spoon; (2) dividing the spread bitumen into smaller regions using the tip of spoon, the amount of which was decided on what size of bitumen drops was desirable to produce; (3) adding 15 mL of an simulated process water (SPW) solution, into the vial; (4) immediately taking the vial into a water bath at 80°C and leaving it there for 10 to 30 seconds, followed by taking it out at room

temperature to stand for 20 minutes. As will be seen, due to different requirement for the “optimal” droplet size, this suspension preparation was a little different from that for  $\zeta$  potential measurement, which will be demonstrated in Section 3.4.2. In the current way, the resulting bitumen drops were spheres resting on the bottom of the vial and their sizes could range from hundreds of micrometers to several millimeters, depending on the amount of bitumen being spread and the size of regions being divided.

### **3.3.3 Oblique contact experiment**

An oblique contact experiment is shown in monitor image in Figure 3-1 (which is an actual video camera image). After filling the aqueous electrolyte together with syringe and silicon tubing, two suction pipettes were fixed in two capillary holders respectively. From the dispersion (approx. 3 mL in volume), one small bitumen drop was captured and held at the pipette tip which was mounted on the digitally controlled micromanipulator through suction pressure; the size of this bitumen drop was chosen on average to be in the range of 250  $\mu\text{m}$  (with less than 5% deviation). One bigger bitumen drop (approximately 2.5 mm of size) was caught by the other pipette tip with the manual micromanipulator. With the use of three-axis movable stages and two micromanipulators, the two bitumen drops were brought into clear view of the video camera, indicating that drops were located on the same height in  $z$ -direction axially. After the drops were recovered to the shape of a spherical cap, firstly the bigger drop was very slowly and carefully made to approach and contact the small drop (or the opposite movement was applied in some cases) in the  $x$ -direction until desirable small droplet deformation ratio (DR) was reached; then the small drop was set to slide on the surface of the bigger drop in the  $y$ -direction (this is referred to as the oblique contact

experiment). Here, the term “contact” refers to the visually observed contact between two drops, but it was understood that there was always a very thin liquid film between the drops in contact before coalescence (if it occurred). This oblique approach, which could be controlled at predetermined speeds (e.g. 1  $\mu\text{m/s}$ ), was designed to create shearing between the droplet surfaces. In addition to the speed of shear, the distance of shear contact ( $H$ ) between the droplets was also varied through the computer-controlled micro-motors. In the case of zero distance of shear contact ( $H = 0$ ), for each contact test, the bitumen droplets are held in contact at least 1 min; this is to allow sufficient time for any water thin film drainage in between bitumen droplets to fade out.

The coalescence probability of bitumen drops,  $\Phi(\text{exp})$ , were quantitatively determined by the oblique contact experiments described above. The video system recorded all the coalescence phenomena as seen on the PC monitor. If the two drops did not coalesce after oblique contact, they could be made to detach from each other. After repeating identical contact experiments with different drop pairs (typically 100 trials),  $\Phi(\text{exp})$  was calculated as the ratio of: the number of successful coalescences to the total number of contact trials

$$\Phi(\text{exp}) \equiv \frac{\text{number of coalescence}}{\text{number of contacts}} \quad (3.1)$$

### **3.3 Atomic Force Microscopy (AFM) technique**

The atomic force microscope (AFM) allows not only the imaging of surface topography at extremely high resolution, but also the measuring of force-versus-distance curves (referred to as *force curves* from here on); from these curves, valuable information on material surface

properties, such as adhesion, surface charge density and  $\zeta$ -potential can be obtained. In contrast to the major restriction of the electrophoresis technique (as will be discussed in Section 3.4), which only measures a *surface-averaged*  $\zeta$ -potential — regardless of whether the charge distribution is homogeneous or not, *local* variations (heterogeneities) in charge density or  $\zeta$ -potential, if any, can be directly quantified by the AFM technique as described here.

### 3.3.1 Introduction of AFM

In this section, the main focus is to describe the basic principles of measuring and analyzing AFM force curves; a good review in this area can be found in the work of Butt et al. [2005]. Some important issues, such as the determination of local  $\zeta$ -potentials and the relevant heterogeneity parameters interpreted from the force curves are also discussed. The AFM consists, in essence, of a laser diode, a position-sensitive photodiode detector (PSD), a piezoelectric translator (briefly called piezo), and a cantilever with a sharp tip, as illustrated in Figure 3-2.

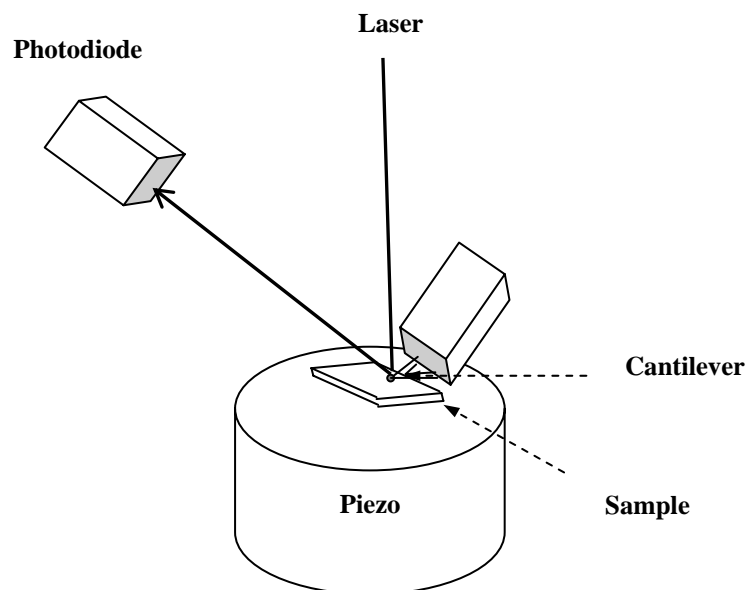


**Figure 3-2: Schematics of an Atomic Force Microscope.** (Adapted from Butt et al. 2003)

In a force measurement, the sample substrate mounted on the piezo is brought towards and away from the tip which is attached to the cantilever spring. The long-range colloidal forces and the adhesion (pull-off) force, if any, between the tip and the substrate, are respectively recorded for the approaching and retracting processes in one cycle. These interaction forces then cause the cantilever spring to deflect upwards or downwards, depending on the nature of the net forces between them. During a measurement cycle, the vertical displacement of the substrate is controlled and measured by applying a voltage to the piezo. On the other hand, the deflection of the cantilever is measured using the optical lever technique: the position of the laser beam reflected by the cantilever tip is monitored by the PSD and the corresponding photodiode current signal is shifted by an amount proportional to the cantilever deflection and the surface forces of origin. In fact, the raw data of a force measurement is only in terms of the relation of the photodiode current  $I_{\text{PSD}}$  versus displacement of the piezo  $Z_p$ , depicted as the  $I_{\text{PSD}} - Z_p$  curve in Figure 3-3a. To obtain a force curve,  $I_{\text{PSD}}$  and  $Z_p$  have to be converted in force  $F$  and distance  $h$  (the  $F - h$  curve sees the points in Figure 3.3b). Such a conversion can be performed with two methods: manual conversion or batch processing using AFM software (which is only available with expensive license purchase). Here, three parameters should be inferred from the raw data curve for the conversion: zero force, zero distance, and inverse sensitivity. As an example, a long-range repulsive force is considered (see Figure 3-3) and the substrate is non-deformable. The horizontal line of the non-contact part far away from separation is defined as zero force, implying negligible surface force; this is also called the baseline correction. The linear part of the “contact regime”, where  $I_{\text{PSD}}$  is linear with respect to  $Z_p$ , is assumed to be zero distance and its inverse slope is the inverse sensitivity

$\Delta Z_p / \Delta I_{\text{PSD}}$ . After the above definitions, the deflection of cantilever  $Z_c$  is obtained by multiplying the photodiode signal by the inverse deflection sensitivity:  $Z_c = I_{\text{PSD}} \times (\Delta Z_p / \Delta I_{\text{PSD}})$ , and the force  $F$  is calculated if the spring constant  $k_c$  of cantilever is known (i.e.  $F = k_c Z_c$ ). The separation distance  $h$  between the tip and the substrate is the addition of cantilever deflection and piezo position:  $h = Z_c + Z_p$ . Here,  $Z_p$  is defined as zero at the point where two linear parts of the raw curve are extrapolated to intersect. Details of such a conversion procedure are illustrated step-by-step in Appendix B.

After the conversion, the next stage is to extract valuable information from the force curve. We can fit the AFM-measured long-range force data (blue circle points in Figure 3-3b) to a theoretical model, e.g. classical DLVO theory; the theoretical equations for the DLVO forces between a pyramid-shaped AFM tip and a flat substrate will be presented in Appendix C. Assuming one knows all other fitting parameters (e.g.  $\zeta$  potential of the AFM tip is estimated from electrophoresis), the only unknown variable, the  $\zeta$  potential (or surface charge density) of the substrate, can be obtained with the best optimization of “curve-fitting.” After obtaining the  $\zeta$ -potential (or surface charge) at a local position, the tip is shifted laterally to another location (here, in 40-nm steps), and the procedure is repeated. In this manner, many force curves are measured and corresponding local  $\zeta$  potentials are inferred (see Section 3.3.3 for details). In the end, a map of the local  $\zeta$  potential variations, if any, can be constructed (see Figure 4-20 through 4-22). With the heterogeneous distribution of  $\zeta$  potentials, it is straightforward to calculate its mean value  $\zeta_{\text{ave}}$  of those local potentials.

The important heterogeneous parameter, namely the patch dimension  $L$ , can also be estimated from the series of randomly-distributed data. To do so, we define the measure of statistical correlation, if any, between a local  $\zeta$  potential and the neighboring  $\zeta$ 's (e.g. between  $\zeta_0$  at a reference point and  $\zeta_k$  for  $k \neq 0$ ). This results in an *autocorrelation function* (ACF) given by

$$\text{ACF}(k) = \{\zeta_0 \dots \zeta_k\} \quad (3.2)$$

where  $\{\dots\}$  denotes the strength of linear association between the two observations. With such notation, a series of ACF quantities are able to be mapped in a graph; this is also known as a *correlogram*, in which the ACF are plotted against the lateral distance ( $x$ ) on the surface. The magnitude of ACF lies in the range  $[1, 0]$ :  $\text{ACF} = 1$  implies that the data are perfectly correlated (i.e. deterministic), whereas  $\text{ACF} = 0$  suggests that the data are not correlated at all (i.e. purely random). A correlogram like those in Figures 4-23 to 4-25, where the values of ACF (in magnitude) comes gradually down from a highly degree of correlation (i.e.  $\text{ACF} \approx 1$ ) to poor correlation (i.e.  $\text{ACF} \approx 0$ ), suggests that the representing process is neither purely random nor deterministic [Chatfield 2004]. In the context of our patchy model for surface charge heterogeneities, recall that we had assumed the  $\zeta_i$ 's of the patches to be statistically independent. For this to be true, we must associate the characteristic patch size  $L$  to the decay length of the ACF. Note that with our current level of analysis, the most we can expect is for  $L$  (from fitting theory to coalescence probabilities) and the ACF decay length (from direct AFM measurements) to have the same order of magnitude. Making such a demonstration would already be a major triumph for our proposed patchy surface model.

The aforementioned discussion indicates the prospect of using the AFM for directly mapping surface charge heterogeneities on a substrate and acquiring the related heterogeneous parameters.

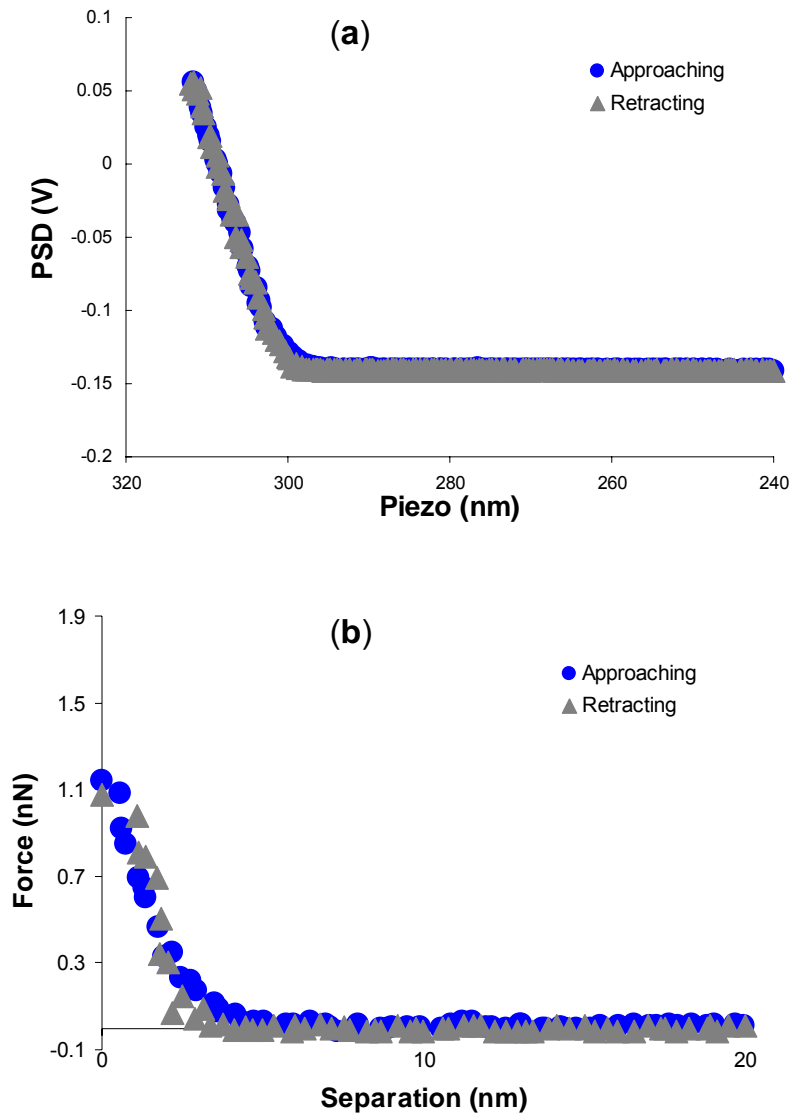


**Figure 3-3: Typical AFM force curves:** (a) photodiode current vs piezo-displacement curves, recorded from AFM; (b) force vs distance curves, converted from (a).

### 3.3.2 Bitumen substrate preparation

Note that the sample for an AFM force measurement is usually required to have a planar and smooth surface. In this study, the sample bitumen substrate was prepared by coating a thin layer of solid free bitumen on a silicon wafer with a P6700 spin coater (Specialty Coating System Inc.). The preparation method used here was a slight improvement from that of Liu et al. 2003. A silicon wafer was divided into roughly 2 cm × 2 cm square pieces; these pieces were immersed in chloroform overnight to eliminate potential organic contaminants, then rinsed with de-ionized water and ethanol, and finally dried with the blowing of ultra-pure grade nitrogen. The required bitumen solution was prepared with dissolving solids free bitumen in toluene at a concentration of about 0.5 wt%. During the spinning of the coater, about 1 mL of the bitumen solution was slowly dropped on the cleaned silicon piece at 1000 rpm for 20 s, and at 5000 rpm for 60 s. The bitumen substrate was further dried in a particle-free hood for at least 1 hr under ambient conditions. The thickness of the resulting bitumen layer was estimated to be about 100 nm [Liu et al. 2003].

In order to have evidence that the above preparation method was effective, X-ray photoelectron spectroscopy (XPS)<sup>†††</sup> was used to characterize the elements on the coated substrate and a typical XPS spectrum of this substrate is shown by the red line B in Figure 3.4. Comparing to that (black line A in Figure 3-4) of the clean silicon substrate, analysis of the two spectra showed that the silicon-element peaks at around 151 eV, and 100 eV bonding energies were highly intense in the spectrum of the clean silicon substrate but much depressed in that of the spin-coated substrate. Opposite scenarios were observed for the

---

<sup>†††</sup> XPS experiment in this work was performed by Dr. Anqiang He (technician at University of Alberta).

carbon-element peak at about 286 eV. In addition, the sulfur-element peaks at 165 eV and 229 eV bonding energies (see the blow-up view of Figure 3.4) were found, even weakly, for the spin-coated substrate. These different spectra clearly indicated coverage of a bitumen layer on the substrate by spin coating.

It was also important to verify that the coated bitumen surface was smooth and suitable for AFM force measurements. This was done by tapping-mode imaging using the Asylum Research MFP-3D<sup>TM</sup> AFM, and a typical example of the recorded three-dimensional images of the prepared bitumen surface in an electrolyte is shown Figure 3-5. On average, the roughness of the bitumen surface over a 20  $\mu\text{m}$   $\times$  20  $\mu\text{m}$  area, defined by the root-mean-square (RMS) of the roughness parameter, was found to be less than 1 nm (a few protrusions were up to 2 nm in height). This result was consistent with similar observations by Liu et al. [2003] and Drelich et al. [2007], who captured the images of the prepared bitumen sample in air. As the roughness of the bitumen-water interface is no more than 1 nm, it can effectively be treated as a smooth surface in regard to AFM measurements (recall the radius of curvature of a fine cantilever tip is of order 10 nm).

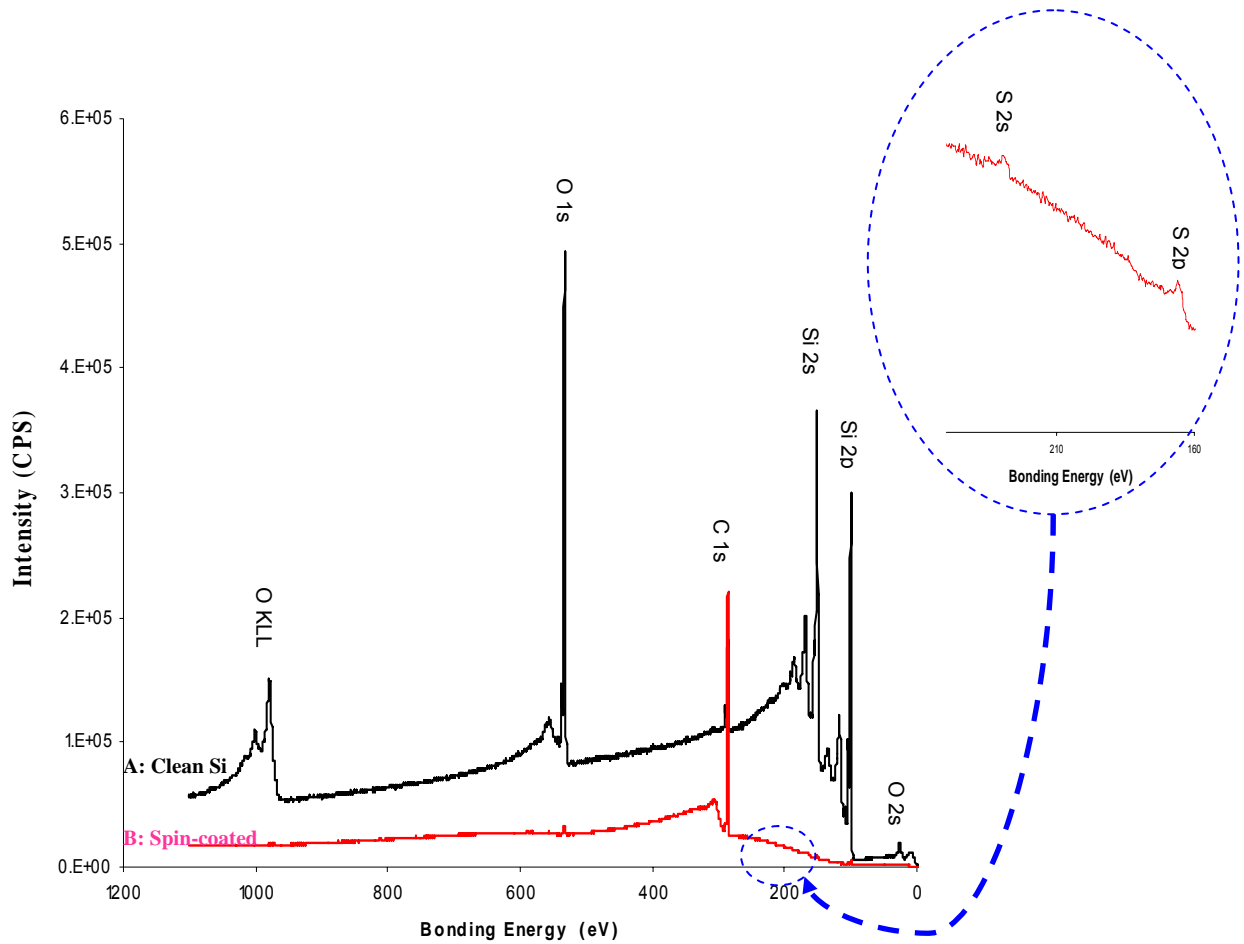


**Figure 3-4: XPS spectra of (A): the clean silicon substrate (black line) and (B): the bitumen-coated silicon substrate (red line). A blow-up view of sulfur-element peaks is also included.**

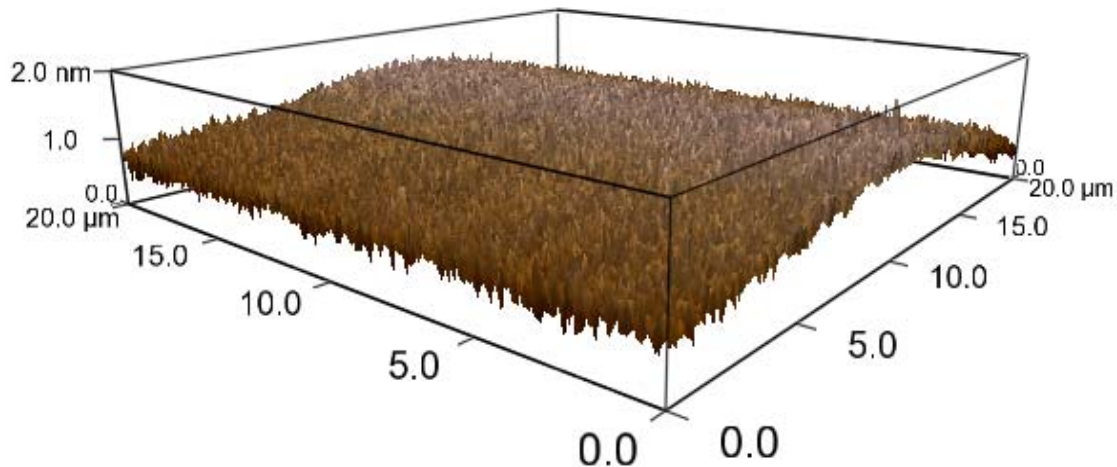


**Figure 3-5: A typical three-dimensional image of the  $20\mu\text{m} \times 20\mu\text{m}$  area of bitumen substrate in a SPW electrolyte obtained with tapping mode.** Image with  $256 \times 256$  resolutions was captured with using a Veeco SNP-10 cantilever at a scan rate of 1 Hz. The manufacturer-given data of the cantilever shows a spring constant of 0.58 N/m, a tip with radius of curvature of about 10 nm, and a resonance frequency in air of about 60 kHz. The resonance frequency of the cantilever in an electrolyte was about 30-50 % of the value in air. The cantilever was cleaned by UV irradiation for at least 2 hours and the bitumen substrate was immersed in the electrolyte for at least 30 min prior to imaging.

### 3.3.3 Force mapping measurements

Colloidal forces between an AFM cantilever tip and the bitumen substrate were measured using the contact mode of MFP-3D™ AFM (Asylum Research Technology Ltd) with a home-made fluid cell. The SNP-10 series cantilever with four pyramid-shaped tips (approximately 10 nm radius of curvature), made of silicon nitride ( $\text{Si}_3\text{N}_4$ ) and purchased from the Veeco Probes, CA, was used. Cantilever tips with a manufacturer's nominal spring constant of 0.58 N/m and 0.12 N/m were chosen for the force measurements, depending on the pH of the electrolyte. It was important to note that, due to manufacturing difficulty in obtaining unique value for mass production, the spring constant for the similar cantilever tips provided by the manufacturer might have one-order-of-magnitude variations and result in largely misleading force data. For better accuracy, the spring constant of the individual cantilever tip was re-determined in air with a thermal noise calibration method as described in the manual of the AFM, giving an error of less than 10%. Prior to each experiment, the fluid cell was rinsed thoroughly with toluene, de-ionized water and ethanol, and finally blow-dried with pure nitrogen; the cantilever was rinsed with de-ionized water and then exposed to ultraviolet irradiation for at least two hours to remove any possible contaminants. Colloidal force measurements between the AFM tip and the bitumen were conducted in the SPW electrolyte with varying pH values (pH = 6, 8 and 10;  $[\text{Ca}^{2+}] = 0$ ) within a period of 30 min to 2 hr after the tip and bitumen substrate were immersed in the test electrolyte. All experiments were conducted at room temperatures (23 °C).

In the force mapping measurements, the AFM tip was made to shift stepwise at 40 nm per step in one lateral direction (x or y axis) over a 2- $\mu\text{m}$  distance on the bitumen surface; this

was done using an operator-controlled offset piezo-scanner adjustment in the software. For each offset *local position*, one set of local approaching and retracting photodiode current – piezo displacement ( $I_{\text{PSD}} - Z_p$ ) raw profiles were measured and recorded. The long ranged force curve was obtained with the manual conversion method using excel spreadsheet, which converted the tip-substrate approaching  $I_{\text{PSD}} - Z_p$  curve into the force – distance curve; this conversion procedure was outlined earlier in Section 3.3.1.

### **3.4 Electrophoresis technique**

As was mentioned in Section 2.3.2, in order to predict the theoretical probabilities of coalescence between two bitumen droplets, we must know the *surface averaged*  $\zeta$ -potentials of suspended bitumen droplets in different aqueous media. In addition, as discussed in Section 3.3.1, in order to fit the DLVO theory to the force-distance curves, the  $\zeta$ -potentials of AFM tip needs to be estimated with those of sub-micron silicon nitride particles in the similar solutions. For determining  $\zeta$ -potentials, by far the most common technique is the electrophoresis as described in the following.

#### **3.4.1 Introduction of electrophoresis**

Electrophoresis is a technique which determines  $\zeta$ -potentials by tracking the motion of particles and measuring their electrophoretic velocity in an applied electrical field. Among many potential instruments based on the principle of electrophoresis, the instrument used in this study was the so-called *Zeta Phase Analysis Light Scattering* (ZetaPALS) analyzer (Brookhaven Instruments Corporation, USA). This Zeta-analyzer consists of a sample cell

holder, a pair of electrodes fitted into perfectly symmetrical compartments, a laser-illuminator, a digital signal detector and other accessories, as illustrated in Figure 3-6.

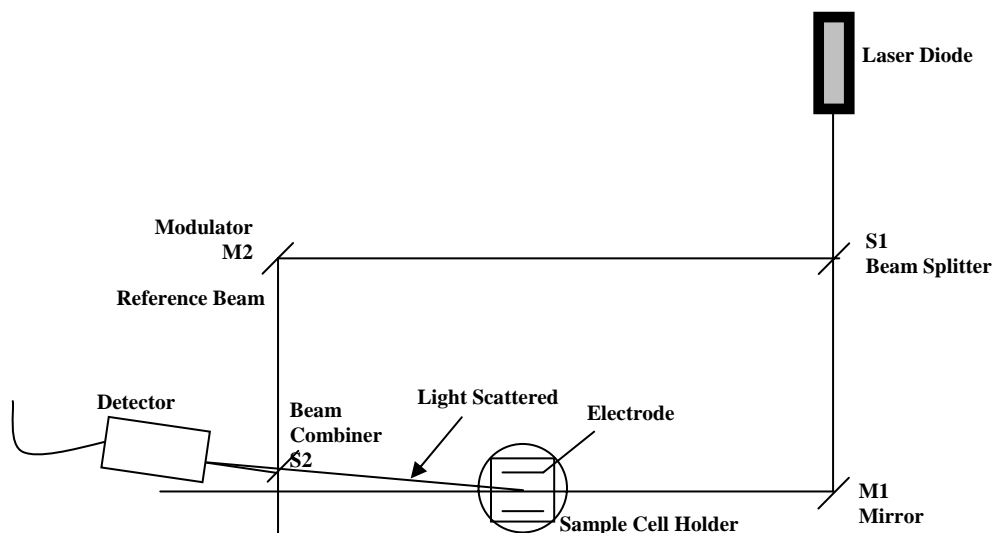


**Figure 3-6: Schematic of ZetaPALS analyzer.** [Adapted from Instruction Manual]

In this system, a colloid sample is placed in the cell holder which carries two electrodes. When a voltage is provided between electrodes, a uniform electric field is produced within the sample solution and therefore the charged particles move towards the oppositely-charged electrode. The direction of the particle movement indicates the sign of the colloid charge. The velocity of the particles is directly proportional to the magnitude of the charge or  $\zeta$ -potential. The movement of particles is traced with the illuminating laser light and then the frequency of light scattered by the particles into the detector is Doppler shifted by an amount proportional to the velocity of the particles. Keeping in mind that this Doppler shift is very small ( $\sim 100$  Hz) compared with the incident frequency ( $\sim 10^{14}$  Hz), this problem can be solved by heterodyning (i.e. recombining) the two split-off beams that consist of the scattered

beam and the reference beam modulated at 250 Hz, and then detecting the Doppler shift from the modulated value. In using phase quadrature, any small Doppler shift eventually gives rise to a change in phase between the signals. This phase change is then analyzed by a built-in phase analysis software, and the electrophoretic velocity of the particles can be obtained. In the final step, the  $\zeta$ -potential of the particles can be calculated with the above measured velocity ( $U$ ) in a known electric field strength ( $E$ ) using the following relations according to different conditions:

Smoluchowski equation: 
$$\zeta = \frac{U\eta}{\varepsilon E} \quad (3.3)$$

for large particles ( $\kappa \cdot d \gg 1$ ); or

Hückel's equation: 
$$\zeta = \frac{3U\eta}{2\varepsilon E} \quad (3.4)$$

for small particles ( $\kappa \cdot d \ll 1$ ), where,  $\eta$  is the continuous phase viscosity, and  $\varepsilon$  is the permittivity of the sample solution.

### 3.4.2 Suspension preparation

The two types of aqueous suspensions with suspended bitumen and silicone nitride were prepared for  $\zeta$ -potential measurements by similar procedures: making a concentrated stock suspension in an ultrasonic method and diluting it by re-suspending a few drops of fresh concentrate ( $\sim 1$  mL) in the mother electrolyte ( $\sim 20$  mL). In the case of bitumen particles, the stock suspension was prepared by pouring 20 mL of an SPW solution into a vial containing approximately 0.1 g of solids-free bitumen on the bottom, sonicating the vial in a warm water bath for about 20 min using a 310 trans-sonic dismembrator (Elma, Germany), and allowing it to stand for about 1 hr at room temperature before the upper portion of suspension was

taken for diluting. The silicone nitride suspension was prepared by mixing 50 mg of silicone nitride nano-powers (aggregates of the initial 50 nm in diameter) with 20 mL of electrolyte. The mixture was conditioned in the ultrasonic bath for 10 min and then left for about 30 min before diluting. As such, in either case, the particle concentration of the after-diluted suspension is about 0.01-0.05 wt%; this was optimum value for measurement. On the other hand, the resulting suspended particle size was approximately in the range of a few microns; this satisfied the prerequisite that colloidal stability does not essentially change during the entire measurement duration.

### **3.4.3 Zeta potentials measurement**

After preparing dilute sample suspension, approximately 1.5 mL was transferred into the clean disposable sample cell. Great care was taken to fully insert the electrodes and to avoid trapped air bubbles. After inserting the cell all the way into the cell holder, operating parameters were chosen within acceptable limits and the instrument was ready to measure  $\zeta$ -potentials. For each experimental condition, a minimum of 50 reproducible measurements were implemented and the average value of  $\zeta$  with standard deviation was reported on the basis of these measurements. All experiments were carried out at room temperature ( $\sim 22 \pm 1^\circ\text{C}$ ) and the  $\zeta$  potentials at each condition were calculated on the basis of Smoluchowski relation (eqn. 3.3). In this study, before each experiment, the performance of ZetaPALS analyzer was confirmed using the diluted BI-ZR3 ( $\sim 20$  mg/L) reference suspension with 1 mM sodium chloride, whose average  $\zeta$  potential is within the range from -49 mV to -57 mV. Once reasonable and reproducible results were given, the measurement of unknown samples would be carried out.

## Chapter 4 : Results and discussion

### 4.1 Determining average $\zeta$ potentials of suspended particles in electrolytes with ZetaPALS

#### 4.1.1 Bitumen-in-water suspensions

Calcium ion concentration and pH are two of the most common chemical parameters present in the process water during bitumen extraction from the oil sands. It is expected that  $\text{Ca}^{2+}$  and pH determining ions not only “compress” the electrostatic double layer, but also change the interfacial properties of bitumen, as demonstrated by the Debye length ( $\kappa^{-1}$ ) and zeta potentials ( $\zeta_{ave}$ ). In the current study, the doping of the two types of ions was relatively small and had insignificant effects on the ionic strength and the therefore the Debye length ( $\kappa^{-1}$ ) of the final aqueous electrolytes. The average  $\zeta$ -potentials of suspended bitumen in simulated process water (SPW) were measured while varying  $[\text{Ca}^{2+}]$  and pH. The measurements were made by electrophoresis as described in Section 3.4, and their results at different  $\text{Ca}^{2+}$  ion concentrations ( $[\text{Ca}^{2+}] = 0, 0.1, \text{ and } 0.5 \text{ mM}$ ) and pH values (pH = 6, 8, and 10) are shown in Figure 4-1. From the data in the figure, it is evident that the bitumen droplets were negatively charged under all the experimental conditions. In addition, the two chemical parameters had significant but opposite influence on the magnitude of the measured average zeta potential. For a given  $[\text{Ca}^{2+}]$ , with increasing pH values, the magnitude of the bitumen droplet  $\zeta$ -potential was dramatically increased. As an example, in the case of  $[\text{Ca}^{2+}] = 0$ , as the pH of the electrolyte increased from 6 to 10, the  $\zeta$  –potential of bitumen droplets became more negative: from  $-65 \text{ mV}$  to  $-110 \text{ mV}$ . However, for a given pH value, with the

small raising concentration of  $\text{Ca}^{2+}$  ion, the magnitude of bitumen  $\zeta$ -potentials was effectively decreased. For instance, at the condition  $\text{pH} = 8$ , the  $\zeta$  potentials of bitumen were less negative: from  $-93$  mV to  $-61$  mV. The trend of the above result is in good agreement with the data of Liu et al. [2003], who investigated the effects of the parameters  $[\text{Ca}^{2+}]$  and  $\text{pH}$  on bitumen  $\zeta$ -potentials in 1 mM KCl background electrolytes. This result can be ascribed to the fact that the carboxyl groups (RCOOH) belonging to the surfactants are naturally present on the bitumen-water interface [Takamura & Chow 1985]. Under the influence of  $\text{pH}$  determining ions ( $\text{H}^+$  or  $\text{OH}^-$ ), the carboxyl groups (RCOOH) are in dissociation and association equilibrium with carboxylic anions ( $\text{RCOO}^-$ ), as demonstrated in eqn (4.1). The  $\text{OH}^-$  ion promotes the reaction in eqn (4.1) to proceed to the right-hand side, while the  $\text{H}^+$  ion has the opposite effect. It is therefore expected that bitumen surface would be more negatively charged with increasing  $\text{pH}$ .



Likewise, in the presence of calcium ion ( $\text{Ca}^{2+}$ ), the specific chemical-reaction between the carboxylic anions ( $\text{RCOO}^-$ ) and the calcium cation ( $\text{Ca}^{2+}$ ) is postulated to take place [Takamura & Chow 1985], as shown in eqn (4.2). Here, we would expect the  $\zeta$ -potential of bitumen to be less negative with the increase of  $\text{Ca}^{2+}$  ion concentration.



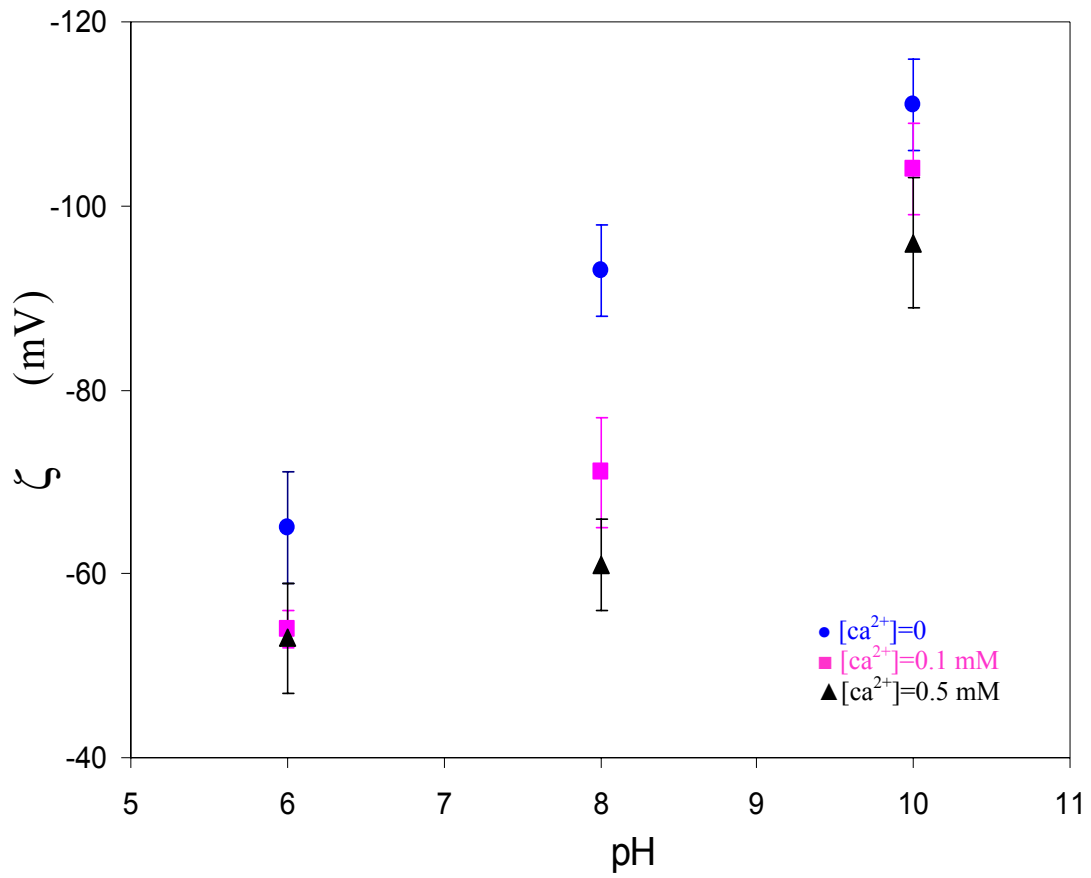


**Figure 4-1:  $\zeta$ -potentials of suspended bitumen droplets in the SPW-based aqueous solutions at different pH and  $[Ca^{2+}]$ .** The potentials were measured using electrophoresis. The experiments were conducted at room temperature. The average size of bitumen droplet was estimated to be of order 1  $\mu\text{m}$ .

#### 4.1.2 Si<sub>3</sub>N<sub>4</sub>-in-water suspensions

Since the surface potential (or surface charge density) of the Si<sub>3</sub>N<sub>4</sub> AFM tip is the important parameter for fitting the AFM force curve, we had to determine its value prior to analysis of the force data. In this regard, submicron silicon nitride particles as received were suspended in the SPW-based aqueous electrolytes similar to those used in the AFM experiment. The surface potential of suspended Si<sub>3</sub>N<sub>4</sub> particles was assumed to be the relevant  $\zeta$ -potentials, which was measured by electrophoresis; their average values with standard deviation bars at different pH values (pH = 6, 8 and 10) are shown in Figure 4-3. The data clearly shows that the surface potentials of Si<sub>3</sub>N<sub>4</sub> particles were negatively charged in the background SPW solutions having pH  $\geq$  6. In the meantime, as the pH increased from 6, 8 to 10, the Si<sub>3</sub>N<sub>4</sub> surface potentials were found to be more negative: from -36 mV, -53 mV to -65 mV.

For the feasibility demonstration of equating the Si<sub>3</sub>N<sub>4</sub> particle without treatment to the Si<sub>3</sub>N<sub>4</sub> AFM tip, we also applied the same electrophoresis method to measure the surface potentials of Si<sub>3</sub>N<sub>4</sub> in 1mM KCl solution of varying pH (pH = 4, 6, and 8), and the results (square points with error bars in Figure 4-2) are then compared with similar values (solid line in Figure 4-2) reported in the work of Yin & Drelich [2008]. The authors obtained surface potentials (or charge densities) by curve fitting to the AFM-measured colloidal forces between the Si<sub>3</sub>N<sub>4</sub> tip and the Si<sub>3</sub>N<sub>4</sub> cantilever in 1mM KCl background electrolytes of varying pH values (from 4 to 9), assuming identical charge value between the Si<sub>3</sub>N<sub>4</sub> tip and the cantilever. The data from two methods, as depicted in Figure 4-2, are seen to be in reasonable agreement. This comparison of results strongly supports our assumption of equivalence between Si<sub>3</sub>N<sub>4</sub> particles and the Si<sub>3</sub>N<sub>4</sub> AFM tip.

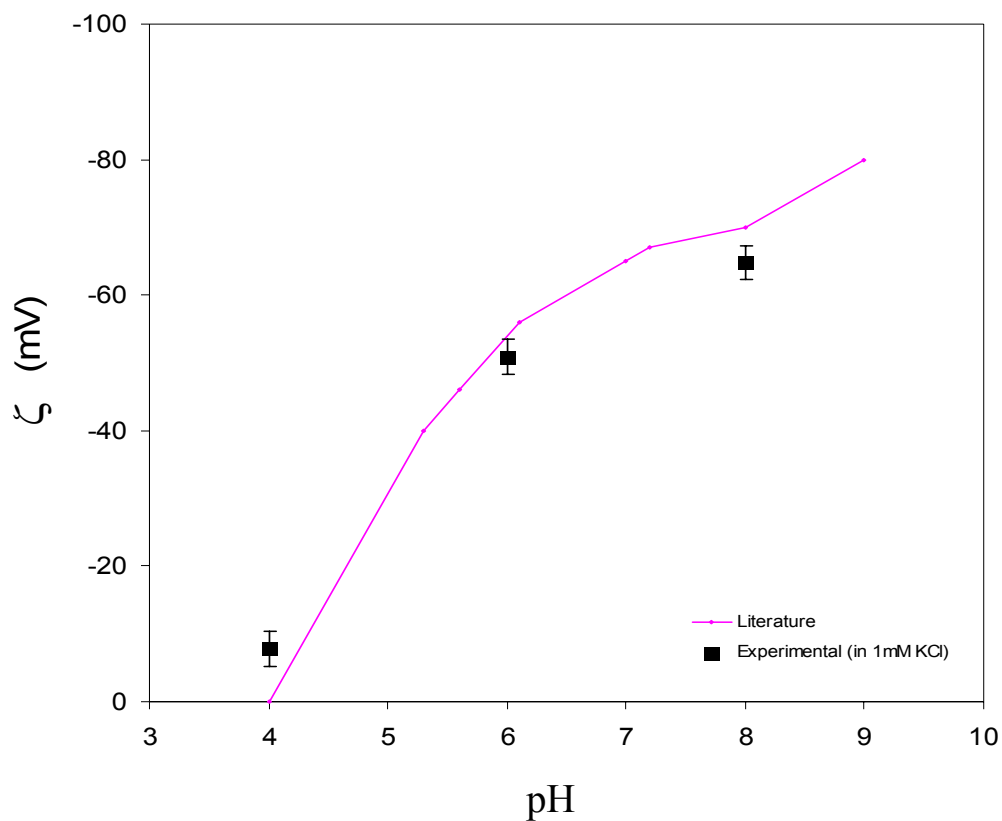


**Figure 4-2: Comparison of surface potentials of  $\text{Si}_3\text{N}_4$  in 1mM KCl solution of varying pH in this study with similar value reported in literature [Yin & Drelich 2008].** We measured the electrophoretic mobility of powdered  $\text{Si}_3\text{N}_4$  as received and calculated the surface potentials (shown in the square symbols with error bars) assuming the zeta potentials as surface potentials. Yin & Drelich measured the  $\text{Si}_3\text{N}_4$  -  $\text{Si}_3\text{N}_4$  colloidal forces using AFM and curve fitted them to obtain surface charge densities and zeta potentials, which are shown in the solid line with small dots.

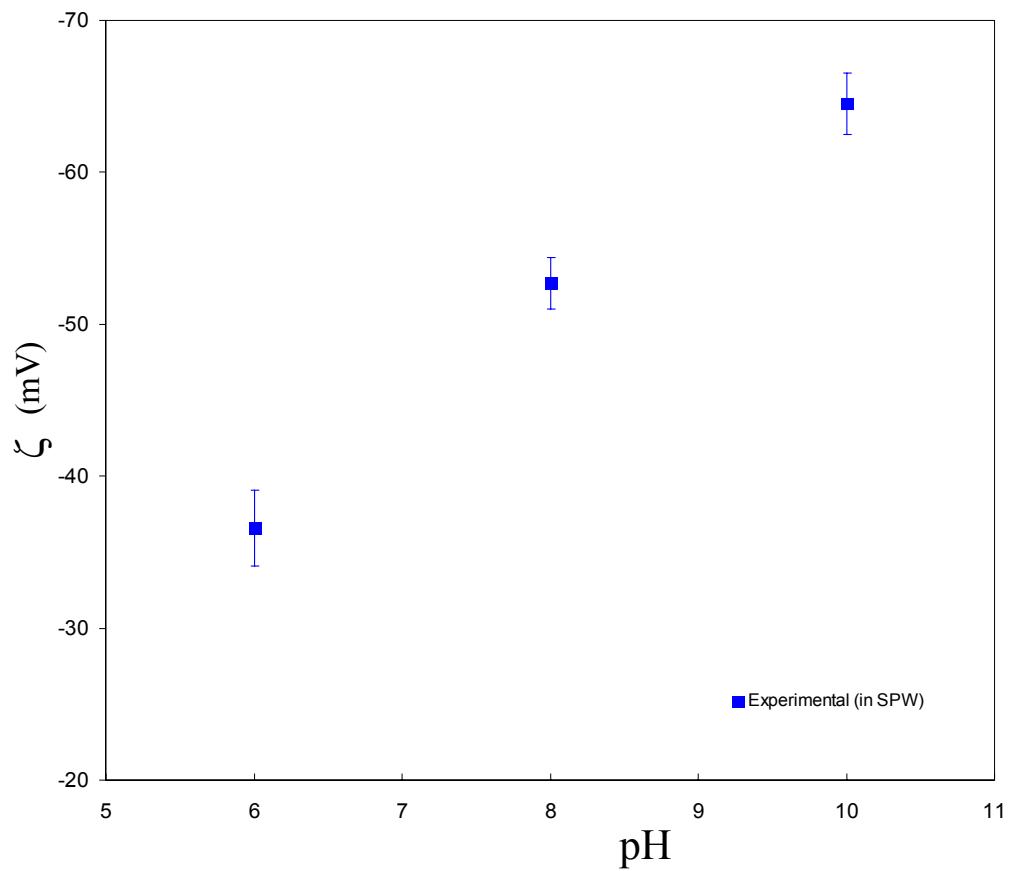


**Figure 4-3: Surface potentials of  $\text{Si}_3\text{N}_4$  powders in SPW-based aqueous electrolytes of varying pH in absence of calcium ion, assuming equality between  $\zeta$  potentials and surface potentials. The potentials were measured using electrophoretic experiments. The experiments were conducted at room temperature. The average bitumen droplet size was estimated to be of about  $1 \mu\text{m}$ .**

## 4.2 Quantifying shear-induced coalescence of bitumen droplets in water with micropipette

### 4.2.1 General observations

Typical oblique contact experiments using the micropipette technique are illustrated by the series of photographs in Figure 4-4; this was designed to study the coalescence phenomena of bitumen drops suspended in aqueous media under various conditions. The two droplets (small one had diameter of approximately 250  $\mu\text{m}$ ) were brought into “contact” in either moving direction and then the small drop was made to glide along the surface of the stationary and much larger drop over a certain distance at a preset speed; the suspending media were SPW electrolytes with three concentrations of  $\text{Ca}^{2+}$  ions ( $[\text{Ca}^{2+}] = 0, 0.1, \text{ and } 0.5$  mM) and three different pH values (pH = 6, 8, and 10). One deformation ratio ( $DR = 1.1$ ), four distances of shear contact ( $H = 0, 50, 100, \text{ and } 200$   $\mu\text{m}$ ), and three speeds of shear contact ( $v = 1.5, 15, \text{ and } 150$   $\mu\text{m/s}$ ) were chosen in this study. To avoid the effect of “aging” of the interface [Moran et al. 2007b], all experiments were conducted within 1 hr of dispersion preparation. Under the above conditions, the three coalescence phenomena in the following were generally observed:

- i. Coalescence *did* occur in all cases. However, the process was stochastic in that, under *identical* experimental conditions, a contact event may or may not result in coalescence. Such a stochastic process can only be represented by an experimentally-determined probability of coalescence  $\Phi(\text{exp})$ , as described in Section 3.2.3.<sup>†</sup> In cases where coalescence did not occur (photos on the right column of Figure 4-4), the two droplets

---

<sup>†</sup> In the limiting cases when  $\Phi(\text{exp})$  is either 0 or 1, the stochastic process reduces to apparent determinism.

were easily separated as either one of the suction pipettes was retracted. In addition, there was no evidence of bitumen-bitumen cohesion as two “un-coalesced” droplets were separated. Otherwise, as shown in the left column of Figure 4-4, as the pipette was pulled back, it was clearly evident that the two droplets had coalesced at the contact region. Given sufficient time, the coalesced droplets would eventually become one spherical drop. The measurement of this relaxation time, which depends on the drop size and interfacial properties [Yeung et al. 1999], was beyond the scope of the present study. This stochastic nature of coalescence was also documented in the previous head-on contact experiments where two similarly sized bitumen drops were tested [Esmaili et al. 2012].

- ii. The probability of coalescence was strongly dependent on the contacted area between the two droplets. Droplets with larger contacted area (due to longer distance of oblique contact) were more likely to coalesce than those with less contacted area. This observed behavior was a reinforcement of the previous study [Esmaili et al. 2012] — that bigger drops were easier to coalesce than smaller ones. (This was obvious, as bigger drops would undoubtedly have larger contacted area. However, classical DLVO theory could not explain the fact that bigger drops were easier to coalesce.)
- iii. If coalescence did occur, it would take place on the first sliding/shear contact (either upward or downward), as illustrated in the left column of Figure 4-4. Otherwise, coalescence would not happen even after many cycles (upwards and downwards) of shear contact in the same contact region (photos on right). If one wanted coalescence to occur for the same two drops, new contact regions must be explored.

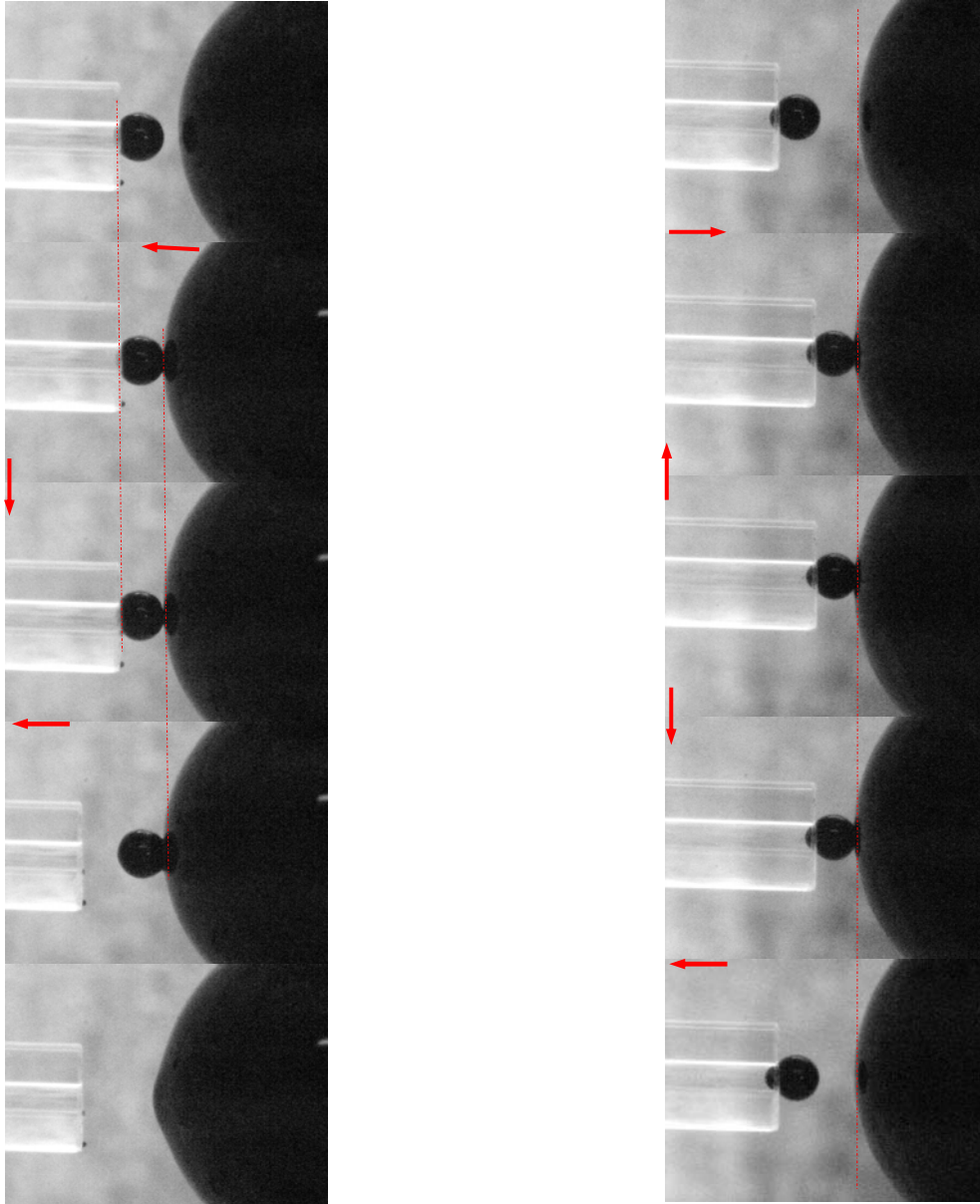


**Figure 4-4: Series of Photos showing oblique contact experiments between bitumen drops.** The experimental conditions in the left and right columns were *identical*: the medium was SPW in absence of  $\text{Ca}^{2+}$ ; temperature of medium was  $22^\circ\text{C}$ ; distance and speed of shear contact were controlled at  $100\ \mu\text{m}$  and  $150\ \mu\text{m/s}$ , respectively; the sizes of small and large drops were around  $250\ \mu\text{m}$  and  $2.5\ \text{mm}$ ; the deformation ratio of small drop was 1.1. Nevertheless, the outcomes of the two contact events were different: coalescence occurred on the left, but not on the right (despite sweeping the small droplet multiple times over the big drop).

#### 4.2.2 Constant shear distance

Shear-induced contact is often encountered in the industrial process of bitumen extraction — in a variety of situations where mechanical agitation is involved. In this study, the role of shear on bitumen droplet coalescence was divided into two parts: in term of the effects of shear distance ( $H$ ) and shear speed ( $\nu$ ). In this section, we fix the distances of shear contact at 100 and 200  $\mu\text{m}$ , and maintain the same water chemistry (SPW with  $[\text{Ca}^{2+}] = 0$  and  $\text{pH} = 8$ ). The focus here is on the effect of shear speed on the probability of coalescence between bitumen drops; the results are shown in Figure 4-5. Interestingly, regardless of the shear distance, as the speed of shear contact increased from low ( $\nu = 1.5 \mu\text{m/s}$  in this case) to medium ( $\nu = 15 \mu\text{m/s}$ ), the coalescence probability was not obviously seen to be affected. However, as the speed continued to increase to a relatively high value ( $\nu = 150 \mu\text{m/s}$ ), the probability appeared to be slightly decreased. Moreover, the decrease in  $\Phi(\text{exp})$  with  $\nu$  appears to be more prominent for the case with longer shearing distance. (As the speed varied from low to high, in the case of 200- $\mu\text{m}$  shear distance, the probability was reduced from 52% to 40%; however, only a 4% reduction in probability was observed for the case with 100- $\mu\text{m}$  shearing distance.)

We make the following speculation: Like the DLVO theory, our model of surface charge heterogeneity (or “SCH”; see Section 2.3.2) is an equilibrium one and involves no dynamics. As will be demonstrated in later sections, the patchy surface theory is capable of capturing the most important aspects of droplet coalescence. The above-mentioned dependence on shear speed is clearly a dynamic effect, but one that appears to be secondary (i.e. a higher order perturbation). This dynamic effect is very likely due to a lubricating aqueous film

between the droplets, which adds an extra stabilizing force (albeit a small one) to the EDL repulsion. The incorporation of lubrication theory into our SCH model shall be left for future work. Unlike shear speed, which makes only a small perturbation to  $\Phi(\text{exp})$ , the shear distance is a much more important parameter. This is demonstrated in the following section.

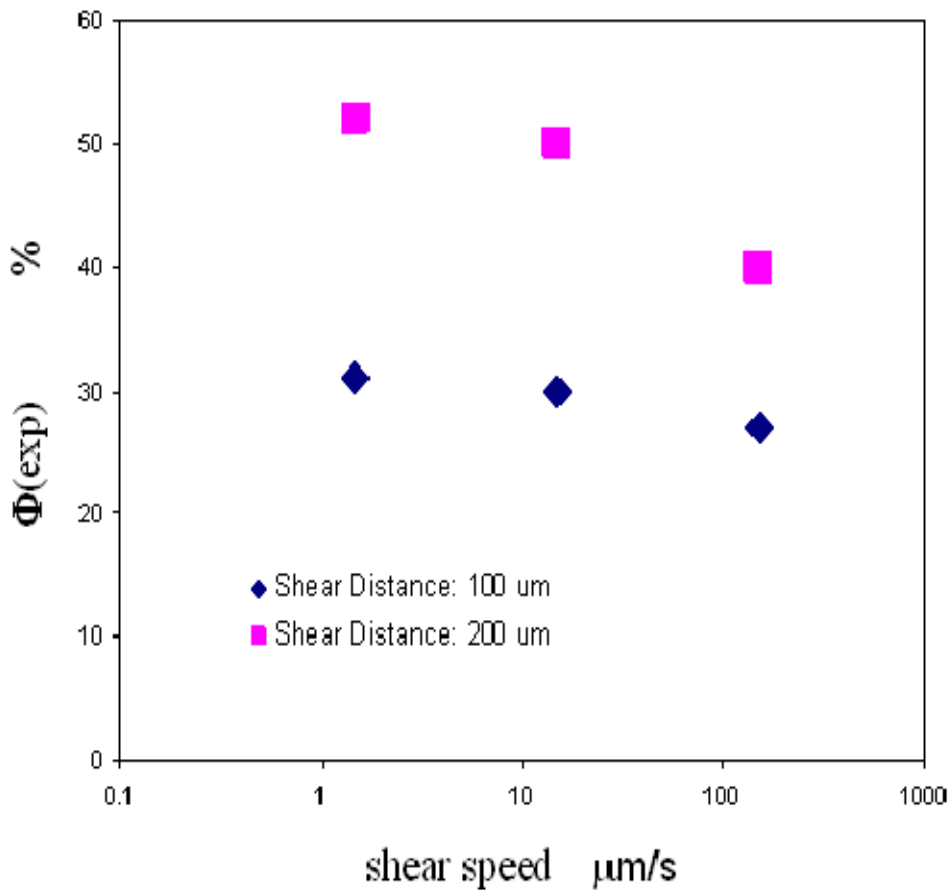


**Figure 4-5: Experimental probability of bitumen coalescence as function of shear speed.** The electrolyte medium was SPW in the absence of  $\text{Ca}^{2+}$  ions and at  $\text{pH} = 8$ . The temperature of medium was  $22^\circ\text{C}$ ; the size of the small droplet was around  $250 \mu\text{m}$ , and the larger drop was  $2.5 \text{ mm}$ . The deformation ratio of the small droplet was 1.1.

### 4.2.3 Constant shear speed

In this section, we turn to the other aspect of the oblique contact experiment. Here, we maintain the same shearing speed ( $\nu$ ) and vary the distances of shear contact ( $H$ ) from 0 to 200  $\mu\text{m}$  in 50  $\mu\text{m}$  intervals. The two parameters which characterize water chemistry, namely  $\text{Ca}^{2+}$  concentration and pH, are also varied. The influence of these parameters ( $H$ ,  $[\text{Ca}^{2+}]$  and pH) on the probability of coalescence ( $\Phi(\text{exp})$ ) are summarized in Figures 4-6 to 4-8. Here, we should point out that the speed of shear was kept very low during oblique contact ( $\nu = 1.5 \mu\text{m/s}$ ); we can thus neglect any dynamic effect and treated the experimental condition as quasi-static (see Figure 4-5). From the data points in the three figures, it is obvious that the shear distance  $H$  affected very strongly the probabilities of coalescence (at least until  $\Phi(\text{exp})$  reaches 100% and cannot increase any further). Such effects can be divided into three categories: First, the probabilities of bitumen coalescence were significantly improved (by several times) when oblique contact distances were changed from 0 to 200  $\mu\text{m}$ . This kind of trend was observed for the conditions of pH = 10 &  $[\text{Ca}^{2+}] = 0$ , pH = 10 &  $[\text{Ca}^{2+}] = 0.1 \text{ mM}$ , and pH = 8 &  $[\text{Ca}^{2+}] = 0$ . Second, the rate of increase of the coalescence probability was not as dramatic as that of the first category, and the probability was leveled off after 100% coalescence was reached at a certain shear distance. This phenomena was seen for the conditions such as pH = 10 &  $[\text{Ca}^{2+}] = 0.5 \text{ mM}$ , and pH = 8 &  $[\text{Ca}^{2+}] = 0.1 \text{ mM}$ . Third, no change of coalescence probability (all were 100 percentages) was observed in the cases of pH = 8 &  $[\text{Ca}^{2+}] = 0.5 \text{ mM}$ , and pH = 6 &  $[\text{Ca}^{2+}] = 0.5 \text{ mM}$ , as the shear distance increased. We speculated that, if the droplet size is decreased to a few microns, the apparent increasing trend of bitumen coalescence probability will likely be expected with increasing shear distance. The current experimental setup was not suitable for

examining the behavior of micron-sized drops. The influence of bitumen droplet size on coalescence was studied in a previous but related study [Esmaeili et al. 2012], which reported that bigger bitumen droplets tended to coalesce more easily and suggested the similar, i.e. contact-area-dependent coalescence behaviors as here.

Next, it is worth mentioning that the effects of either  $[Ca^{2+}]$  or pH variations (which cause changes in the  $\zeta$ -potential in both cases; see Figure 4-1) on  $\Phi(\text{exp})$  was equally well quantified in the oblique contact experiments in which the shear speed was kept constant; their results are also illustrated in Figure 4-6 to 4-8. Generally, the coalescence probabilities were seen to steeply increase with the increase of  $[Ca^{2+}]$  (similar to the lowering of  $\zeta$ -potential and electrostatic repulsion). As an example, it is clearly shown in Figure 4-7 at pH = 8 that, for the case of contacts at zero shear distance, the absence of  $Ca^{2+}$  seldom (with only 8%) resulted in coalescence. With addition of 0.1 mM  $Ca^{2+}$ , the bitumen coalescence probability was increased to 83% — an order of magnitude higher than the case with no  $Ca^{2+}$  ions; the maximum probability (100%) was reached when 0.5 mM  $Ca^{2+}$  was added. This behavior indicates that the presence of calcium ions promoted bitumen droplets to coalesce. In contrast, the probabilities of coalescence were shown to moderately decrease with the increase of pH (i.e. an increase in  $\zeta$  potential, and hence electrostatic repulsion). For instance, in the case of  $[Ca^{2+}] = 0.1 \text{ mM}$  &  $H = 0$ , by comparing the values of the three square symbols located on the  $y$  axis as shown in Figures 4-6 to 4-8, the bitumen coalescence probability was decreased from 95%, 83% to 2 % with the rising of pH from 6, 8 to 10.

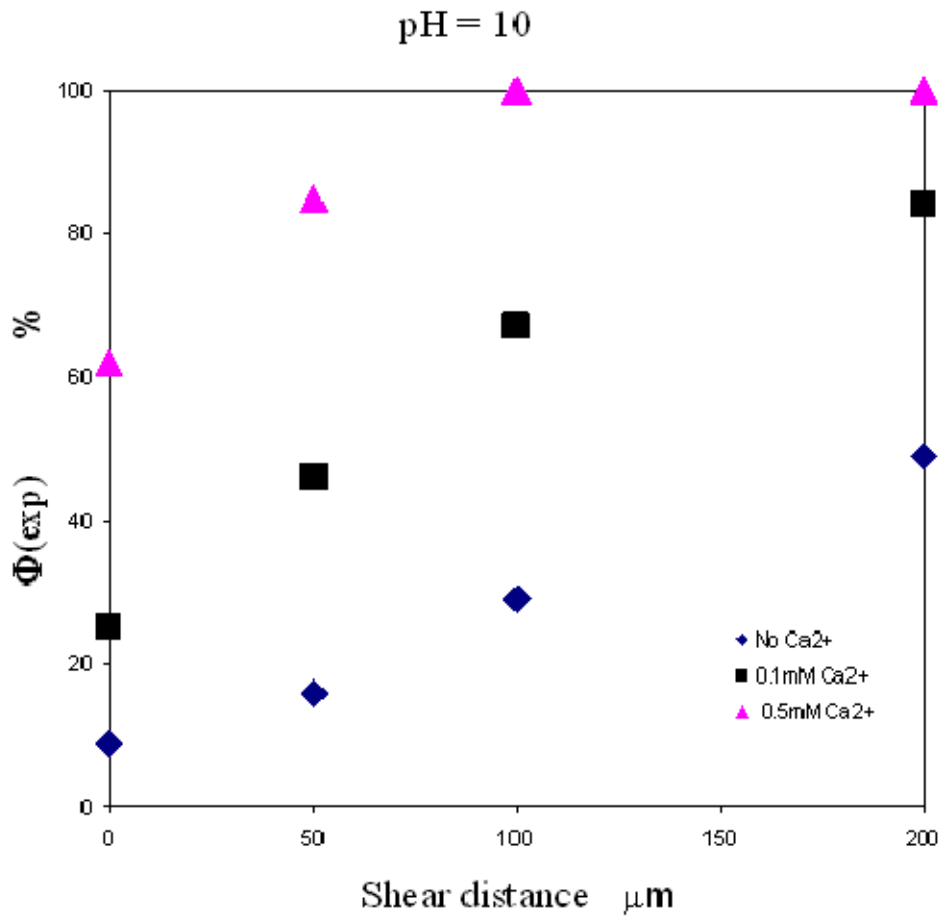


**Figure 4-6: Experimental probability of coalescence between bitumen droplets as function of shear distance.** The electrolyte media were SPW solutions at pH = 10 with varying  $[\text{Ca}^{2+}] = 0, 0.1, \text{ and } 0.5 \text{ mM}$ ; the speed of shear was held constant at  $1.5 \mu\text{m/s}$ ; the temperature of media was  $22^\circ\text{C}$ ; the size of small droplet was around  $250 \mu\text{m}$ , and the larger one  $2.5 \text{ mm}$ ; the deformation ratio of the small droplet was 1.1.

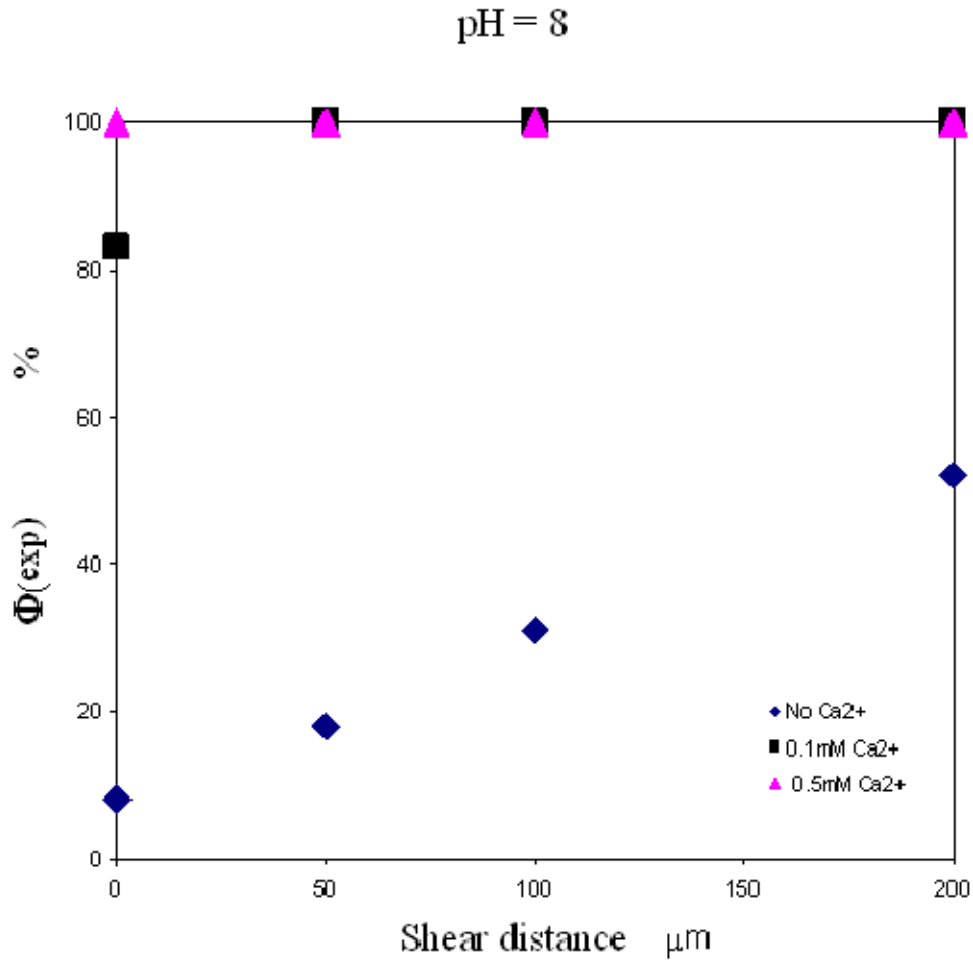


**Figure 4-7: Experimental probability of coalescence between bitumen droplets as function of shear distance.** The electrolyte media were SPW solutions at pH = 8 with varying  $[\text{Ca}^{2+}] = 0, 0.1, \text{ and } 0.5 \text{ mM}$ ; the speed of shear was held constant at  $1.5 \mu\text{m/s}$ ; the temperature of media was  $22^\circ\text{C}$ ; the size of small droplet was around  $250 \mu\text{m}$ , and the larger one  $2.5 \text{ mm}$ ; the deformation ratio of the small droplet was 1.1.

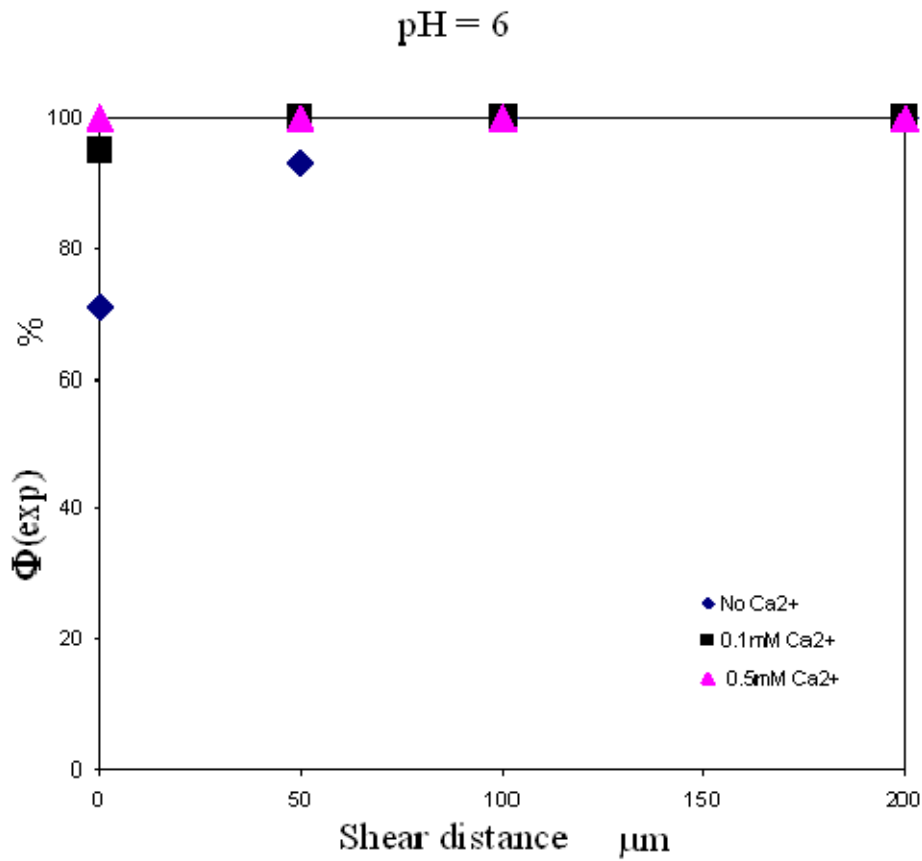


**Figure 4-8: Experimental probability of coalescence between bitumen droplets as function of shear distance.** The electrolyte media were SPW solutions at pH = 6 with varying  $[Ca^{2+}] = 0, 0.1, \text{ and } 0.5 \text{ mM}$ ; the speed of shear was held constant at  $1.5 \mu\text{m/s}$ ; the temperature of media was  $22^\circ\text{C}$ ; the size of small droplet was around  $250 \mu\text{m}$ , and the larger one  $2.5 \text{ mm}$ ; the deformation ratio of the small droplet was 1.1.

#### 4.2.4 Data fitting and interpretation

As just noted, the influence of droplet-droplet shearing on the coalescence of bitumen was considered under dynamic and quasi-equilibrium conditions; the results were presented in Section 4.2.2 and 4.2.3, respectively. Here, we will begin by elucidating the quasi-equilibrium experimental results. To do so, we must consider the balance of all the potential forces (or stresses) in the system. The order-of-magnitude approximation of colloidal and external forces was discussed in Section 2.3.1. In that analysis, the colloidal forces were founded on the classical DLVO theory, which consists of two rigorous and physically-sound components — electric double layer repulsion and van der Waals attraction. Firstly, we will evaluate the outcomes and predictions of this classical formalism. It is easily seen from the magnitude in Section 2.3.1 and Figure 2-5 that, even for the lowest magnitude of zeta potential ( $\sim 50$  mV, see Figure 4-1), the DLVO force barrier height was several orders of magnitude larger than any external forces for all the conditions studied. In the other argument, as quoted in Section 2.3.1, according to the classical DLVO theory, when equal and homogenous zeta potentials ( $\zeta_1 = \zeta_2$ ) interact across a thin water film, the two oil droplets would coalesce only if the zeta potentials (in magnitude) were less than about 8 mV. However, as depicted in Figure 4-1, the measured zeta potentials of bitumen in the SPW electrolytes exceeded 50 mV in magnitude. As such, classical DLVO theory would predict that coalescence between bitumen droplets, under all relevant experimental conditions, should *never* occur (i.e. it would suggest that  $\Phi(\text{theo})$  is identically zero). It should be noted that the classical DLVO theory is a deterministic one, and as such cannot explain the stochastic nature of the observed coalescence behaviors. Worse yet, the contact-area-dependence of  $\Phi(\text{theo})$  is completely at odds with the DLVO theory.

In this study, the complete failure of classical DLVO theory in making accurate predictions was attributed to the heterogeneous nature of the bitumen-water interface. As noted earlier, the classical theory makes ideal assumptions that the interacting surfaces are molecularly smooth and homogeneously charged, which may not apply to many practical systems. For liquid-liquid interfaces, as in the present case, the assumption of physical smoothness is likely valid [Walz 1998]. However, bitumen is an extremely viscous mixture of many different hydrocarbons and contains a complex molecular structure. The diffusion of surface charges at the bitumen-water interface would likely be limited or even effectively “immobile” on the time scale of the experiments, resulting in the existence of heterogeneous charge distribution. In what follows, we will attempt to make appropriate modifications of the DLVO theory by considering local variations in surface charge density on the electric double-layer interaction.

In order to determine the theoretical coalescence probability  $\Phi(\text{theo})$ , the surface charge heterogeneity (SCH) model was used; the description of this SCH model and the calculation procedures for the current oblique contact experiments were outlined in Section 2.3.2. In this model, four parameters were needed to determine  $\Phi(\text{theo})$ . Among them, the *surface averaged* potential  $\zeta_{\text{ave}}$  was obtained from electrophoretic measurements and the results were shown in Figure 4-1, and the contact area  $AC$  is estimated by formula (A.1) in Appendix A. This leaves the SCH model with two undetermined parameters: standard deviation of the random potential signal  $\sigma_{\zeta}$ , and the patch size  $L$ . As described in Section 4.2.3, the two chemical variables (pH and  $[\text{Ca}^{2+}]$ ) and one physical variable (shear distance

$H$ ) played very important roles in affecting the experimental coalescence probabilities  $\Phi(\text{exp})$ . It is obvious that the two heterogeneous parameters,  $\sigma_\zeta$  and  $L$ , are *inherently linked* to the chemical properties of the bitumen-water interface and should therefore be independent of the physical variable  $H$ . Yet, due to inadequate molecular understanding of the interface, we are not clear whether  $\sigma_\zeta$  and  $L$  should be independent of either or both of the variables pH and  $[\text{Ca}^{2+}]$ ; several scenarios exist.

#### First scenario

In the first scenario, we assume that the two fitting parameters  $\sigma_\zeta$  and  $L$  are independent of both pH and  $[\text{Ca}^{2+}]$ , and the consequence of data fitting by this assumption would be examined. Note that the surface-averaged potential  $\zeta_{\text{ave}}$  is linked to the variables pH and  $[\text{Ca}^{2+}]$  by Figure 4-1. Hence, we first rearrange the above three figures, from 4-6 to 4-8, into one graph in which the coalescence probability  $\Phi$  is plotted against the average potential  $\zeta_{\text{ave}}$ , as shown in Figure 4-9. Next, we use the measured  $\zeta_{\text{ave}}$  and  $\Phi(\text{exp})$  values in Figure 4-9 — a total 36 points in the present scenario, along with the corresponding oblique contact areas  $AC$ , for curve fitting to determine the parameters  $\sigma_\zeta$  and  $L$ . This is done through minimization of the least square function  $\Omega$  in eqn 2-39:

$$\Omega \equiv \sum_{i=1}^M [\Phi_i(\text{theo}) - \Phi_i(\text{exp})]^2 \quad (2.39)$$

The summation in eqn 2.39 is from 1 to  $M$ ;  $M$  is the number of experimental points to be fitted. By minimizing  $\Omega$  with respect to  $\sigma_\zeta$  and  $L$ , we obtained

$$\sigma_\zeta = 30 \text{ mV}; \quad L = 0.6 \text{ } \mu\text{m} \quad (4.3)$$

After obtaining the fitting parameters (values in eqn 4.3), the theoretical coalescence probability  $\Phi(\text{theo})$  were calculated (following the SCH theory described in Section 2.3.2); the results are shown as the solid lines in Figure 4-9. From this figure, it is clearly seen that the theoretical curves (e.g. the blue solid line) failed to match the experimental data (e.g. the blue diamond symbols), especially for the case of zero shear ( $H = 0$ ). This was likely due to the incorrect assumption that the two fitting parameters are independent of the two chemical variables pH and  $[\text{Ca}^{2+}]$ . So, we have to seek other options.

### Second scenario

In the second scenario, we make the assumption that the two fitting parameters are dependent on one variable, namely  $[\text{Ca}^{2+}]$ , but independent of the other variable, i.e. pH. We repeat the same fitting and minimization procedures. Here, it should be noted that the 36 data points must now be divided into 3 groups of 12 points — with each group corresponding to a particular value of  $[\text{Ca}^{2+}]$ . Minimization of the functional  $\Omega$  (eqn 2.39) will therefore be carried out three times, each time for a given value of  $[\text{Ca}^{2+}]$  and involving only 12 data points. After minimizing  $\Omega$  with respect to  $\sigma_c$  and  $L$ , we acquired the optimal values of two free parameters for different  $[\text{Ca}^{2+}]$  conditions; the results are shown in Table 4-1. With the use of these values, we calculated the theoretical probabilities, which are illustrated by the solid lines in Figures 4-10 to 4-12 for the three  $[\text{Ca}^{2+}]$  concentrations. A comparison between model predictions and experimental observation, especially in the case of  $[\text{Ca}^{2+}] = 0$  (Figure 4-10), indicates that the second scenario assumption has also failed (almost as miserably as in the first case). In what follows, we will explore the third scenario, with an assumption that is opposite to that of the second scenario.

**Table 4-1:** The two modeling parameters  $\sigma_\zeta$  and  $L$  obtained with best fitted to the corresponding experimental data by assuming their primary dependence on  $[\text{Ca}^{2+}]$ .

---

$[\text{Ca}^{2+}] / \text{mM}$	$\sigma_\zeta / \text{mV}$	$L / \mu\text{m}$
0	28	1
0.1	25	0.14
0.5	25	0.14

---

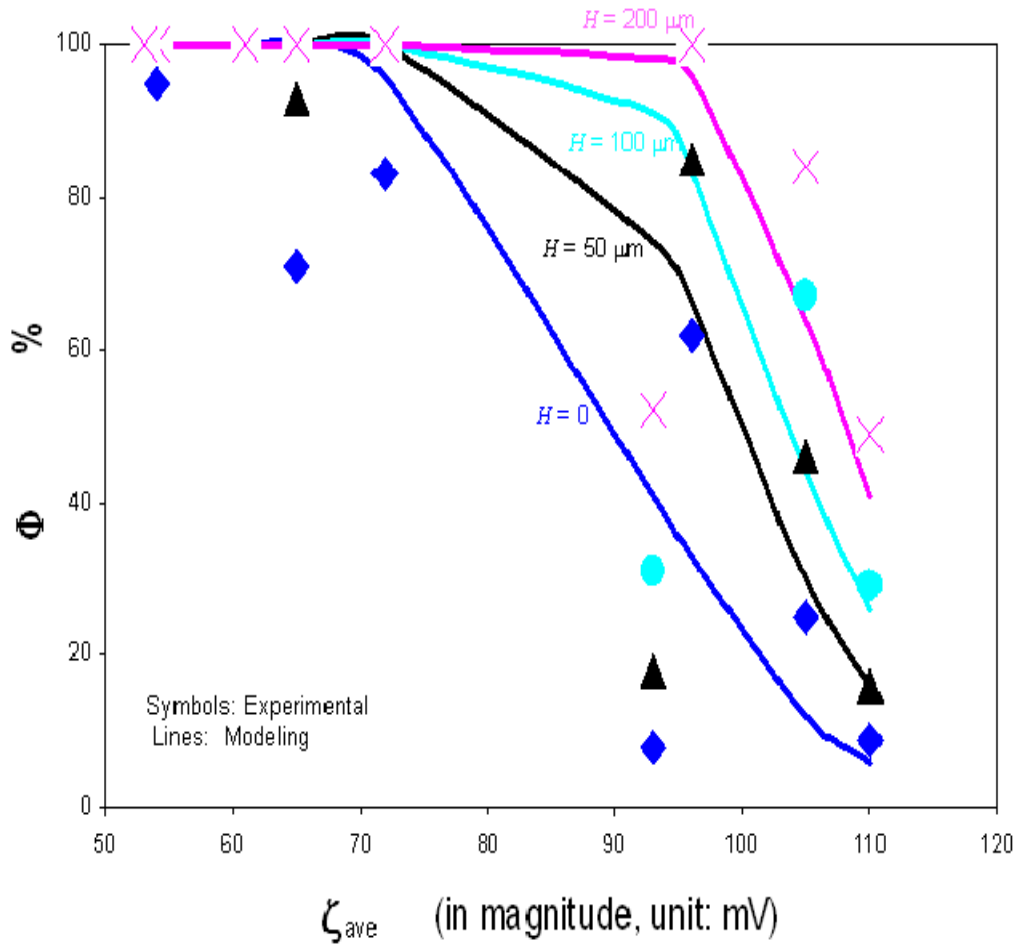


**Figure 4-9: Bitumen coalescence probability  $\Phi$  as function of surface-averaged zeta potential  $\zeta_{ave}$  (in magnitude) with varying shear distance  $H$ .** Here, the symbols are experimental results of coalescence probabilities (also see Figure 4-6 to 4-8); different symbols correspond to different shear distances  $\blacklozenge$ :  $H = 0$ ,  $\blacktriangle$ :  $H = 50 \mu\text{m}$ ,  $\bullet$ :  $H = 100 \mu\text{m}$ ,  $\times$ :  $H = 200 \mu\text{m}$ . The solid lines are theoretical model predictions based on the two fitting parameters:  $\sigma_{\zeta} = 30 \text{ mV}$  and  $L = 0.6 \mu\text{m}$ . The fitting was based on the assumption that these parameters are independent of both pH and  $[\text{Ca}^{2+}]$ . The magnitude of  $\zeta_{ave}$  were controlled by the two variables pH and  $[\text{Ca}^{2+}]$ , see Figure 4-1. The background electrolytes were SPW solutions with varying  $\text{Ca}^{2+}$  addition and pH; temperature of media was  $22^{\circ}\text{C}$ ; the speed of shear was controlled at  $1.5 \mu\text{m/s}$ ; the size of small drop was around  $250 \mu\text{m}$ , larger one  $2.5 \text{ mm}$ , the deformation ratio of small drop was 1.1.

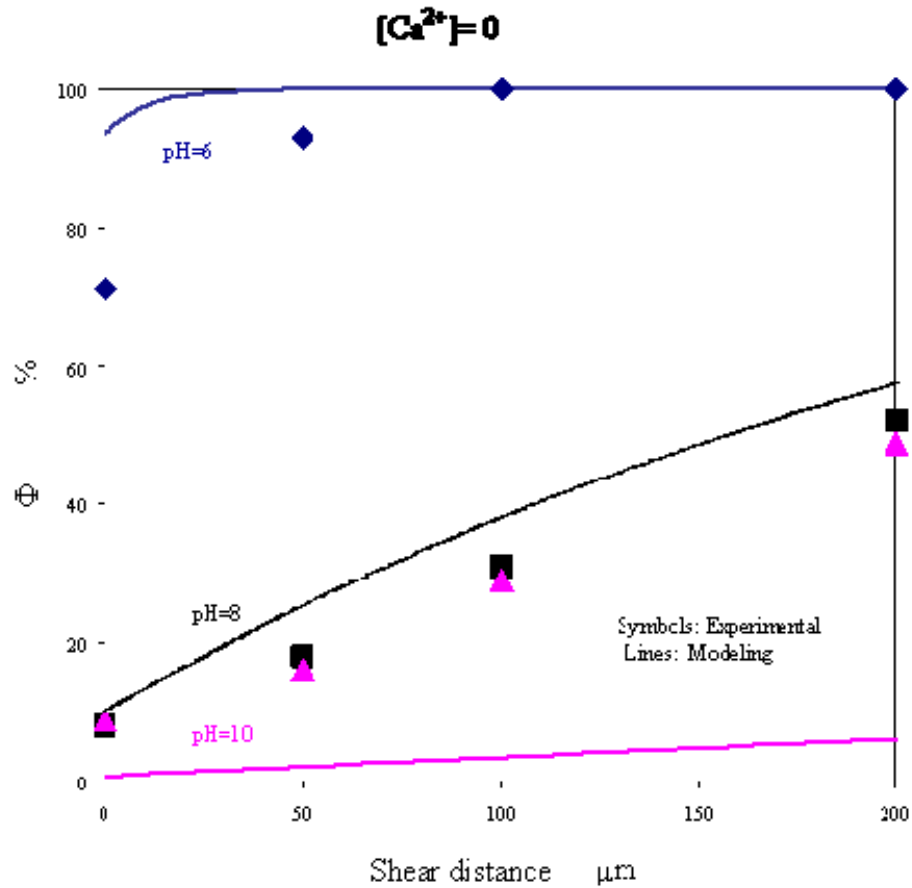


**Figure 4-10: Bitumen coalescence probability  $\Phi$  as function of shear distance  $H$  in the SPW background electrolytes with varying pH values at fixed  $[\text{Ca}^{2+}] = 0$ .** The symbols are experimental results of coalescence probabilities; different symbols correspond to different pH conditions ♦: pH = 6, ■: pH = 8, ▲: pH = 10. The solid lines are theoretical modeling predictions based on the two fitting parameters:  $\sigma_{\zeta} = 28$  mV;  $L = 1$   $\mu\text{m}$ ; the fitting was based on the assumption that these parameters were dependent on  $[\text{Ca}^{2+}]$  but independent on pH. The temperature of electrolyte media was 22°C; the speed of shear was controlled at 1.5  $\mu\text{m}/\text{s}$ ; the size of small droplet was around 250  $\mu\text{m}$ , larger one 2.5 mm, the deformation ratio of small droplet was 1.1.

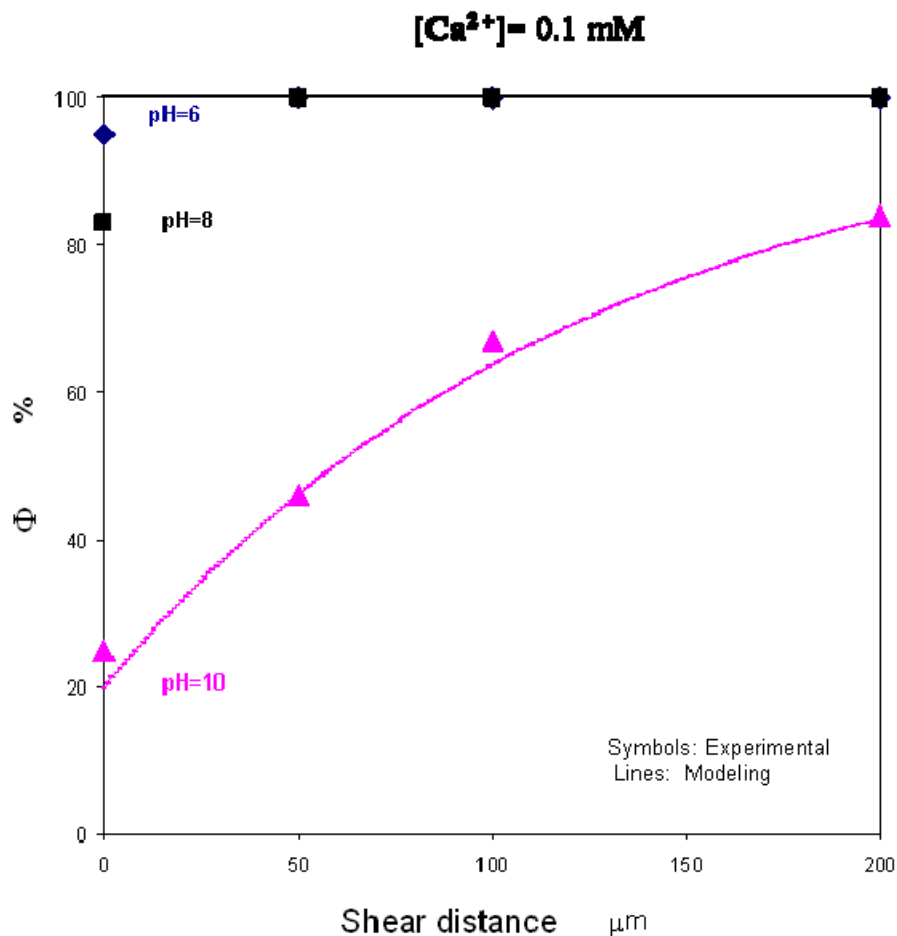


**Figure 4-11: Bitumen coalescence probability  $\Phi$  as function of shear distance  $H$  in the SPW background electrolytes with varying pH values at fixed  $[\text{Ca}^{2+}] = 0.1 \text{ mM}$ .** The symbols are experimental results of coalescence probabilities; different symbols correspond to different pH conditions  $\blacklozenge$ : pH = 6,  $\blacksquare$ : pH = 8,  $\blacktriangle$ : pH = 10. The solid lines are theoretical modeling predictions based on the two fitting parameters:  $\sigma_{\zeta} = 25 \text{ mV}$ ;  $L = 0.14 \mu\text{m}$ ; the fitting was based on the assumption that these parameters were dependent on  $[\text{Ca}^{2+}]$  but independent on pH. The temperature of electrolyte media was  $22^{\circ}\text{C}$ ; the speed of shear was controlled at  $1.5 \mu\text{m/s}$ ; the size of small droplet was around  $250 \mu\text{m}$ , larger one  $2.5 \text{ mm}$ , the deformation ratio of small droplet was 1.1.

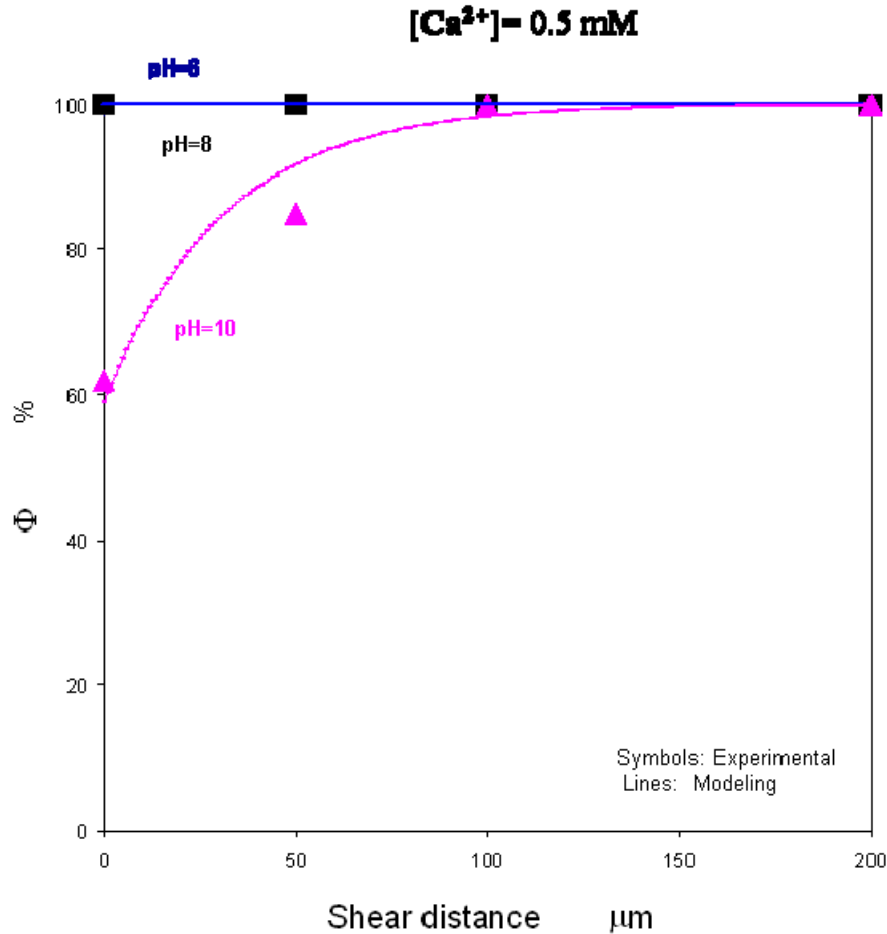


**Figure 4-12: Bitumen coalescence probability  $\Phi$  as function of shear distance  $H$  in the SPW background electrolytes with varying pH values at fixed  $[\text{Ca}^{2+}] = 0.5 \text{ mM}$ .** The symbols are experimental results of coalescence probabilities; different symbols correspond to different pH conditions  $\blacklozenge$ : pH = 6,  $\blacksquare$ : pH = 8,  $\blacktriangle$ : pH = 10. The solid lines are theoretical modeling predictions based on the two fitting parameters:  $\sigma_{\zeta} = 25 \text{ mV}$ ;  $L = 0.14 \text{ }\mu\text{m}$ ; the fitting was based on the assumption that these parameters were dependent on  $[\text{Ca}^{2+}]$  but independent on pH. The temperature of electrolyte media was  $22^{\circ}\text{C}$ ; the speed of shear was controlled at  $1.5 \text{ }\mu\text{m/s}$ ; the size of small droplet was around  $250 \text{ }\mu\text{m}$ , larger one  $2.5 \text{ mm}$ , the deformation ratio of small droplet was 1.1.

### Third scenario

In the third scenario, we assume that the two modeling parameters are primarily dependent on pH, but are insensitive to changes in  $[Ca^{2+}]$  (opposite of the second scenario assumption). Once again, we apply the proposed heterogeneity model to best fit the coalescence probabilities — this time under different pH conditions. The resulting optimum values of two modeling parameters (i.e.  $\sigma_{\zeta}$  and  $L$ , also called the heterogeneous parameters) are shown in Table 4-2 for three pH values. Using these values, the theoretical probabilities of coalescence predicted from the heterogeneity model were calculated, and the results are illustrated as the solid lines in Figures 4-13 to 4-15.

**Table 4-2: The effect of pH on the two modeling parameters  $\sigma_{\zeta}$  and  $L$ .** Those parameters were obtained with best fitted to the corresponding experimental data by assuming their primary dependence on pH.

pH	$\sigma_{\zeta}$ / mV	$L$ / $\mu\text{m}$
6	24	1
8	26	0.7
10	28	0.3

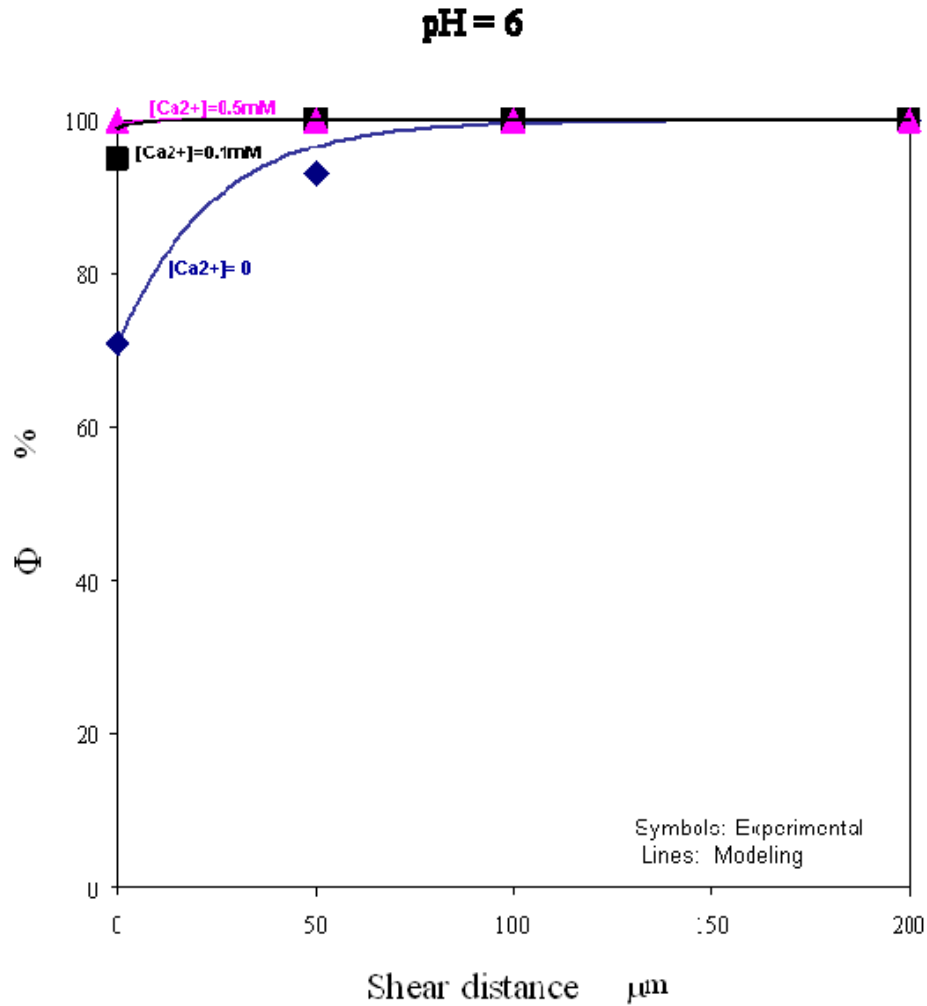


**Figure 4-13: Bitumen coalescence probability  $\Phi$  as function of shear distance  $H$  in the SPW background electrolytes with varying  $[\text{Ca}^{2+}]$  values at fixed  $\text{pH} = 6$ .** The symbols are experimental results of coalescence probabilities; different symbols correspond to different  $[\text{Ca}^{2+}]$  conditions  $\blacklozenge$ :  $[\text{Ca}^{2+}] = 0$ ,  $\blacksquare$ :  $[\text{Ca}^{2+}] = 0.1 \text{ mM}$ ,  $\blacktriangle$ :  $[\text{Ca}^{2+}] = 0.5 \text{ mM}$ . The solid lines are theoretical modeling predictions based on the two fitting parameters:  $\sigma_{\zeta} = 24 \text{ mV}$ ;  $L = 1 \text{ }\mu\text{m}$ ; the fitting was based on the assumption that these parameters were dependent on  $\text{pH}$  but independent on  $[\text{Ca}^{2+}]$ . The temperature of electrolyte media was  $22^{\circ}\text{C}$ ; the speed of shear was controlled at  $1.5 \text{ }\mu\text{m/s}$ ; the size of small droplet was around  $250 \text{ }\mu\text{m}$ , larger one  $2.5 \text{ mm}$ , the deformation ratio of small droplet was 1.1.

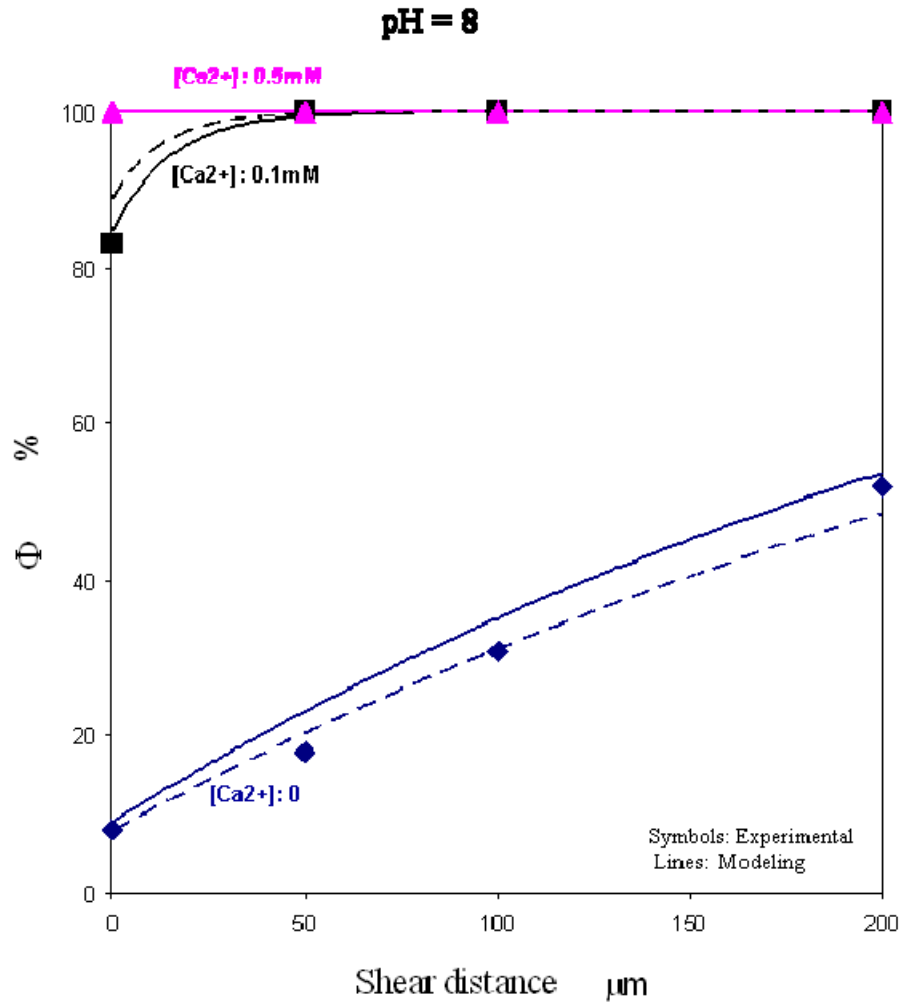


**Figure 4-14: Bitumen coalescence probability  $\Phi$  as function of shear distance  $H$  in the SPW background electrolytes with varying  $[\text{Ca}^{2+}]$  values at fixed  $\text{pH} = 8$ .** The symbols are experimental results of coalescence probabilities; different symbols correspond to different  $[\text{Ca}^{2+}]$  conditions  $\blacklozenge$ :  $[\text{Ca}^{2+}] = 0$ ,  $\blacksquare$ :  $[\text{Ca}^{2+}] = 0.1 \text{ mM}$ ,  $\blacktriangle$ :  $[\text{Ca}^{2+}] = 0.5 \text{ mM}$ . The solid lines are theoretical modeling predictions based on the two fitting parameters:  $\sigma_{\zeta} = 26 \text{ mV}$ ;  $L = 0.7 \text{ }\mu\text{m}$ ; the fitting was based on the assumption that these parameters were dependent on  $\text{pH}$  but independent on  $[\text{Ca}^{2+}]$ . The dashed lines are theoretical modeling predictions based on the values of three parameters ( $\sigma_{\zeta}$ ,  $L$ , and  $\zeta_{ave}$ ) obtained previously by Esmaili [2009]. The temperature of electrolyte media was  $22^{\circ}\text{C}$ ; the speed of shear was controlled at  $1.5 \text{ }\mu\text{m/s}$ ; the size of small droplet was around  $250 \text{ }\mu\text{m}$ , larger one  $2.5 \text{ mm}$ , the deformation ratio of small droplet was 1.1.

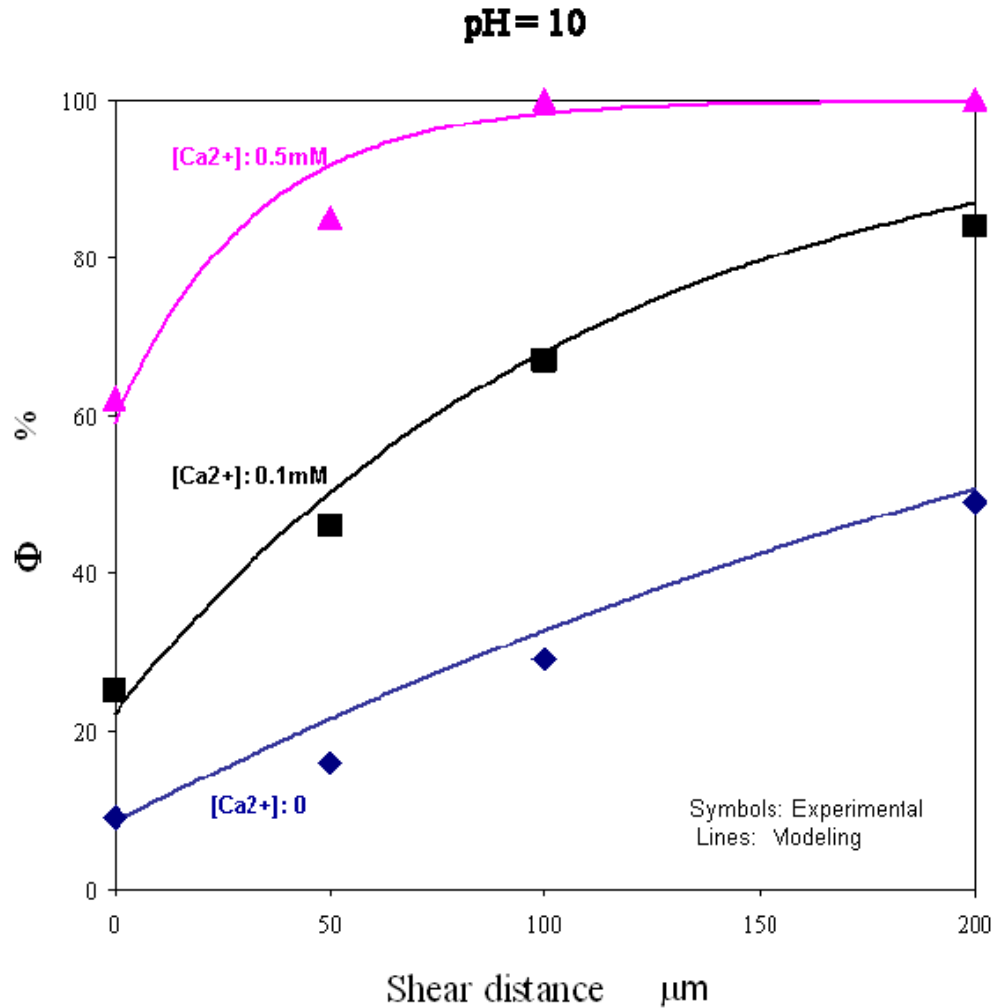


**Figure 4-15: Bitumen coalescence probability  $\Phi$  as function of shear distance  $H$  in the SPW background electrolytes with varying  $[\text{Ca}^{2+}]$  values at fixed pH = 10.** The symbols are experimental results of coalescence probabilities; different symbols correspond to different  $[\text{Ca}^{2+}]$  conditions  $\blacklozenge$ :  $[\text{Ca}^{2+}] = 0$ ,  $\blacksquare$ :  $[\text{Ca}^{2+}] = 0.1 \text{ mM}$ ,  $\blacktriangle$ :  $[\text{Ca}^{2+}] = 0.5 \text{ mM}$ . The solid lines are theoretical modeling predictions based on the two fitting parameters:  $\sigma_{\zeta} = 28 \text{ mV}$ ;  $L = 0.3 \mu\text{m}$ ; the fitting was based on the assumption that these parameters were dependent on pH but independent on  $[\text{Ca}^{2+}]$ . The temperature of electrolyte media was  $22^{\circ}\text{C}$ ; the speed of shear was controlled at  $1.5 \mu\text{m/s}$ ; the size of small droplet was around  $250 \mu\text{m}$ , larger one  $2.5 \text{ mm}$ , the deformation ratio of small droplet was 1.1.

It is apparent, through comparison between experimental data (symbols) and theoretical predictions (solid lines) in Figures 4-13 to 4-15, that our proposed model of surface charge heterogeneity (SCH) was remarkably successful in predicting the experimental coalescence probabilities under quasi-static shear condition, both in term of the trends and the magnitudes of the probabilities. Most significantly, the data suggests that, even for very high surface averaged potentials ( $\zeta_{ave}$ ), there is a probability that coalescence can occur due to “local breaching.” In addition, the larger the contact area between the two droplets, the higher the probability that they may coalesce. As such, the SCH model is able to explain the observed statistical nature and contact-area-dependence involving the coalescence of bitumen drops. Moreover, the third general observation described earlier in Section 4.2.1 (point iii) likely implies that charged domains on the bitumen-water interface are effectually “frozen” due to the extremely high viscosity of bitumen (at least for experimental time scales of 1-10 min).

There is another remarkable feature about data fitting to the SCH model: Regarding the two heterogeneous parameters ( $\sigma_\zeta$  and  $L$ ), the values currently obtained are consistent with those from a previous study by Esmaili [2009] for similar electrolyte solutions (i.e. pH = 8). Esmaili’s results were based on experimental results involving head-on contacts between similarly-sized bitumen droplets. The slight differences are well within experimental errors. Parameters obtained by Esmaili<sup>†††</sup> are also used here to calculate  $\Phi(\text{theo})$  for the different values of calcium ion concentration at pH = 8; these theoretical probabilities are shown as dashed lines in Figure 4-14. The resulting agreements are excellent. Consistency between the two studies (Esmaili’s head-on contacts and the present sliding contacts) suggests that,

---

<sup>†††</sup>  $\sigma_\zeta = 27$  mV;  $L = 0.65$   $\mu\text{m}$ ;  $\zeta_{ave} = -98, -73, -60$  mV for  $[\text{Ca}^{2+}] = 0, 0.1, 0.5$  mM respectively [Esmaili, 2009].

at least for equilibrium situation, the SCH model is robust (consistency regardless of variations in experimenter, instrument, type of experiment, etc.).

Here, it is also important to underline how pH variations may affect the degree of surface charge heterogeneity on the bitumen-water interface. The data in the Table 4-2 indicates that, while the increase of electrolyte pH slightly raised the standard deviation of the local potentials, the size of charged patch was decreased by more than three fold for the pH range tested. It appears that, if given an unchanged average  $\zeta$  potential, the wider standard deviation  $\sigma_{\zeta}$  implies higher randomness of charge distributed on individual droplet surface and the higher chances of “weak spots” for coalescence to occur. Meanwhile, for smaller values of  $L$ , there will be a larger numbers of patches over the same surface area, and variations of charge distribution will appear to be more intensified. As such, increasing the solution pH can give a more heterogeneous distribution of charges on the bitumen surface, and hence higher probability of coalescence (assuming the average  $\zeta$  potential remains constant). However, as shown in Figure 4-1, the average  $\zeta$  potential (or charge density) of bitumen was found to be increased in magnitude with the raising of the electrolyte pH, thus leading to a depressed coalescence probability of bitumen. These two factors, the average charge density and the degree of charge heterogeneity, were competing with one another in term of the experimentally observed bitumen coalescence probabilities under the influence of pH variation. It is noted that the exact origins of this pH-dependence are yet to be understood. With the above demonstration, it appears that targeted modification of charge heterogeneity, through control of pH, annealing [Feick & Velegol 2004] or adding other chemical additives (e.g poly-electrolytes and surfactant) [Feick et al. 2004], can provide a

new window for controlling colloidal stability or destabilization, together with the traditional method — altering the  $\zeta$ -potential.

Thus far, we have rationalized shear-induced coalescence behaviors at equilibrium conditions (i.e. very low constant speed of shear contact). Regarding the dynamic effects at relatively high shear speeds, although the exact reason for the observed behavior is not clear, it may be qualitatively interpreted by our proposed heterogeneity model in conjunction with lubrication theory. According to lubrication theory, the thin viscous water film between bitumen drops plays the role of lubricant and generates somehow increasingly large pressure difference between the drops as the sliding speed increases, thus preventing drop-drop contact [Cameron, 1981]. As such, the contact area during shear will be somehow reduced with higher velocity and consequently the theoretical probability will be decreased to a certain degree. Calculation of the magnitude of decline in contact area by hydrodynamic effects is complicated and beyond the scope of this study.

From the above micropipette-based oblique contact experimental results and the success of the SCH theory, we can make two suggestions at this point: (1) The classical DLVO view of colloidal stability remains sound, but should only be applied locally to charged domains (patches). There is also no need to invoke any “non-DLVO” forces to explain the observed phenomena. (2) The existence of surface charge heterogeneity is responsible for the stochastic and shear-induced nature of bitumen coalescence. However, the main drawback of the surface charge heterogeneity (SCH) theory, up to this point, is that the parameters  $\sigma_\zeta$  and  $L$  appear rather fictitious and are obtained only indirectly from curve fits. This issue is resolved next through direct AFM studies.

### **4.3 Ascertaining surface charge heterogeneity on bitumen-water interface with AFM**

#### **4.3.1 Colloidal force mapping and calculated surface charge distributions**

As introduced in Section 3.3.1, the atomic force microscopy (AFM) provides a powerful analytical tool in the mapping of colloidal forces on a surface and obtaining many valuable force curves. From this information, the distribution of surface charge (e.g. heterogeneously-charged distribution, if any) and the relevant distribution properties (e.g. correlation length) can be calculated.

In this study, one-dimensional colloidal force mapping was carried out in an SPW electrolyte in the absence of calcium ions. The pH was adjusted to three values (6, 8, and 10). At each pH, a silicon nitride AFM tip was used to quantify force curves along the bitumen-water interface. The force curves were measured at every 40-nm step, over a total distance of 2  $\mu\text{m}$ . At each local position, the colloidal force measurement between the tip and the bitumen was recorded. Typical examples of the converted force curve at different local positions are illustrated as the symbol points in the Figures 4-16 to 4-18. From these figures; all the measured long-range forces were found to be monotonically repulsive; these results suggest that the AFM tip and the bitumen surface are similarly charged (i.e. both negative), as expected. The  $\text{Si}_3\text{N}_4$  tip is negatively charged at  $\text{pH} = 6$  to 10, as shown in Figure 4-3. The bitumen surface is also negatively charged at  $\text{pH} = 6$  to 10 (as confirmed by the average  $\zeta$ -potential data measured by electrophoresis in the Figure 4-1). However, it is apparent that the measured repulsive force profiles are significantly different (in term of force magnitude)

at different locations in the same electrolyte solution; the upper bound of these forces is several times (e.g. by a factor of 5) stronger than the lower bound. This is very different from the common observation of 20% variations in the magnitude of colloidal forces when the AFM force curves are measured at the same location, as shown in Figure 4-19, in which at least 10 force measurements were performed at one location. As noted earlier, the prepared bitumen surfaces are very smooth and thus would not affect the force measurement results. The significant variations in colloidal forces along the bitumen surface are likely due to non-uniform charge distributions.

In the next step, individual force curves at different locations are fitted individually with an established theoretical model (the DLVO theory). The theoretical fitting equations and the relevant known values (e.g. the Hamaker constant for the system and the electrolyte concentration, the tip geometry-related parameters) in this study are outlined in Appendix C. In the asymmetric  $\text{Si}_3\text{N}_4$ -water-bitumen system, the surface potential (surface charge density) of  $\text{Si}_3\text{N}_4$  tip was estimated by electrophoresis (for experimental and result details, see Sections 3.4 and 4.1 respectively), and the surface potential (surface charge density) of bitumen substrate was taken as the only unknown fitting parameter. Also to be pointed out, the fitting equation (C.1) for the constant potential boundary condition (CPBC) was found to yield attractive force curves for the present system, which was not in agreement with the repulsive experimental data. Therefore, all fittings were carried out using equation (C.2) for constant charge boundary condition (CCBC). Typical examples of the fitted theoretical curves are plotted as solid lines in Figures 4-16 to 4-18.

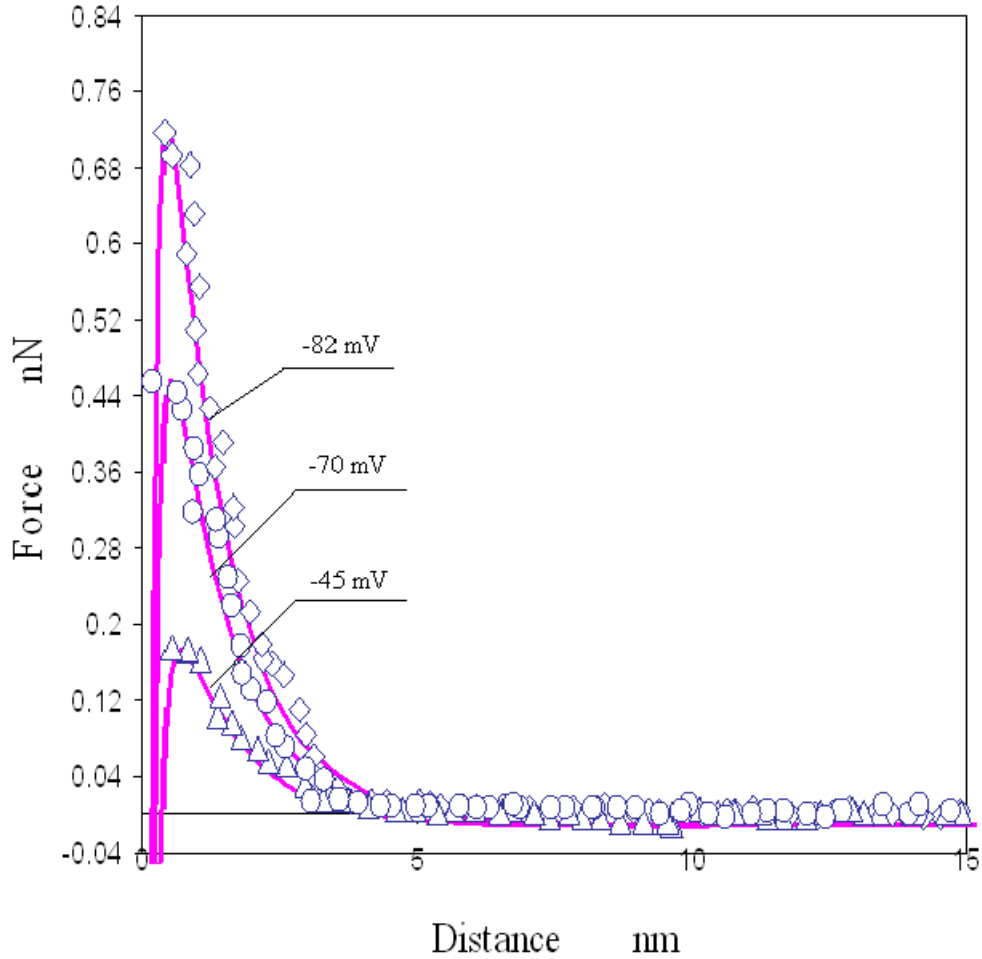


**Figure 4-16: Examples of force-distance curves obtained at different tip locations on the bitumen surface in the SPW electrolyte without calcium ion at pH = 6.** Here, symbols represent the converted force data from AFM measurements; the cantilever tip with a manufacturer’s nominal spring constant of 0.12 N/m was used. Solid lines show the theoretical fitting plots based on the DLVO equation of constant charge boundary condition in eqn (C.2) of Appendix C; the surface potential and charge density were related by the Grahame equation (C.3), the values of the related fitting parameters are given as follows: radius of the tip end  $r_s = 10$  nm, angle for the tip  $\beta = 10^\circ$ , Debye length  $\kappa^{-1} = 1.45$  nm, Hamaker constant  $A_{123} = 2.7 \times 10^{-20}$  J, surface potential of the tip  $\zeta_1 = -36.6$  mV, surface potentials of bitumen  $\zeta_2$  are respectively shown in the graph.

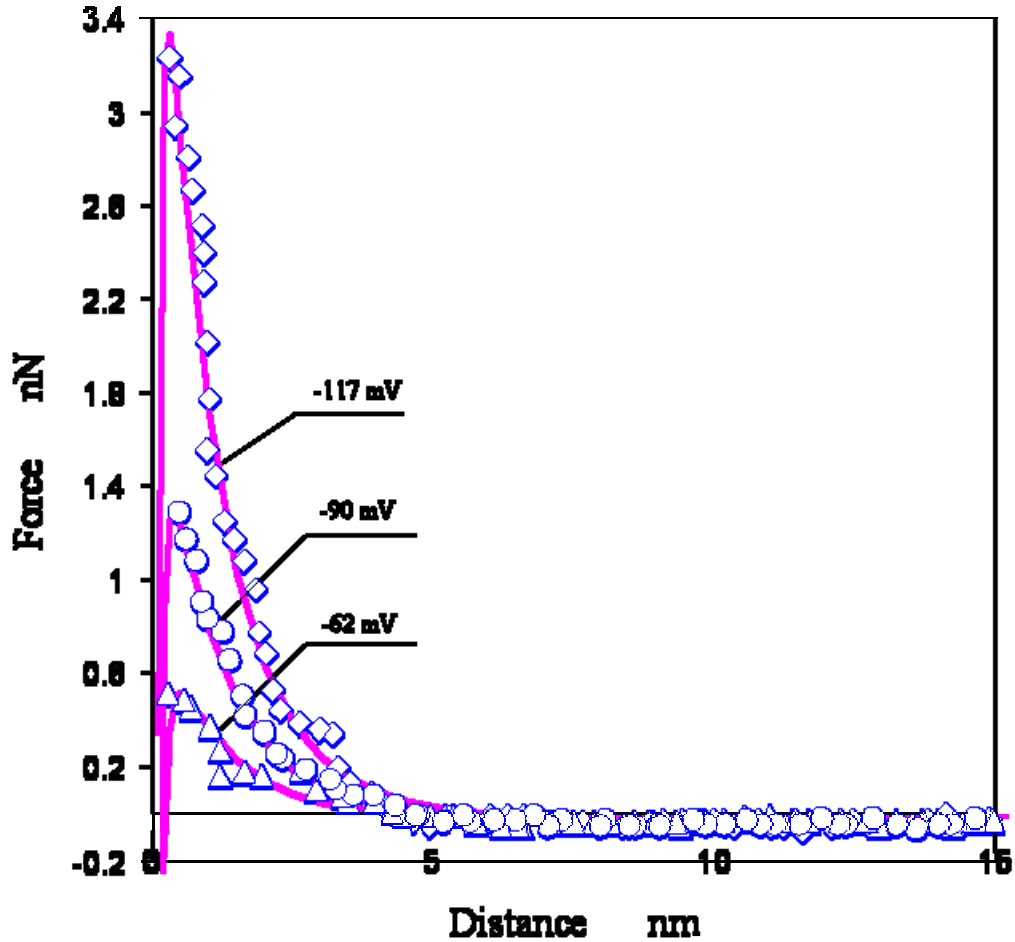
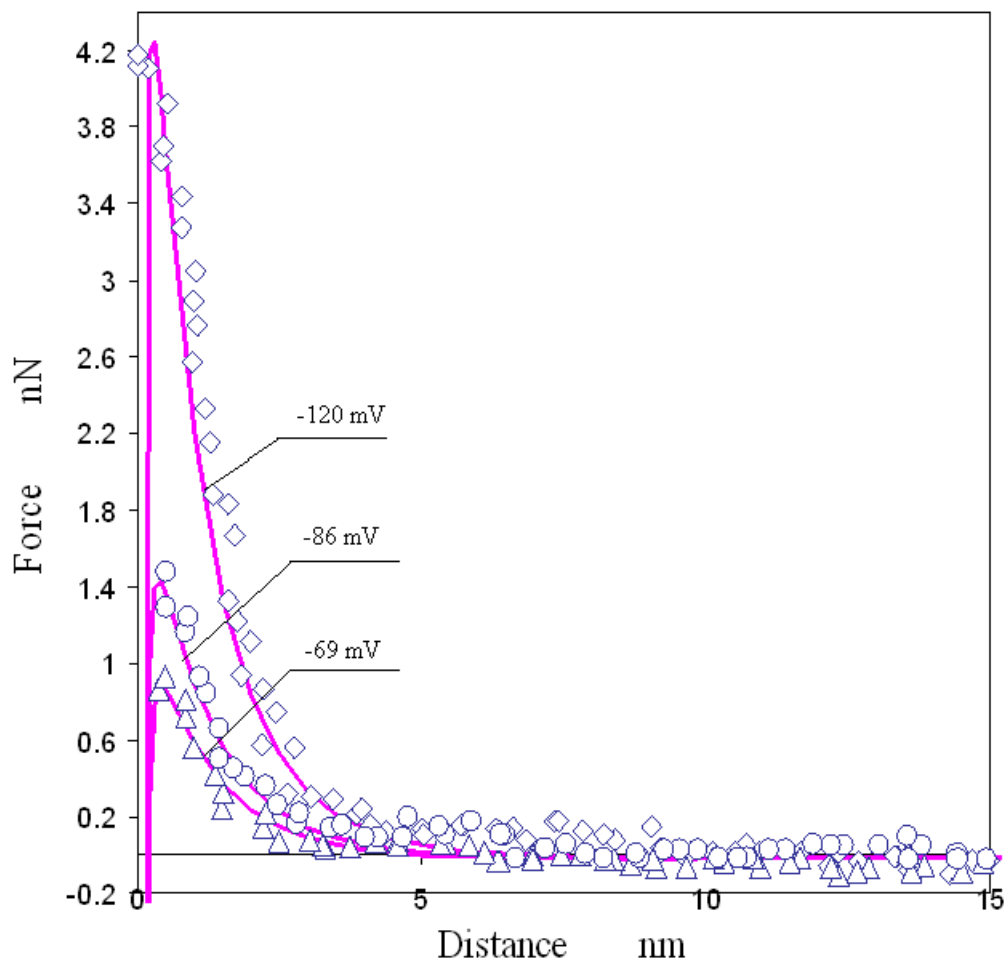
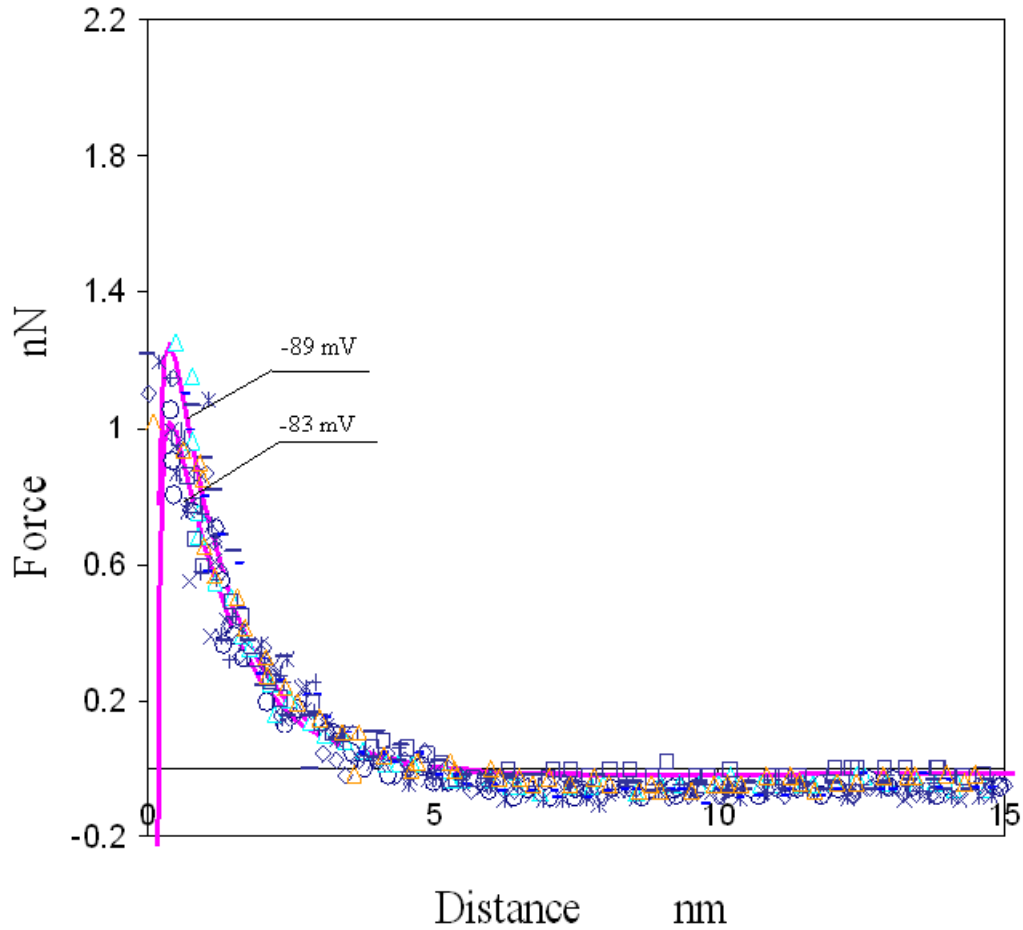


Figure 4-17: Examples of force-distance curves obtained at different tip locations on the bitumen surface in the SPW electrolyte without calcium ion at pH = 8. Here, symbols represent the converted force data from AFM measurements; the cantilever tip with a manufacturer's nominal spring constant of 0.58 N/m was used. Solid lines show the theoretical fitting plots based on the DLVO equation of constant charge boundary condition in eqn (C.2) of Appendix C; the surface potential and charge density were related by the Grahame equation (C.3), the values of the related fitting parameters are given as follows: radius of the tip end  $r_s = 10$  nm, angle for the tip  $\beta = 20^\circ$ , Debye length  $\kappa^{-1} = 1.45$  nm, Hamaker constant  $A_{123} = 2.7 \times 10^{-20}$  J, surface potential of the tip  $\zeta_1 = -52.7$  mV, surface potentials of bitumen  $\zeta_2$  are respectively shown in the graph.



**Figure 4-18: Examples of force-distance curves obtained at different tip locations on the bitumen surface in the SPW electrolyte without calcium ion at pH = 10.** Here, symbols represent the converted force data from AFM measurements; the cantilever tip with a manufacturer’s nominal spring constant of 0.58 N/m was used. Solid lines show the theoretical fitting plots based on the DLVO equation of constant charge boundary condition in eqn (C.2) of Appendix C; the surface potential and charge density were related by the Grahame equation (C.3), the values of the related fitting parameters are given as follows: radius of the tip end  $r_s = 10$  nm, angle for the tip  $\beta = 20^\circ$ , Debye length  $\kappa^{-1} = 1.45$  nm, Hamaker constant  $A_{123} = 2.7 \times 10^{-20}$  J, surface potential of the tip  $\zeta_1 = -64.5$  mV, surface potentials of bitumen  $\zeta_2$  are respectively shown in the graph.



**Figure 4-19:** The ten examples of force-distance curves obtained at the same tip locations on the bitumen surface in the SPW electrolyte without calcium ion at pH = 8. Here, symbols represent the converted force data from at least 10 AFM measurements; the cantilever tip with a manufacturer’s nominal spring constant of 0.58 N/m was used. Solid lines show the theoretical fitting plots based on the DLVO equation of constant charge boundary condition in eqn (C.2) of Appendix C; the surface potential and charge density were related by the Grahame equation (C.3), the values of the related fitting parameters are given as follows: radius of the tip end  $r_s = 10$  nm, angle for the tip  $\beta = 20^\circ$ , Debye length  $\kappa^{-1} = 1.45$  nm, Hamaker constant  $A_{123} = 2.7 \times 10^{-20}$  J, surface potential of the tip  $\zeta_1 = -52.7$  mV, surface potentials of bitumen  $\zeta_2$  are respectively shown in the graph. These curves indicate that less than 20 % variations of colloidal forces (around 5 % changes in surface potentials) were commonly observed in the AFM measurements repeated on the same substrate location.

Theoretical matches to experimental data, such as in Figures 4-16 to 4-18, were general. These good agreements suggest that the DLVO forces were the main contribution of colloidal forces and a non-DLVO force was not necessary to be taken into account. As such, the surface charge density of bitumen for individual local position was obtained after each fitting and then corresponding surface potential was calculated by the Grahame equation as expressed in (C.3) of Appendix C. After this, a plot of local surface potentials ( $\zeta$ ) versus location ( $x$ ) was made. At least two reproducible potential series plots were investigated and obtained for each pH, and the plot results are shown in Figures 4-20 through 4-22. All the figures indicate strongly fluctuating surface potentials of bitumen in the electrolytes. For example, the surface potentials of bitumen droplets in the background SPW electrolyte changed from about  $-45$  mV to  $-82$  mV at pH 6, as shown in Figure 4-20a; from about  $-62$  mV to  $-117$  mV at pH 8, as indicated in Figure 4-21a; from  $-69$  mV to  $-120$  mV at pH 10, as shown in Figure 4-22a. It is unlikely that these fluctuations are attributed to irreproducibility of AFM measurements. As illustrated in Figure 4-19, around 5% variation in the magnitude of surface potentials was obtained among at least ten consecutive measurements conducted on the same location of the bitumen surface. Hence, over 50% fluctuations of surface potentials in all the pH tested suggest the common existence of the heterogeneously-distributed charge characteristics on the bitumen surface.

Figure 4-20: pH = 6

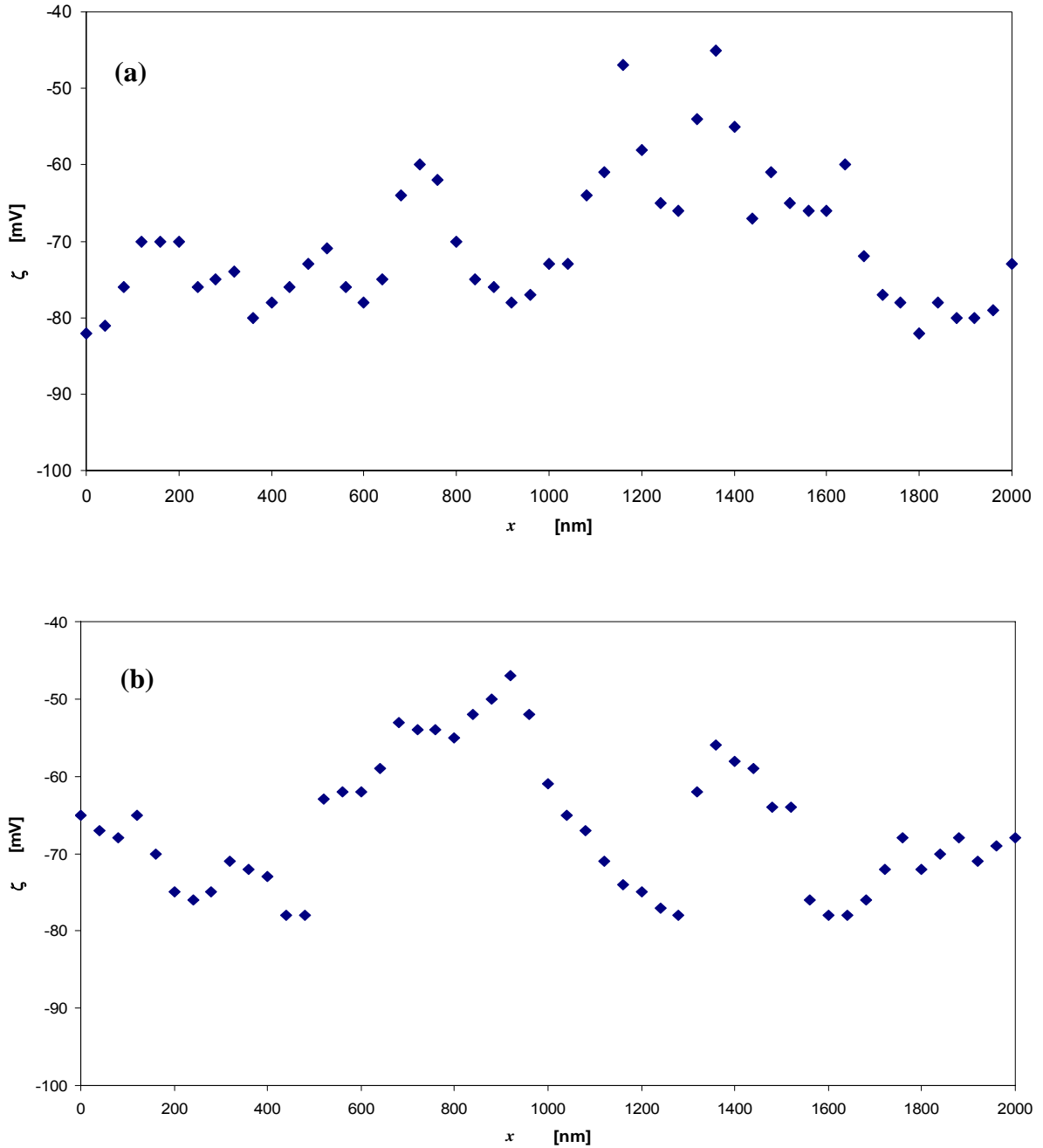


**Figure 4-20 (a) and (b): The two plots of random potential signal from bitumen-water interface at pH = 6 (SPW,  $[Ca^{2+}] = 0$ ).** The x-axis represents the lateral position of bitumen sample relative to the AFM tip (40 nm per step offset adjustment); y-axis is the local potential, which is determined by the parameter to be fit AFM-obtained force vs. separation curve at a local position, assuming that  $\zeta$  equals to surface potential.

Figure 4-21: pH = 8

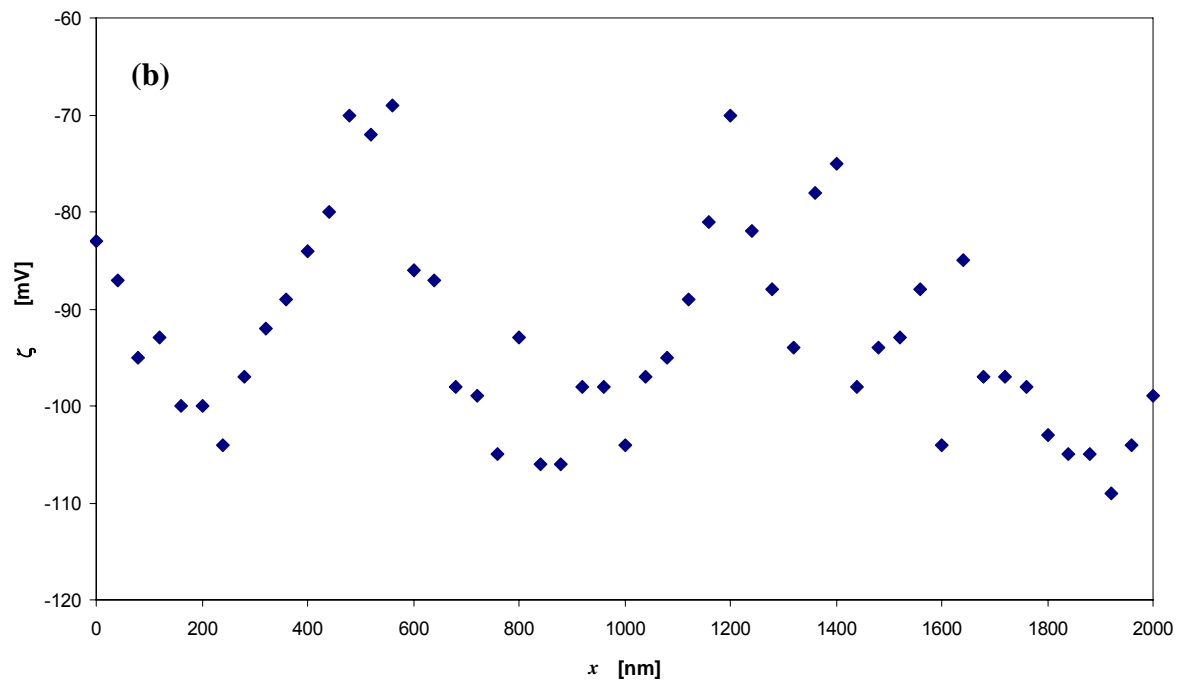
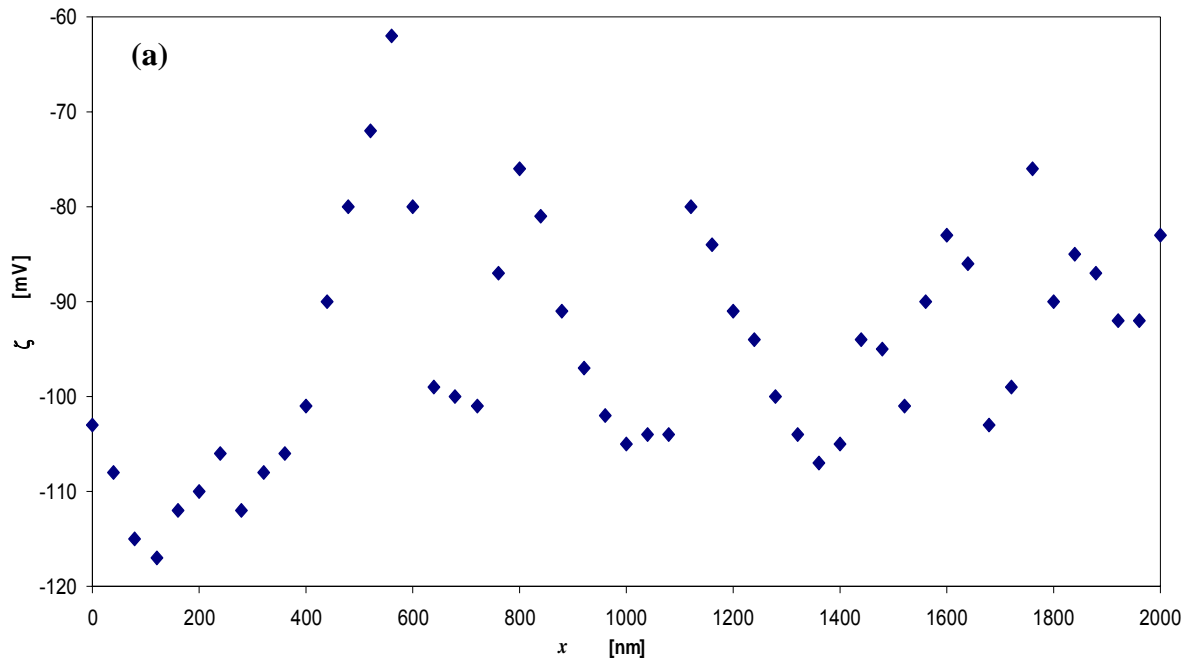
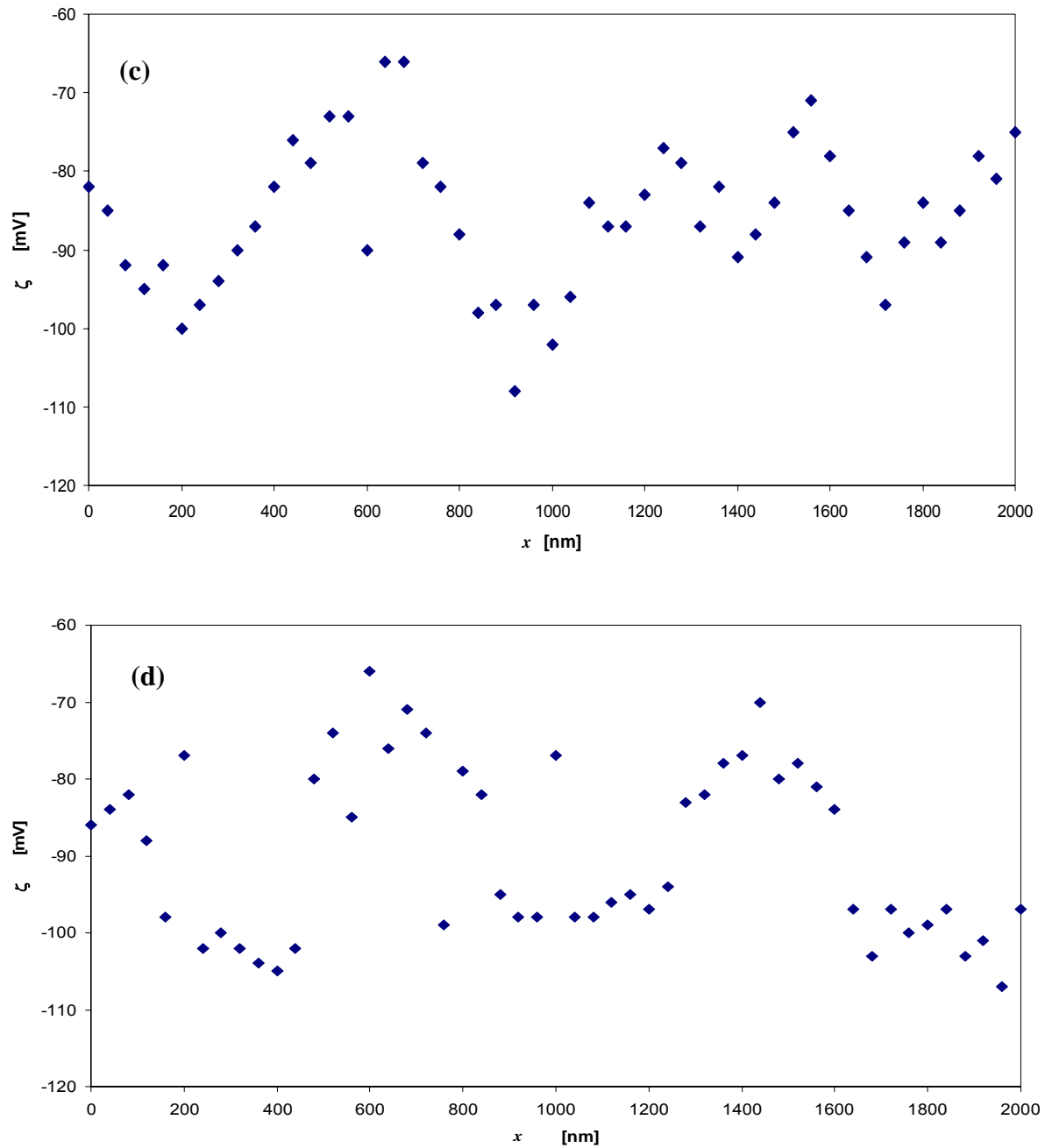
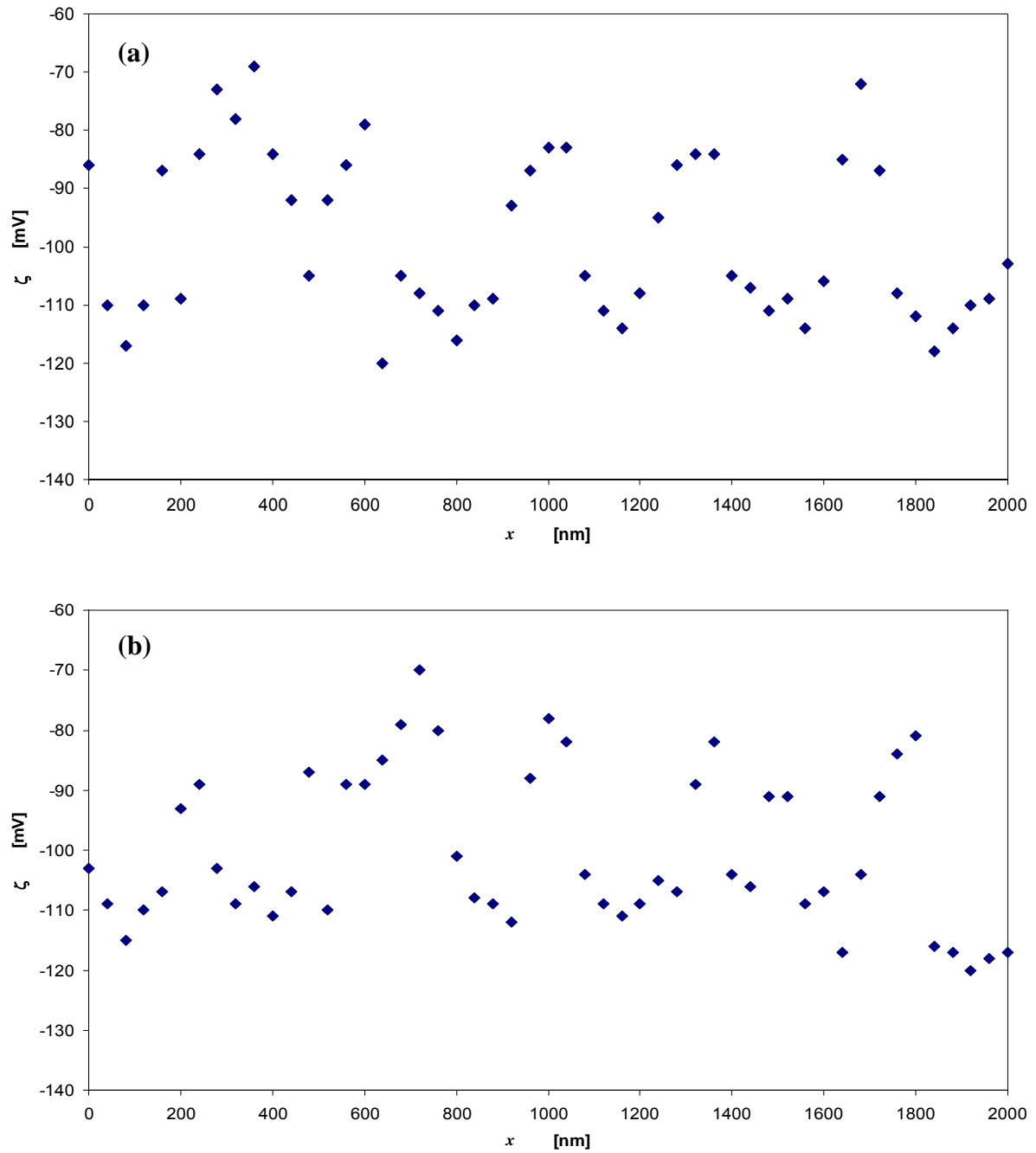


Figure 4-21: pH = 8



**Figure 4-21 (a) - (d): The four plots of random potential signal from bitumen-water interface at pH = 8 (SPW,  $[Ca^{2+}] = 0$ ).** The x-axis represents the lateral position of bitumen sample relative to the AFM tip (40 nm per step offset adjustment); y-axis is the local potential, which is determined by the parameter to be fit AFM-obtained force vs. separation curve at a local position, assuming that  $\zeta$  equals to surface potential.

Figure 2-22: pH = 10



**Figure 4-22 (a) and (b): The two plots of random potential signal from bitumen-water interface at pH = 10 (SPW,  $[Ca^{2+}] = 0$ ).** The x-axis represents the lateral position of bitumen sample relative to the AFM tip (40 nm per step offset adjustment); y-axis is the local potential, which is determined by the parameter to be fit AFM-obtained force vs. separation curve at a local position, assuming that  $\zeta$  equals to surface potential.

### 4.3.2 Autocorrelation functions of heterogeneous charge distributions

Having acquired the above plots of random potentials signals on the bitumen-water interface, it was possible to calculate the corresponding mean values of local potentials  $\zeta_{ave}$ ; their results are shown in Table 4-3. Regarding the estimation of the patch size  $L$ , as described in Section 3.3.1, at first we needed to construct the correlogram, in which the series of well-defined *autocorrelation function* (ACF) values of the random  $\zeta$ -potential signal were plotted against the location displacement ( $x$ ).

In practice, given  $N$  local  $\zeta$ -potentials  $\zeta_0, \zeta_1 \dots \zeta_k \dots \zeta_{N-1}$ , along the lateral locations having the mean value  $\zeta_{ave}$ , such as any one plot in Figures 4-20 through 4-22, one was able to form  $N - k$  pairs of observations, namely,  $(\zeta_0, \zeta_k), (\zeta_1, \zeta_{k+1}), \dots, (\zeta_{N-1-k}, \zeta_{N-1})$ , where each pair of observations was separated by lag  $k$  interval. Then, the autocorrelation function (ACF) between two observations at lag  $k$  apart,  $\zeta_x$  and  $\zeta_{x+k}$ , were calculated, using the following formula [Chatfield, 2004]:

$$ACF(k) = Cov(k) / Cov(0) \quad (4.4)$$

In eqn (4.4),  $Cov(k)$  is the series of auto-covariance coefficient at lag  $k$ , which is given by

$$Cov(k) = \frac{1}{N} \sum_{x=0}^{N-1-k} (\zeta_x - \zeta_{ave})(\zeta_{x+k} - \zeta_{ave}) \quad (4.5)$$

for  $k = 0, 1, 2, \dots, M$  ( $M < N =$  the total number of experimental data points, was 51 in the present case). It is obvious that,  $k = 0$  would lead to the reference auto-covariance coefficient  $Cov(0)$  and the corresponding  $ACF(0)$ . Of course,  $ACF(0)$  was always unity, but was still plotted for comparative purposes. It is also noted that the 40 nm per step was used

in the offset adjustment on detecting the random  $\zeta$  potential signal, and therefore the lag  $k$  and the location displacement  $x$  were related with  $x = 40 k$ . With the use of these definitions, the ACF versus  $x$  plots were obtained and the resulting correlograms for all the above potential signals in Figures 4-20 to 4-22 are shown as the symbols in Figures 4-23 through 4-25, respectively.

Interpreting the meaning of the correlogram was not always easy, especially when the number of experimental data was limited and a finite step size was used (such as in the present case). Local truncation error would commonly be generated. This highlights one of the difficulties in interpreting the correlogram, in which a series of ACF values were quite likely to contain “unusual” outcomes, even when no real physical effects were present. If the experimental measurements became infinitely large, those “artificial” effects would likely be “smoothed out”. Here, we are also showing the outcomes of producing the plots of ACF values against distance  $x$ , from the physically-sound signal of the Ornstein-Uhlenbeck (OU) process, by changing the number of signal processing data (similar to varying experimental data). The brief description of the OU process and its exact formula that applies for any size of distance interval  $\Delta x$  are noted in Appendix D. As shown in Figure 4-26, when small amount of signaling number (51 points in this case) is chosen, it is obvious to see the significant “ringing” pattern of ACF values along with distance  $x$ . If we increase the number of signaling while keeping other factors (including discrete distance step of interval, the mean value and standard deviation of the signal) the same, the generated ACF plots will have less and less significant fluctuations. When the number of signaling is sufficiently large, the produced ACF plot will decay smoothly and exponentially. It should be pointed out that

herein the ACF plots have the same exponential decay length if being fitted with least square minimization by a simple exponentially-decayed function (shown in solid lines in Figure 4-26), even though they have very different degree of significance in “ringing” patterns. (This fitting method will also be adopted to generate the distance of correlation between the local potential signals in our study).

In addition, it is physically reasonable on the grounds that the fluctuating material property (local surface charge in this case) has values that are correlated only for very short distance intervals. Therefore, we suggest that this local truncation error was a possible origin of generating the “ringing” pattern, which was somehow observed from the correlograms in Figures 4-23 through 4-25. Even though having the above-mentioned difficulty, it is clear from the figures that the correlogram series generally showed some degree of correlation characterized by a fairly large value of ACF(1) followed by one or more further “significant” values, which, while greater than zero, tended to become successively smaller. In addition, despite the existence of “artificial ringing,” the ACF series of the zeta potential data exhibited a fairly clear exponential decay. This pattern of correlation revealed that local surface charges at the bitumen-water interface were correlated (influenced) by their nearest neighbours. The characteristic distance of decay in the ACF can be interpreted as a *correlation length*  $\lambda$ , which is a measure of the distance that two locations must be separated before their local potentials become uncorrelated. We postulate that while the oscillations (the “ringing”) is likely an artifact, the overall exponential-like decay is a real physical effect. To decouple the two, we “force-fitted” the oscillating ACF data to a simple exponential decay (shown as the solid lines in the correlograms in Figures 4-23 through 4-25).

Then, we associated the correlation length  $\lambda$  with the size of the patch  $L$  proposed in the SCH model. *The following point is important:* while  $L$  and  $\lambda$  are both measures of the patch size, there is no reason to equate the two quantities. We expect the values of  $L$  and  $\lambda$  to be strongly correlated — perhaps maintaining a constant ratio of  $L/\lambda$  as the patch size changes.

Table 4.3 shows the results of the three parameters at different pH values with the similar SPW electrolytes and in the absence of calcium ions. The mean values  $\zeta_{\text{ave}}$  of the  $\zeta$ -potential signals were calculated from the local potential signal data in Figures 4-20 to Figure 4-22, and the correlation length  $\lambda$  was estimated from the decay constant of an exponential function being fitted to the correlograms in Figures 4-23 through 4-25. It is clear from the table that reproducibility of data at all pH values was very good. For example, the discrepancy between values of  $\zeta_{\text{ave}}$  at pH = 8 was only about 10% and might be the results of calibrating the spring constants of the different cantilevers used in the AFM force measurement.

Figure 23: pH = 6

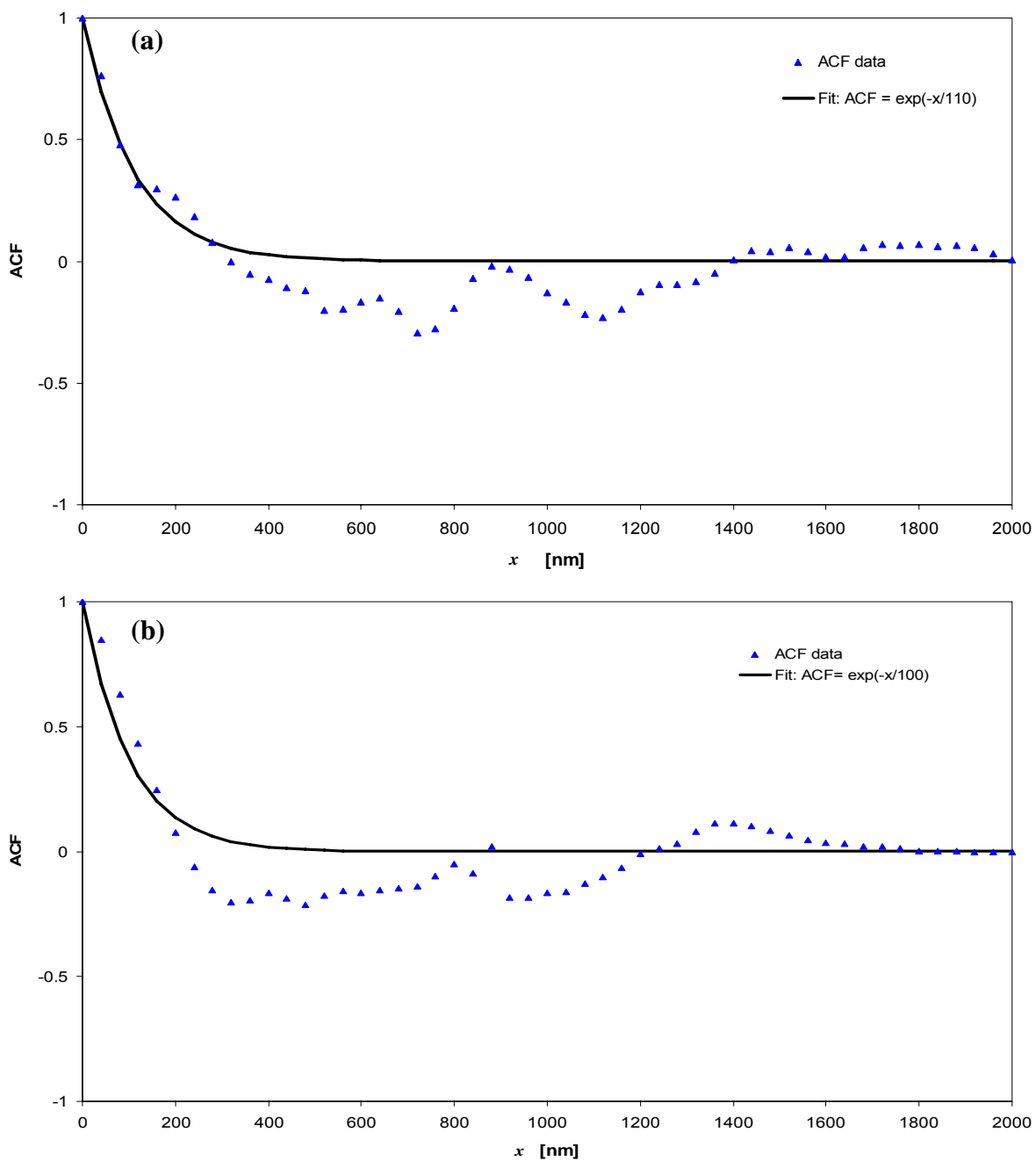


**Figure 4-23 (a) and (b):** The two correlograms of random  $\zeta$  potential signal from bitumen-water interface at pH = 6 (SPW,  $[\text{Ca}^{2+}] = 0$ ), in which the series of the autocorrelation function (ACF) values were plotted against the location displacement ( $x$ ). Here, symbol points represent the calculated ACF data from the AFM study; solid lines show the fitted exponential decay functions. The decay lengths of the fitted equations were listed in Table 4-3.

Figure 4-24: pH = 8

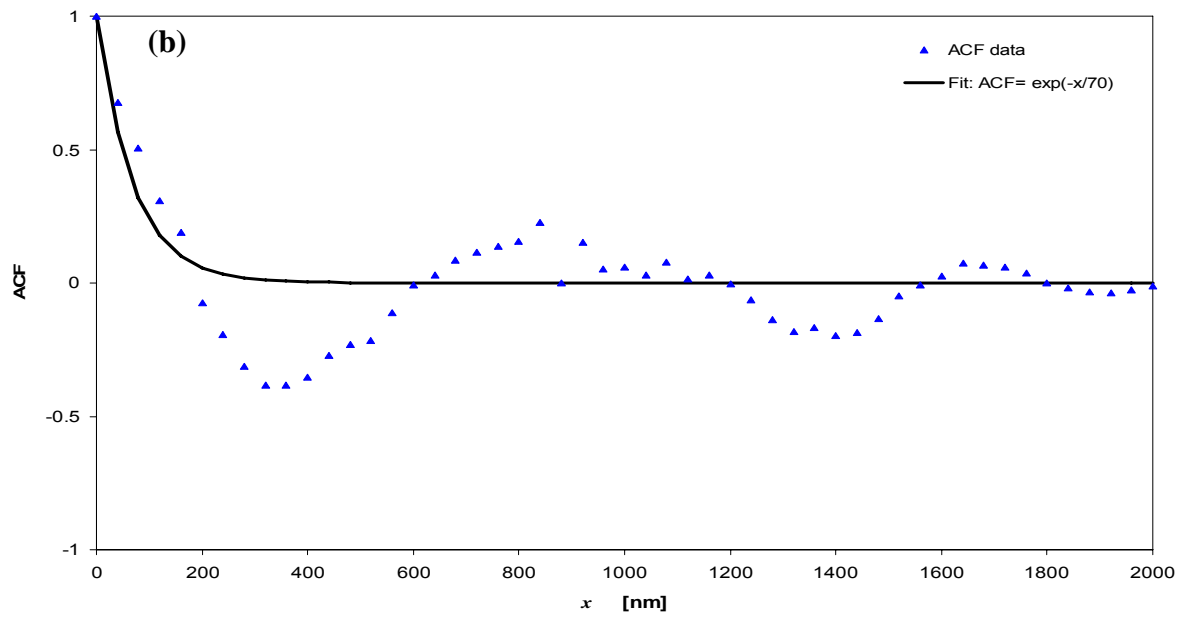
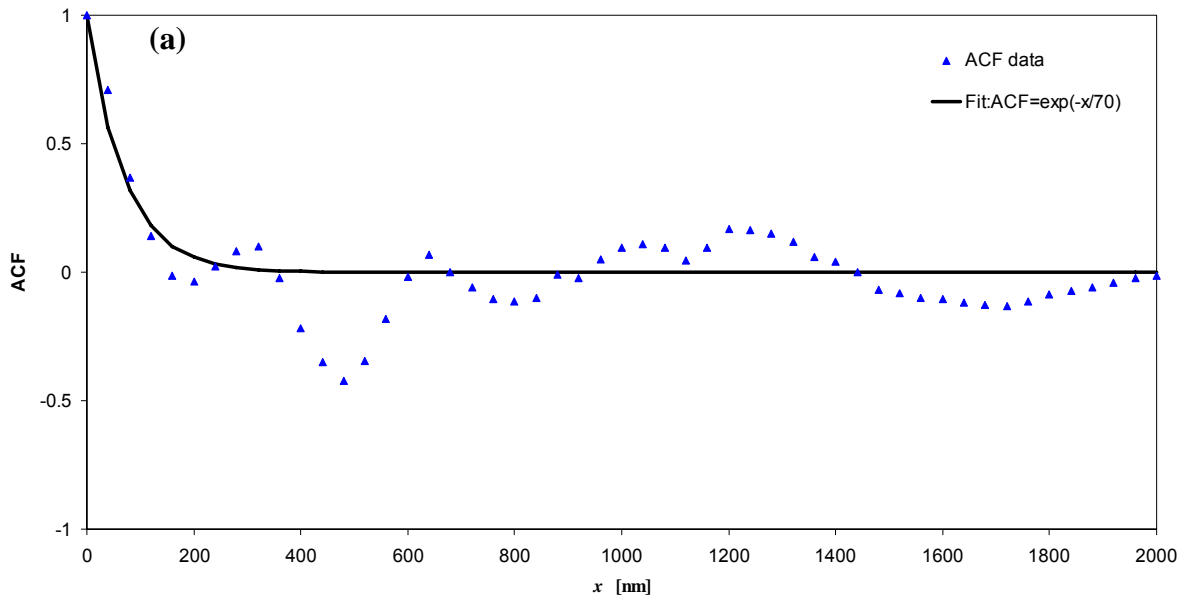
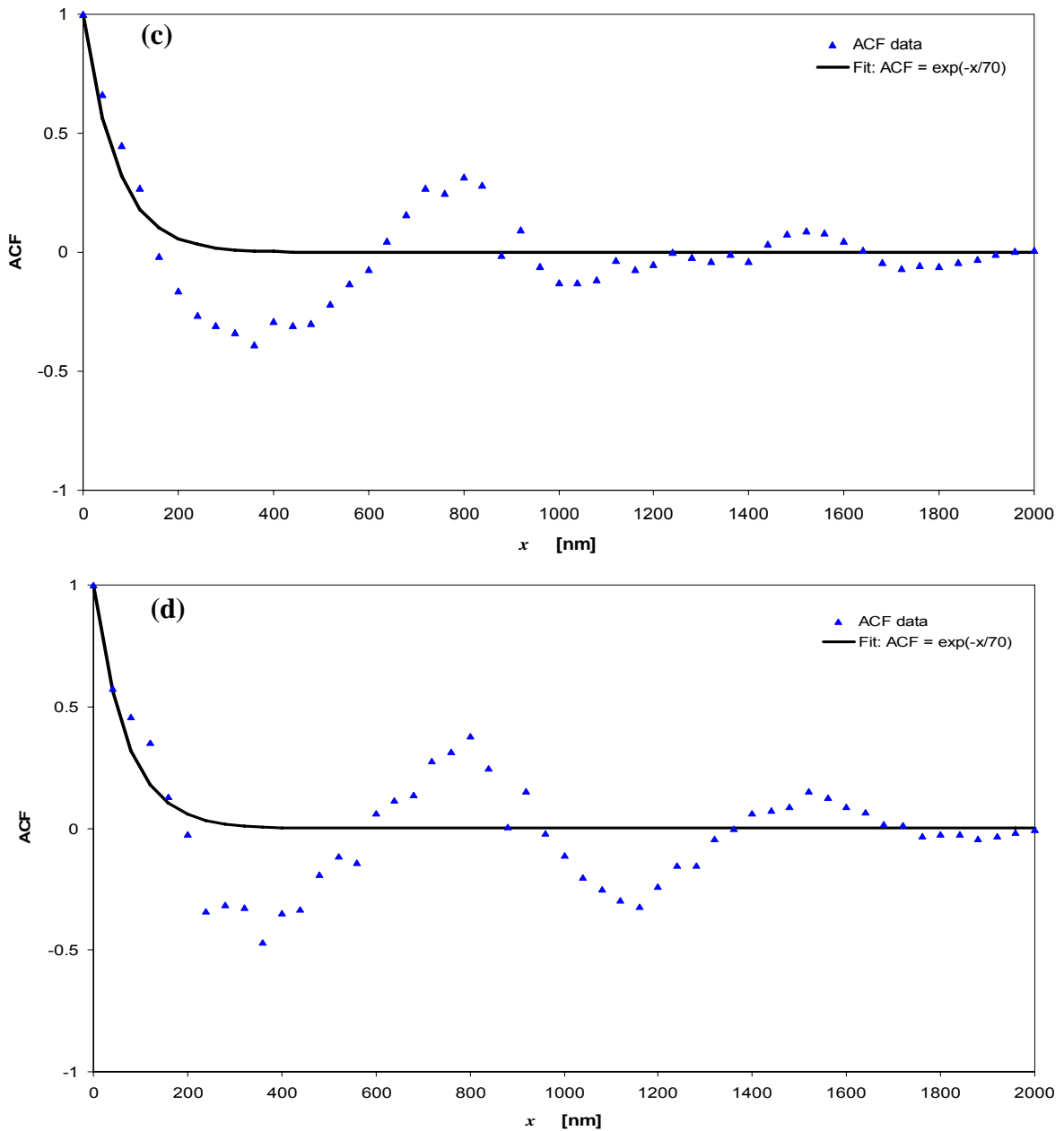
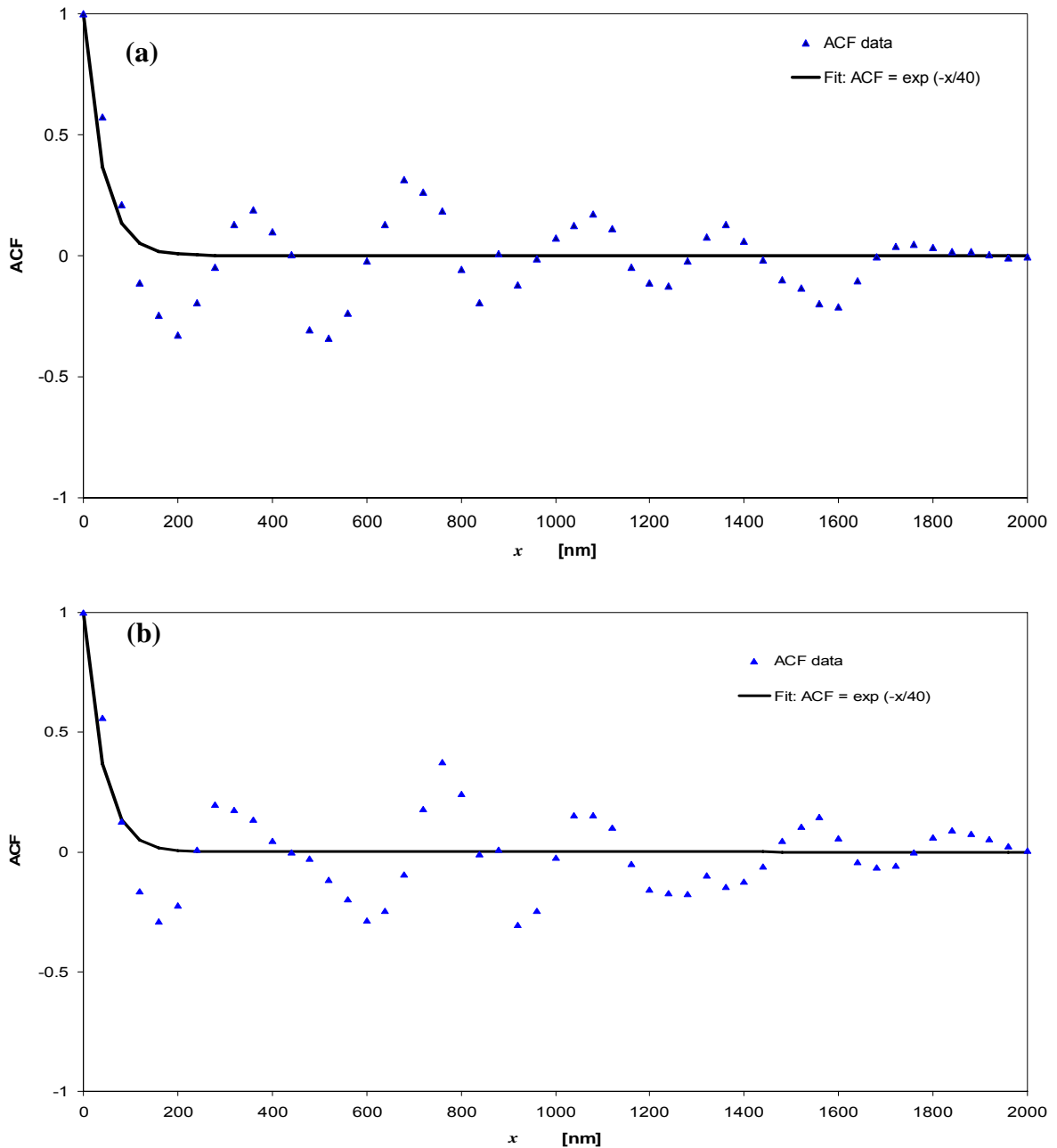


Figure 4-24: pH = 8



**Figure 4-24 (a) - (d): The four correlograms of random  $\zeta$  potential signal from bitumen-water interface at pH = 8 (SPW,  $[Ca^{2+}] = 0$ ), in which the series of the autocorrelation function (ACF) values were plotted against the location displacement ( $x$ ). Here, symbol points represent the calculated ACF data from the AFM study; solid lines show the fitted exponential decay functions. The decay lengths of the fitted equations were listed in Table 4-3.**

Figure 2-25: pH = 10



**Figure 4-25 (a) and (b):** The two correlograms of random  $\zeta$  potential signal from bitumen-water interface at pH = 10 (SPW,  $[\text{Ca}^{2+}] = 0$ ), in which the series of the autocorrelation function (ACF) values were plotted against the location displacement ( $x$ ). Here, symbol points represent the calculated ACF data from the AFM study; solid lines show the fitted exponential decay functions. The decay lengths of the fitted equations were listed in Table 4-3.

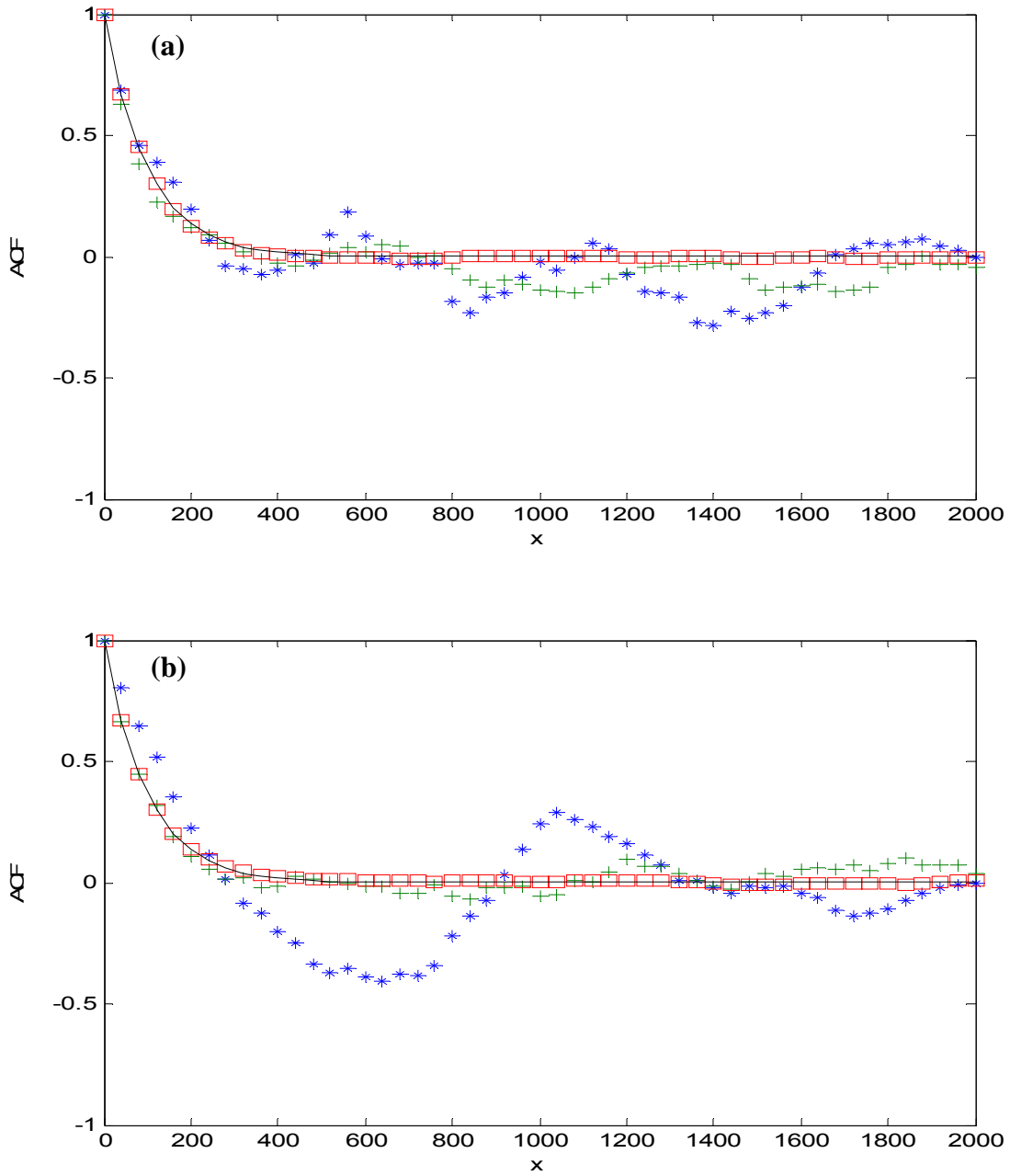


**Figure 4-26 (a) and (b):** The two examples of showing the effect of the number of processing data on the correlogram of Ornstein-Uhlenbeck (OU) signal. The formula of OU signal is shown in the equation (D.2) in Appendix D. Here, symbols represent the calculated ACF data from the same OU signal with increasing number of processing data while keeping interval of steps the same ( $= 40$ ); “\*”: 51 points, “+”: 501 points, “□”: 5001 points. Solid lines show the fitted exponential decayed functions.

**Table 4-3: Summary of the two parameters calculated from local  $\zeta$ -Potentials data and correlogram charts with repeated sets of experiments at different pH values.** Here, the mean value  $\zeta_{ave}$  of the  $\zeta$  potential signals was calculated from the signal data in Figure 4-20 to Figure 4-22, and the correlation length  $\lambda$  was approximately equivalent to the decay constant of the fitted exponential equation to the ACF data in Figures 4-23 through 4-25.

pH	Figure No.	$-\zeta_{ave} / \text{mV}$	$\lambda / \text{nm}$
6	4-20 a / 4-23 a	70.4	110
	4-20 b / 4-23 b	66.5	100
8	4-21 a / 4-24 a	95.1	70
	4-21 b / 4-24 b	92.6	70
	4-21 c / 4-24 c	85.7	70
	4-21 d / 4-24 d	89.7	70
10	4-22 a / 4-25 a	98.9	40
	4-22 b / 4-25 b	100.4	40

**Table 4-4: Comparison between the two parameters based on two different approaches of quantifying surface charge heterogeneity on the bitumen droplet immersed in the SPW electrolyte in absence of calcium ion at different pH values.** Here, the parameters of model were quoted from the Figure 4-1 and Table 4-2, being fit to the oblique contact experiments. The parameters of AFM study were collected from the Table 4-3.

pH	Method	$-\zeta_{ave} / \text{mV}$	Length scale/ $\mu\text{m}$
6	Model	65	1
	AFM study	68	0.1
8	Model	93	0.7
	AFM study	91	0.07
10	Model	110	0.3
	AFM study	100	0.04

### 4.3.3 Comparison between heterogeneous parameters obtained in two approaches

Table 4-4 summarizes the comparative results among the two parameters related to charge heterogeneity (i.e. the average zeta potential  $\zeta_{ave}$  and length scale of charged patch) based on two different approaches: First, surface charge heterogeneity was indirectly acquired by fitting the SCH model to data obtained from oblique contact experiments (this is called the “Model” method in Table 4-4). Thereafter, we applied AFM force measurements to directly ascertain the local  $\zeta$  potential distributions along the bitumen-water interface (called the “AFM study” method in Table 4-4). It is clear from the Table 4-4 that data from AFM study and from model fitting were consistent with one another at all three pH values tested. More specifically, there are four indications which suggest good agreement between SCH model fitting and direct AFM measurements: (1) findings from the two approaches suggest existence of heterogeneous charge distributions on the bitumen-water interface, which played a significant role in the shear-induced coalescence between bitumen droplets. (2) The two methods both revealed the strong influence of pH on  $\zeta_{ave}$  and  $L$ . Moreover, the same trends are seen (e.g. increasing the solution pH not only increased the magnitude of  $\zeta_{ave}$ , but also gave a more heterogeneous distribution of charges on the bitumen surface through a significant decrease in  $L$ ). (3) The average zeta potential  $\zeta_{ave}$  was measured by AFM and by electrophoresis (for the same pH). With a maximum of 10% difference, agreement was indeed remarkable (although the AFM result should be taken with caution due to the very crude DLVO equation that was used). (4) Perhaps the most encouraging trend is found in the last column of Table 4-4. The estimates of “patch size” by the two methods appear to maintain a constant ratio of about 10. This ratio is  $L/\lambda$ , where  $L$  is the characteristic patch

size in the context of the SCH model (Section 2.3.2), while  $\lambda$  is from direct AFM measurements — it is the decay length of the autocorrelation function of the “zeta noise” along the bitumen surface. As discussed at the end of Section 4.3.2, seeing a constant ratio of  $L/\lambda$  — especially when the absolute values are varying by more than a factor of 3 (as the pH changes from 6 to 10) — is strong indication that the postulated parameters in the SCH model ( $L$ ,  $\sigma_\zeta$  and  $\zeta_{\text{ave}}$ ) are indeed real.

## Chapter 5 : Conclusions and Recommendations

Understanding the influence of shear on bitumen coalescence is crucial for maximizing the water-based bitumen extraction performance and potential for generating significant economic and environmental benefits. To this end, the impact of the shear on the coalescence probabilities of bitumen droplets in aqueous media was systematically studied. It was shown from experiments that the bitumen droplets did coalesce, albeit randomly, with larger distances of shear contact inducing higher tendencies for coalescing. To rationalize this, we proposed a theory of surface charge heterogeneity (SCH) and successfully interpreted the stochastic and shear-induced nature of the coalescence process. To give credence to the SCH model, we have also used the AFM technique to directly probe charge heterogeneities at the bitumen-water interface. The AFM results provided strong support for the SCH theory — in terms of the existence of surface charge variations, as well as the magnitudes of the heterogeneity parameters.

Micropipette-based techniques were developed to quantify the bitumen coalescence probability in the simulated process water (SPW) through accurately controlling the shear distance and speed in oblique contact experiments. The varying experimental parameters, including  $\zeta$ -potentials of the bitumen drops (through manipulation of solution pH and  $[\text{Ca}^{2+}]$  of the electrolyte), distance of shear contact, and shear speed, were observed to have significant effects on the drop coalescence probabilities. The probability was found to increase remarkably with longer shear distances and lower magnitudes of  $\zeta$ -potential (by increasing  $[\text{Ca}^{2+}]$  and/or decreasing pH); however, it was only very slightly diminished by higher shear speeds. In order to compare the oblique contact results with the prediction of

traditional DLVO formalism, the  $\zeta$ -potential of bitumen in SPW, with varying pH and  $[\text{Ca}^{2+}]$ , was first determined (this was required for the estimation of the electrostatic repulsion). It was found that, according to traditional DLVO theory, the measured zeta potentials were sufficiently large to prevent any coalescence between the bitumen droplets. Moreover, the traditional theory could not explain the stochastic nature and contact-area-dependence of the coalescence process.

The underlying mechanism behind the coalescence phenomena seemed to be one which involves random surface charge distributions. We proposed that the complete deviation from traditional DLVO prediction was due to the existence of randomly charged “domains” on the bitumen-water interface. The surface charge heterogeneity (SCH) model was developed. Remarkably, this model was able to successfully predict the experiential evidences and data under a wide range of conditions if one assumes that the two undetermined heterogeneous parameters (standard deviation of the random potentials  $\sigma_\zeta$  and the size of the patches  $L$ ) were dependent on the pH but not on  $\text{Ca}^{2+}$  ion concentration. It was suggested, from the data fitting, that the characteristic length of the charged patches was about 0.3-1.0  $\mu\text{m}$  for the pH tested, with the patch size decreasing as the pH was raised.

Finally, an AFM-based technique was used to directly detect charge variations on the bitumen-water interface. One dimensional colloidal force mapping was performed stepwise along the surface of a flat bitumen substrate in the SPW at different pH values. *Local* zeta potentials were obtained by fitting the measured force curves to traditional DLVO theory. All the AFM-acquired plots of local  $\zeta$ -potentials versus location confirmed the presence of heterogeneous charges distributed along the bitumen surface. Also, the parameter of average

$\zeta$ -potential determined from the random potential plots was shown to be roughly in the same trend and magnitude range with those acquired from the earlier approach — the surface charge heterogeneity (SCH) model fit to the oblique contact results. In addition, autocorrelation function (ACF) correlograms were constructed to reveal any possible spatial correlation among the measured local  $\zeta$ -potentials. It was shown that, despite some artificial “ringing” effect caused by truncation errors, the correlogram series were characterized by overall exponential-like decays — beginning with strong correlation near the reference point, and falling to zero over some characteristic distance (denoted  $\lambda$  in this study). Strong correlation was shown between the decay length  $\lambda$  and the patch size  $L$  (the latter is in the context of the SCH model), a fact which lends credence to the validity of the SCH model.

Regarding future work, one of the recommendations should be on further refining the current approach of oblique contact experiments to investigate the effect of other parameters, such as the presence of solids or fine particles, the temperature, and the addition of surfactants and different chemicals, on the colloidal interactions of bitumen droplets and their resulting coalescence behaviors. Another area of interest is to further improve the AFM technique to carry out mapping of surface charge variations on bitumen in two dimensions and providing valuable information on the regional charge correlations. The cantilever tips should be made of materials other than silicon nitride and have chemical functionality that is chemically inert. This way, a sufficiently large number mapping measurements can be performed and the accuracy of calculating the surface potential data and autocorrelation function charts will be improved.

## References:

- Adamson, A. W. *Physical Chemistry of Surfaces*, 5<sup>th</sup> Ed.; Wiley-Interscience: New York, 1990.
- Aksoy, B. S. *Hydrophobic Forces in Free Thin Films of Water in the Presence and Absence of Surfactants*; PhD Thesis, Virginia Polytechnic Institute and State University, Blackburg, Virginia, USA, 1997.
- Basheva, E. S.; Gurkov, T. D.; Ivanov, I. B. Bantachev, G. B. ; Campbell, B. ; Borwankar, R. P. Size Dependence of the Stability of Emulsion Drops Pressed against a Large Interface. *Langmuir* **1999**, 15, 6764-6769.
- Bhattacharjee, S.; Ko, C. H.; Elimelech, M. DLVO Interaction between Rough Surfaces. *Langmuir* **1998**, 14, 3365-3375.
- Butt, H. J.; Cappella, B.; Kappl, M. Force Measurements with the Atomic Force Microscope: Technique, Interpretation and Application. *Surf. Sci. Reports* **2005**, 59, 1-152.
- Butt, H. J.; Graf, K.; Kappl, M. *Physics and Chemistry of Interfaces*; Wiley-VCH: Weinheim, Germany, 2003.
- Cameron, A. *Basic Lubrication Theory*, 3<sup>rd</sup> Ed.; Ellis Horwood Ltd: West Sussex, England, 1981.
- Castro, F.; Sanchez, A.; Wio, H. Reentrance Phenomena in Noise-Induced Transitions. *Phys. Rev. Lett.* **1995**, 75, 1691-1694.
- Chatfield, C. *The Analysis of Time Series: an Introduction*, 6<sup>th</sup> Ed.; CRC Press Company, New York, USA, 2004.
- Chung, H. S.; Hogg, R. Stability Criteria for Fine-Particle Dispersions. *Colloids Surf.* **1985**, 15, 119-135.
- Clark, K. A. Athabasca Oil Sands – Fundamentals Affecting Development. *Can. Petro.* **1966**, 7, 18-25.
- Czarnecki, J. The Effect of Surface Inhomogeneities on the Interactions in Colloidal Systems and Colloidal Stability. *Adv. Colloid Interf. Sci.* **1986**, 24, 283-319.
- Dai, Q.; Chung, K. H. Bitumen-Sand Interaction in Oil Sand Processing. *Fuel* **1995**, 74, 1858-1864.

- Danov, K. D.; Denkov, N. D.; Petsev, D. N.; Ivanov, I. B.; Borwankar, R. Coalescence Dynamics of Deformable Brownian Emulsion Droplets. *Langmuir* **1993**, 9, 1731-1740.
- Derjaguin, B.; Landau, L. Theory of Stability of Highly Charged Liophobic Sols and Adhesion of Highly Charged Particles in Solutions of Electrolytes. *Zhurnal Eksperimentnoi I Tereticheskoi Fiziki* **1945**, 15 (11), 663-682.
- Deshikan, S. R.; Papadopoulos, K. D. London-VDW and EDL Effects in the Coalescence of Oil Drops. *J. Colloid Interf. Sci.*, **1995**, 174, 302-312.
- Drelich, J.; Long, J.; Yeung, A. Determining Surface Potential of The Bitumen-Water Interface at Nanoscale Resolution Using Atomic Force Microscopy. *Can. J. Chem. Eng.* **2007**, 85, 625-634.
- Ducker, W. A.; Senden, T. J.; Pashley, R. M. Direct Measurement of Colloidal Forces Using an Atomic Force Microscope. *Nature* **1991**, 353 (6341), 239-241.
- Elimelech, M.; Gregory, J.; Jia, X. *Particle Deposition and Aggregation: Measurement, Modelling, and Simulation*; Butterworth-Heinemann: Oxford, England, 1995.
- Elimelech, M.; O'Melia, C. R. Effect of Particle Size on Collision Efficiency in the Deposition of Brownian Particles with Electrostatic Energy Barriers. *Langmuir* **1990**, 6 (6):1153-1163.
- Esmaeili, P. *Surface Charge Heterogeneities and the Stability of Emulsion Drops*; PhD thesis, University of Alberta, Edmonton, AB, Canada, 2009.
- Esmaeili, P.; Lin, F.; Yeung, A. Stability of Emulsified Heavy Oil: The Combined Effects of Deterministic DLVO Forces and Random Surface Charges. *Langmuir* **2012**, 28, 4948-4954.
- Evans, E. A.; Needham, D. Physical Properties of Surfactant Bilayer Membranes: Thermal Transitions, Elasticity, Rigidity, Cohesion and Colloidal Interactions, *J. Phys. Chem.* **1987**, 91, 4219-4228.
- Feick, J. D.; Chukwumah, N.; Noel, A. E.; Velegol, D. Altering Surface Charge Nonuniformity on Individual Colloidal Particles. *Langmuir* **2004**, 20 (8), 3090-3095.
- Feick, J. D.; Velegol, D. Electrophoresis of Spheroidal Particles having a Random Distribution of Zeta Potential. *Langmuir* **2000**, 16 (26), 10315-10321.
- Feick, J. D.; Velegol, D. Measurements of Charge Nonuniformity on Polystyrene Latex Particles. *Langmuir* **2002**, 18 (9), 3454-3458.

- Feick, J. D.; Velegol, D. Reducing Surface Charge Nonuniformity on Individual Particles through Annealing. *Ind. Eng. Chem. Res.* **2004**, 43, 3478-3483.
- Fleming, B. D. Wanless, E. J. Biggs, S. Non-equilibrium Mesoscale Surface Structures: The Adsorption of Polymer-Surfactant Mixture at the Solid/Liquid Interface. *Langmuir* **1999**, 15, 8719-8725.
- Frens, G.; Overbeek, J. T. G. Repeptization and the Theory of Electrostatic Colloids. *J. Colloid Interface Sci.* **1972** 38(2), 376-387.
- Fuchs, N. Theory of Coagulation. *Phys. Z.* **1934**, 171, 199-208.
- Gillespie, D. T. Exact Numerical Simulation of the Ornstein-Uhlenbeck Process and Its Integral. *Phys. Rev. E* **1996**, 54, 2084-2091.
- Grant, M. L.; Saville, D. A. Colloidal Interaction in Protein Crystal Growth. *J. Phys. Chem.* **1994**, 98, 10358-10367.
- Grant, M. L.; Saville, D. A. Electrostatic Interactions between a Nonuniformly Charged Sphere and a Charged Surface. *J. Colloid Interf. Sci.* **1995**, 171, 35-45.
- Gregory, J. Interaction of Unequal Double Layers at Constant Charge. *J. Colloid Interf. Sci.* **1975**, 51 (1), 44-51.
- Gregory, J.; Wishart, A. J. Deposition of Latex-Particles on Alumina Fibers. *Colloids and Surfaces* **1980**, 1 (3-4), 313-334.
- Gregory, J. Fundamentals of Flocculation. *Critical Reviews in Environ. Control* **1989**, 19 (3), 185-230.
- Healy, T. W.; Homola, A.; James, R. O. Coagulation of Amphoteric Latex Colloids: Reversibility and Specific Ion Effect. *Faraday Discuss Chem. Soc.* **1978**, 65, 156-163.
- Herman, M. C.; Papadopoulos, K. D. Effects of Asperities on the van der Waals and Electric Double Layer Interactions of Two Parallel Flat Plates. *J. Colloid Interf. Sci.* **1990**, 136, 385-392.
- Hiemenz, P. C.; Rajagopalan, R. *Principles of Colloid and Surface Chemistry*; Marcel Dekker: New York, 1997.
- Higashitani, K.; Tanaka, T.; Matsuno, Y. A Kinematic Interpretation on Coagulation Mechanism of Hydrophobic Colloids. *J. Colloid Interf. Sci.* **1978**, 63 (3), 551-560.
- Holt, W. J. C.; Chan, D. Y. C. Pair Interaction between Heterogeneous Spheres. *Langmuir* **1997**, 13, 1577-1686.

- Honig, E. P.; Roeberson, G. J.; Wiersema, P. H. Effect of Hydrodynamic Interaction on the Coagulation Rate of Hydrodynamic Colloids. *J. Colloid Interf. Sci.* **1971**, 36, 97-109.
- Hunter, R. J. *Foundation of Colloid Science*, Volume 1 and 2; Oxford University Press: New York, 1986.
- Hunter, R. J. *Zeta Potential in Colloid Science: Principles and Application*; Academic Press: London, 1981.
- Luczka, J.; Hanggi, P.; Gadowski, A. Non-Markovian Process Driven by Quadratic Noise Kramers-Moyal Expansion and Fokker-Planck Modeling *Phys. Rev. E* **1995**, 512933-2938.
- Israelachvili, J. N. *Intermolecular and Surface Forces*; 2<sup>nd</sup> Ed.; Academic press: London, 1992.
- Israelachvili, J. N.; Adams, G. E. Measurement of Forces between Two Mica Surfaces in Aqueous Electrolyte Solutions in the Range 1-100 nm, *J. Chem. Soc., Faraday Trans. I* **1978**, 74, 975-985.
- Israelachvili, J. N.; Pashley, R. The Hydrophobic Interaction is Long Range, Decaying Exponentially with Distance. *Nature* **1982**, 300, 341-342.
- Israelachvili, J. N.; Pashley, R. Measurement of the Hydrophobic Interaction between two Hydrophobic Surfaces in Aqueous Electrolyte Solutions. *J. Colloid Interf. Sci.* **1984**, 90, 500-514.
- Jackson, P. M.; Eastwood, K. M. Finding the Critical Numbers: What Are the Real Decline Rates for Global Oil Production? *CERA Private Report*, Sept 4, 2007.  
<http://www.cera.com/aspx/cda/client/report/reportpreview.aspx?CID=8958&KID=>.
- Jones, J. F.; Holtzer, G. L.; Snyder, C.; Yake A. M.; Velegol, D. Charge Nonuniformity Light Scattering. *Colloids Surfaces A: Physicochem. Eng. Aspects* **2005**, 267 (1), 79-85.
- Kallay, N.; Nelligan, J. D.; Matijevic, E. Particle Adhesion and Removal in Model Systems. Part 6. Kinetics of Deposition of Haematite Particles on Steel. *J. Chem. Soc., Faraday Trans. I*, **1983**, 79 (1), 65-74.
- Kasperski, K. L. *A Review of Oil Sands Aqueous Extraction Research*; Canada Centre for Mineral and Energy Technology (CANMET) Division Report, 2001
- Kostoglou, M.; Karabelas, A. J. Effect of Roughness on Energy of Repulsion between Colloidal Surfaces. *J. Colloid Interf. Sci.* **1995**, 171, 187-199.

- Kozlova, N.; Santore, M. M. Manipulation of Micrometer-Scale Adhesion by Tuning Nanometer-Scale Surface Features. *Langmuir* **2006**, 22 (3), 1135-1142.
- Kuin, A. J. Interaction Potential of a Dispersion of Colloidal Particles with a Non-homogeneous Surface Potential. *Faraday Discuss. Chem. Soc.* **1990**, 90, 235-244
- Laroche, I. *Investigating the Stability of Bitumen Droplets in Water through Force Measurements*; MSc. Thesis, University of Alberta, Edmonton, Alberta, Canada, 2000
- Lessard, R. R.; Zieminski, S. A. Bubble Coalescence and Gas Transfer in Aqueous Electrolyte Solutions. *Ind. Eng. Chem. Fund.* **1971**, 10, 260-269.
- Loeb, A. L.; Overbeek, J. T. G.; Wiersema, P. H. *The Electrical Double Layer around a Spherical Particle*; M.I.T. Press: Cambridge, Massachusetts, US, 1961.
- Litton, G. M.; Olson, T. M. Colloid Deposition Rates on Silica Bed Media and Artifacts Related to Collector Surface Preparation Methods, *Environ. Sci. Technol.* **1993**, 27 (1), 185-193.
- Liu, J.; Xu, Z.; Masliyah, J. Studies on Bitumen-Silica Interaction in Aqueous Solution by Atomic Force Microscopy. *Langmuir* **2003**, 19, 3911-3920.
- Mankowski, P.; Ng, S.; Siy, R.; Spence, J.; Staleton, P. *Syncrude's Low Energy Extraction Process: Commercial Implementation*; Syncrude Research Report: Edmonton, Canada 1996.
- Marinova, K. G.; Alargova, R. G.; Denkov, N. D. Charging of Oil-Water Interfaces due to Spontaneous Adsorption of Hydroxyl Ions. *Langmuir* **1996**, 12, 2045-2051.
- Masliyah, J. *Course Notes – CHE534 Fundamentals of Oilsands Extraction*; University of Alberta, Edmonton, Canada, winter 2007.
- Masliyah, J. H.; Bhattacharjee, S. *Electrokinetic and Colloid Transport Phenomena*; Wiley-Interscience: Hoboken, N. J., 2006.
- Masliyah, J.; Zhou, Z.; Xu, Z.; Czarnecki, J. Hamza, H. Understanding Water-Based Bitumen Extraction from Athabasca Oil Sands. *Can. J. Chem. Eng.* **2004**, 82, 628-654.
- McCull, D. *The Eye of the Beholder: Oil Sands Calamity or Golden Opportunity?* Canadian Energy Research Institute (CERI) Oil Sands Briefing, 2009.  
<http://www.ceri.ca/Publications/documents/CERIOilSandsBriefingFebruary2009.pdf>.
- Miklavic, S. J. Double Layer Forces between Heterogeneous Charged Surfaces: the Effect of Net Surface Charge. *J. Phys. Chem.* **1995**, 103, 4794-4806.

- Miklavic, S. J.; Chan, D. Y. C.; White, L. R.; Healy, T. W. Double Layer Forces between Heterogeneous Charged Surfaces. *J. Phys. Chem.* **1994**, 98, 9022-9032.
- Moran, K.; Yeung, A.; Czarnecki, J.; Masliyah, J. Micro-scale Tensiometry for Studying Density-Matched and Highly Viscous Fluids with Application to Bitumen-in-Water Emulsions. *Colloids Surf. A: Physicochem. Eng. Aspects* **2000a**, 174, 147-157.
- Moran, K.; Yeung, A.; Masliyah, J. Factors Affecting the Aeration of Small Bitumen Droplets. *Can. J. Chem. Eng.* **2000b**, 78, 625-634.
- Napper, D. H. Flocculation of Sterically Stabilized Dispersions. *J. Colloid Interf. Sci.* **1970**, 32, 106-114.
- O'Donnell, S. *Syncrude Pleads not Guilty in Dead Ducks Case*; Edmonton Journal, Sept 14, 2009.  
<http://www.calgaryherald.com/business/Syncrudepleadsguiltydeadducks/1992697/story>.
- Ornstein, L. S.; Uhlenbeck, G. E. On the Theory of the Brownian Motion. *Phys. Rev.* **1930**, 36, 823-841.
- Ottewill, R. H.; Walker, T. Influence of Particle Size on the Stability of Polystyrene Latexes with an Adsorbed Layer of Nonionic Surface Active Agent. *J. Chem. Soc. Faraday Trans.* **1974**, 70 (1), 917-926.
- Pashley, R. M. The Effects of Hydrated Cation Adsorption on Surface Forces between Mica Crystals and its Relevance to Colloidal Systems. *Chem. Scripta* **1985**, 25, 22-27.
- Pashley, R. M.; Israelachvili, J. N. DLVO and Hydration Forces between Mica Surfaces in  $Mg^{2+}$ ,  $Ca^{2+}$ ,  $Sr^{2+}$ , and  $Ba^{2+}$  Chloride Solutions. *J. Colloid Interf. Sci.* **1984**, 97, 446-455.
- Penners, N. H. G.; Koopal, L. K. The Effect of Particle Size on the Stability of Haematite ( $\alpha-Fe_2O_3$ ) Hydrosols. *Colloids Surf. A.* **1987**, 28, 67-83.
- Prieve, D. C.; Lin, M. M. J. The Effect of a Distribution in Surface Properties on Colloid Stability. *J. Colloid Interf. Sci.* **1982**, 86 (1), 17-25.
- Radler, M. Worldwide Reverses Increase as Production Holds Steady. *Oil & Gas Journal*, **2002**, 100, 113-145.
- Reerink, H.; Overbeek, J. T. G. The Rate of Coagulation as a Measure of the Stability of Silver Iodide Sols. *Discuss. Faraday Soc.* **1954**, 18, 74-84.
- Richmond, P. Electrical Forces between Particles with Arbitrary Fixed Surface Charge Distributions in Ionic Solution. *J. Chem. Soc., Faraday Trans. II.* **1974**, 70, 1066-1073.

- Richmond, P. Electrical Forces between Particles with Discrete Periodic Surface Charge Distributions in Ionic Solution. *J. Chem. Soc., Faraday Trans. II.* **1975**, 71, 1154-1162.
- Rodriguez-Valverde, M. A.; Cabrerizo-Vilchez, M. A. Paez-Duenas, A.; Hidalgo-Alvarez, R. Stability of Highly Charged Particles: Bitumen-in-Water Dispersions. *Colloids Surf. A: Physicochem. Eng. Aspects* **2003**, 222, 233-251.
- Rotsh, C.; Radmacher, M. Mapping Local Electrostatic Forces with the Atomic Force Microscope. *Langmuir* **1997**, 13, 2825-2832.
- Salou, M.; Siffert, B.; Jada, A. Study of the Stability of Bitumen Emulsions by Application of DLVO Theory. *Colloids Surf. A: Physicochem. Eng. Aspects* **1998**, 142, 9-16.
- Sanders, R. S.; Chow, R. S.; Masliyah, J. H. Deposition of Bitumen and Asphaltene-Stabilized Emulsions in an Impinging Jet Cell. *J. Colloid Interf. Sci.* **1995**, 174, 230-245.
- Sanders, R. S.; Chow, R. S.; Masliyah, J. H. Hydrophobic Interactions in Silane-Treated Silica Suspensions and Bitumen Emulsions. *Can. J. Chem. Eng.* **2003**, 81, 43-52.
- Santore, M. M.; Kozlova, N. Micrometer Scale Adhesion on Nanometer-Scale Patchy Surfaces: Adhesion Rates, Adhesion Thresholds, and Curvature-Based Selectivity. *Langmuir* **2007**, 23, 4782-4791.
- Shaw, D. J. *Introduction to Colloid and Surface Chemistry*; 3<sup>rd</sup> Ed.; Butterworths: London, 1980.
- Shaw, R. C.; Schramm, L. L.; Czarnecki, J. *Suspension: Fundamentals and Application in the Petroleum Industry, Advances in Chemistry* (Schramm, L. L. Edition); American Chemical Society: Washington DC, 1996.
- Shulepov, S. Y.; Frens, G. Surface Roughness and the Particle Size Effect on the Rate of Slow, Perikinetic Coagulation. *J. Colloid Interf. Sci.* **1995**, 170, 44-49.
- Song, L.; Johnson, P. R.; Elimelech, M. Kinetics of Colloid Deposition onto Heterogeneously Charged Surfaces in Porous Media. *Environ. Sci. Technol.* **1994**, 28 (6), 1164-1171.
- Song, S.; Lopez-Valdivieso, A.; Reyes-Bahena, J.L.; Bermejo-Perez, H.I.; Trass, O. Hydrophobic Flocculation of Galena Fines in Aqueous Suspensions. *J. Colloid Interf. Sci.* **2000**, 227, 272-281.
- Sparnaay, M. J. *The Electrical Double Layer*; Pergamon, 1972.

- Sparnaay, M. J. Four Notes on van der Waals Forces: Induction Effect, Nonadditivity, Attraction between a Cone and a Flat Plate (Asperities), History. *J. Colloid Interf. Sci.* **1983**, 91, 307-319.
- Speight, J. G. *The Chemistry and Technology of Petroleum*, 2<sup>nd</sup> Ed.; New York, 1991.
- Spence, J.; Siy, R.; Sury, K.; McDowell, K.; Ng, S. *Aurora Extraction Process: 1995 OSLO Cold Water Extraction Research Pilot Test Program*, Syncrude Research Report 96-3, June 1996.
- Spielman, L. A. Viscous Interaction in Brownian Coagulation. *J. Colloid Interf. Sci.* **1970**, 33, 562-571.
- Suresh, L.; Walz, J. Y. Direct Measurement of the Effect of Surface Roughness on the Colloidal Forces between a Particles and Flat Plate. *J. Colloid Interf. Sci.* **1997**, 196, 177-190.
- Suresh, L.; Walz, J. Y. Effect of Surface Roughness on the Interaction Energy between a Colloidal Sphere and a Flat Plate. *J. Colloid Interf. Sci.* **1996**, 183, 199-213.
- Tabor, D.; Winterton, R. M. Direct Measurements of Normal and Retarded van der Waals Force. *Proc. Roy. Soc. Lond. A.* **1969**, 312, 435-450.
- Takamura, K.; Chow, R. S. The Electric Properties of the Bitumen/Water Interface Part II. Application of the Ionizable Surface-Group Model. *Colloids Surf.* **1985**, 15, 35-48.
- Tan, S.; Sherman, R. L.; Qin, D.; Ford, W. T. Surface Heterogeneity of Polystyrene Latex Particles Determined by Dynamic Force Microscopy. *Langmuir* **2005**, 21, 43-49.
- Thwar, P. K.; Velegol, D. Force Measurements between Weakly Attractive Polystyrene Particles. *Langmuir* **2002**, 18, 7328-7333.
- Tipman, R.; Shaw, R. C. Recent Advances in the Treatment of Oil Sands Froth, Presented at AOSTRA 2000, Edmonton, 1993.
- Vanderklippe, N. *Oil Sands Layoffs Coming Down Pipeline*; Globe and Mail, Jan 23, 2009.
- Vaidyanathan, R.; Tien, C. Hydrosol Deposition in Granular Media under Unfavorable Surface Conditions. *Chem. Eng. Sci.* **1991**, 46 (4), 967-983.
- Van Bree, J. L. M. M.; Poulis, J. A.; Verhaar, B. J.; Schram, K. The Influence of Surface Irregularities upon the van der Waals Forces between Macroscopic Bodies. *Physica* **1974**, 78, 187-190.

- Van De Ven, T. G. M.; Mason, S. G. The Microrheology of Colloidal Dispersions IV. Pairs of Interacting Spheres in Shear Flow. *J. Colloid Interf. Sci.* **1976**, 57 (3), 505—516.
- Van Oss, C.J. *Interfacial Forces in Aqueous Media*; 2<sup>nd</sup> Ed.; CRC Press: Boca Raton, 2006.
- Velegol, D.; Anderson, J. L. Determining the Forces between Polystyrene Latex Spheres Using Different Electrophoresis. *Langmuir* **1996**, 12, 4103-4110.
- Velegol, D.; Feick, J. D. Evaluating Randomness of Charge Distribution on Colloidal Particles Using Stationary Electrophoresis Angles. *Langmuir* **2003**, 19, 4592-4596.
- Velegol, D.; Feick, J. D.; Collins, L. R. Electrophoresis of Spherical Particles with a Random Distribution of Zeta Potential or Surface Charge. *J. Colloid Interf. Sci.* **2000**, 230, 114-121.
- Verwey, E. J. W.; Overbeek, J.T. G. *Theory of the Stability of Lyophobic Colloids*; Elsevier: Amsterdam, 1948.
- Von Smoluchowski, M. Outline of the Coagulation Kinetics of Colloidal Solutions. *Colloid Z.* **1917**, 21 (3), 98-104.
- Von Smoluchowski, M. Experiments on a Mathematical Theory of Kinetic Coagulation of Colloid Solutions. *Phys. Chem.* **1917**, 92 (2), 129-168.
- Vreeker, R.; Kuin, A. J. Den Boer, D. C.; Hoekstra, L. L.; Agterof, W. G. M. Stability of Colloidal Particles with a Nonhomogeneous Surface Potential: Application to Colloidal Nickel Hydroxy Carbonate. *J. Colloid Interf. Sci.* **1992**, 154 (1), 138-145.
- Waltermo, A.; Claesson, P. M.; Simonsson, S. Manev, E.; Johansson, I.; Bergeron V. Foam and Thin-Liquid-Film Studies of Alkyl Glucoside Systems. *Langmuir* **1996**, 12, 5271-5278.
- Walz, J. Y. The Effect of Surface Heterogeneities on Colloidal Forces. *Adv. Colloid Interf. Sci.* **1998**, 74, 119-168.
- Wu, X.; Czarnecki, J.; Hamza, N.; Mashliyah, J. Interaction Forces between Bitumen Droplets in Water. *Langmuir* **1999a**, 15, 5244-5250.
- Wu, X.; Dabro, T.; Czarnecki, J. Determining the Colloidal Forces between Bitumen Droplets in Water Using Hydrodynamic Force Balance Technique. *Langmuir* **1999b**, 15, 8706-8713.
- Yergin, D.; Hobbs, D.; Buckhard, J.; et al. *Growth in the Canadian Oil Sands: Finding the New Balance*; an IHS Cambridge Energy Research Associates Special (CERA) Report, Jul 15, 2009.

<http://www.cera.com/asp/cda/client/knowledgearea/servicedescription.aspx?kid=228>.

Yeung, A.; Dabros, T.; Czarnecki, J.; Masliyah, J. On the Interfacial Properties of Micrometer-Sized Water Droplets in Crude Oil. *Proc. Royal Soc. A.* **1999**, 455, 3709-3723.

Yeung, A.; Moran, K.; Masliyah, J.; Czarnecki, J. Shear-Induced Coalescence of Emulsified Oil Drops. *J. Colloid Interf. Sci.* **2003**, 265, 439-443.

Yin, X.; Drelich, J. Surface Charge Microscopy: Novel Technique for Mapping Charge-Mosaic Surfaces in Electrolyte Solutions. *Langmuir* **2008**, 24, 8013-8020.

Yoon, R. H.; Askoy, B. S. Hydrophobic Forces in Thin-Water Film Stabilized by Dodecylammonium Chloride. *J. Colloid Interf. Sci.* **1999**, 211, 1-10.

Yoon, R. H.; Guzonas, D. A.; Aksoy, B. S. Czarnecki, J.; Yeung, A. *Role of Surface Forces in Tar Sand Processing*, in "Processing of Hydrophobic Minerals and Fine Coals: Proceedings of the 1<sup>st</sup> UBC-McGill Bi-Annual International Symposium on Fundamentals of Mineral Processing" (Laskowski, J. S. and Poling, G. W. Edition), Canadian Inst. Mining Metallurgy and Petroleum, Vancouver, BC, 1995.

## **Appendix A: Contact mechanics of two distinctly-sized droplets pressed together in oblique contact experiments.**

Knowing the droplet-droplet interaction area is critical for our theoretical predication. It is known that bitumen is a deformable and highly viscous material. When dealing such bitumen-water interface, deformation is a concern; the degree of surface deformation depends on the size of droplet and the compressive force on the geometry. Though a model invoking Young-Laplace equation used in the previous study [Esmaeili 2009] could describe the droplet contact mechanics, the application of this model remains rather based on a few special assumptions. In this study, instead of two similarly-sized drops, a small drop is compressed against much larger droplet. Since a smaller drop is less deformable than a large one<sup>§§§</sup>, we assume that during oblique contact process (up to the moment of coalescence, if it occurs), the small drop behaves like a rigid body and maintains its shape profile as originally spherical cap; however, the much bigger drop acts as a relatively soft flatted plane and deforms to any appreciable extent, as shown in Figure A-1; the similar treatment was performed by Basheva et al. [1999], who made rigorous hydrodynamic calculations when the emulsified droplets were pressed against a much larger interface. According to this assumption, surface area of oblique contact  $AC$  is estimated as the total area of a spherical cap traveling along the certain distance in the following:

$$AC \approx 2\pi r^2 \left(1 + \sqrt{1 - \left(\frac{r_p}{r}\right)^2} - \frac{2}{DR}\right) + 2rH \cos^{-1} \left( \frac{2}{DR} - \sqrt{1 - \left(\frac{r_p}{r}\right)^2} \right) \quad (\text{A.1})$$

---

<sup>§§§</sup> This is explained by the Laplace equation:  $\Delta p \approx \frac{2\gamma_{BW}}{R}$ ,

Here,  $\Delta p$  is compressive pressure;  $\gamma_{BW}$  is the interfacial tension of bitumen-in-water;  $R$  the radius of an undeformed droplet.

Here  $r$  is the radius of un-deformed small droplet;  $r_p$  is radius of the suction pipette;  $DR$  is the deformation ratio, rather being called as aspect ratio, of small drop equated to the ratio of major axis over minor axis (i.e.  $2a/2b$ ) which is totally immersed in the aqueous medium (here  $a = r$ );  $H$  the distance of oblique shear contact. To ensure that this estimation did not contribute to big errors in the contact area analysis, the deformation ratio ( $DR$ ) was kept sufficiently low. The case of  $DR = 1.1$  could be considered negligible, as confirmed by the experiment that not much noticeable aspect distortion of the small bitumen drop was visually observed from its spherical shape right after departure from contact under this ratio if coalescence did not happen (refers to the right column of Figure 4-4 for evidence).

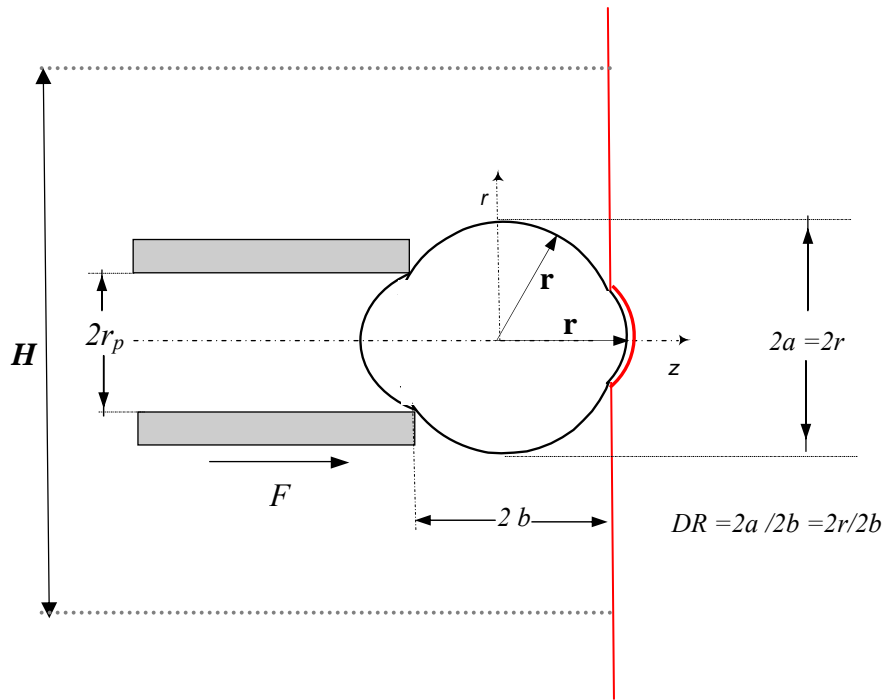


**Figure A-1: Depiction of the droplet shape profile in this study.** A spherical drop (representing a small drop), held by a suction pipette, is brought against a planar surface in red (modeling a much bigger drop).

## Appendix B: AFM force analysis

The raw data of an AFM force measurement is in the relation of photodiode current  $I_{\text{PSD}}$  (mV) versus piezo displacement  $Z_p$  (nm). To obtain a force-vs-distance curve,  $I_{\text{PSD}}$  and  $Z_p$  have to be converted in force  $F$  and distance  $h$ . In the sample preparation of this study, the very thin bitumen layer was spin-coated on the silicone wafer as outlined in Section 3.3.2. In this way, the deformation of bitumen was greatly minimized and can be treated to be negligible. In addition, long ranged repulsive forces were expected in the current study conditions. Therefore, based on the principle of force analysis [Butt et al. 2003], we will declare the conversion procedure of a force curve step by step for the simplified situation as shown in Figure B-1.

### (1) Virtual deflection calibration.

The virtual deflection is a showcase of very slight slope in the force curve far away separation distance (see Figure B-1a), which arises from the mechanical path not being quite perfect. Note that this virtual deflection may be of order 0.1 nm or even less over a hundred of nanometers. However, the virtual deflection calibration would make curve analysis easier; this is done by leveling off the non-contact part of the curve, as shown in Figure B-1b.

### (2) Zero force assumption.

The horizontal line of the non-contact part far away from separation is defined as zero force, implying negligible surface force. Hereafter, we subtract this linear function from the measured raw AFM data and obtain a horizontal line of zero over the non-contact part, depicted as Figure B-1c.

(3) Contact regime and zero distance assumptions.

It is easy to distinguish the linear part of the “contact regime”, where  $I_{\text{PSD}}$  is linear with respect to  $Z_p$  (shown as the solid line in Figure B-1c). Over this contact regime, the separation between the tip and substrate is assumed to be zero distance and the slope of this linear line is defined as the deflection sensitivity  $\Delta I_{\text{PSD}}/\Delta Z_p$ . After these assumptions, the deflection of cantilever  $Z_c$  is obtained by dividing the photodiode signal by the deflection sensitivity:  $Z_c = I_{\text{PSD}} / (\Delta I_{\text{PSD}}/\Delta Z_p)$ , the curve of deflection versus piezo displacement is illustrated in Figure B-1d. The separation distance  $h$  between the tip and the substrate is the addition of cantilever deflection and piezo position:  $h = Z_c + Z_p$ . Here,  $Z_p$  is defined as zero at the point where two linear parts of the raw curve are extrapolated to intercross, as indicated in the arrow point of Figure B-1d.

(4) Force vs distance curve.

The long range force  $F$  against the tip-substrate distance  $h$  is easily calculated by multiplying the cantilever deflection due to the colloidal forces (as declared in Figure B1-e) by the known spring constant  $k_c$  of cantilever:  $F = k_c Z_c$ , which leads to the final force profile in Figure B1-f.

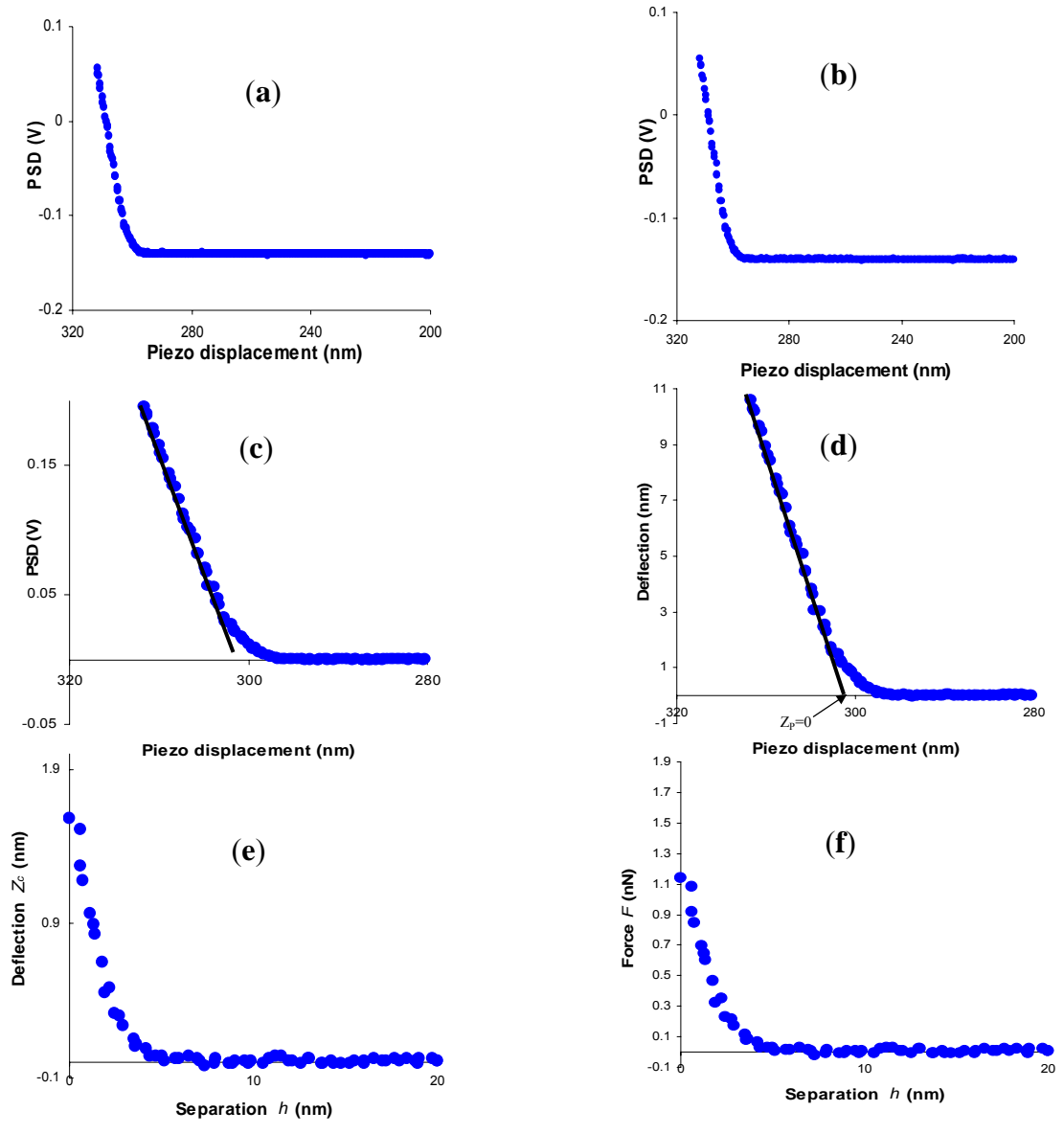


**Figure B-1: Schematic of graphs showing the conversion procedure of a force curve obtained by AFM**

## **Appendix C: Theoretical equations of DLVO forces between the AFM tip and the bitumen substrate in a SPW electrolyte**

The silicone nitride cantilever tip used in the above AFM experiments was pyramid-shaped, which can be reasonably approximated as two parts: a conical region and a spherical cap at its apex. Figure C-1 schematizes the geometry of the system in which this type of tip interacts with the flat sample substrate. The theoretical equations describing DLVO forces (van der Waals plus electrostatic double layer forces) for this geometry were derived by Drelich et al. [2007] who used Derjaguin approximation [Hunter 1986]. Only the final equations with the two boundary conditions (*BC*) of constant potential (*CP*) and constant charge (*CC*) are rearranged here, together with the estimated values of the relevant parameters which were applied for the concerned interactions between the tip and the bitumen in the SPW electrolytes.

*BC-1: Constant potential (CP).*

$$F_T(h) = \{2\pi\varepsilon [2a_1\psi_i\psi_s \exp(-\kappa h) - a_2(\psi_i^2 + \psi_s^2) \exp(-2\kappa h)]\} + \left\{-\frac{A_{123}}{6} \left(\frac{r_s + h}{l_1^2} + \frac{r_s - h}{h^2}\right)\right\} \quad (\text{C.1})$$

*BC-2: Constant charge (CC).*

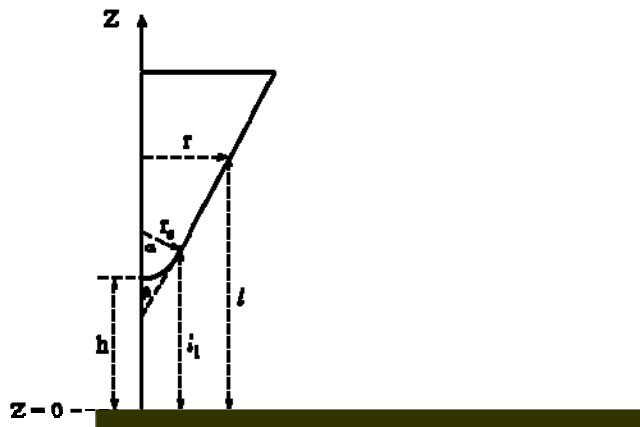
$$F_T(h) = \left\{\frac{2\pi}{\varepsilon\kappa^2} [2a_1\delta_i\delta_s \exp(-\kappa h) - a_2(\delta_i^2 + \delta_s^2) \exp(-2\kappa h)]\right\} + \left\{-\frac{A_{123}}{6} \left(\frac{r_s + h}{l_1^2} + \frac{r_s - h}{h^2}\right)\right\} \quad (\text{C.2})$$

In the above either equation,  $F_T(h)$  is the total DLVO forces, the summation of electrostatic force in the first {...} of the right-handed side and van der Waals force in the second {...} of the right-handed side. In addition,  $l_1 = h + r_s(1 - \cos \alpha)$ ,  $a_1 = r_s\kappa - 1$ ,  $a_2 = r_s\kappa - 0.5$ . Where,  $h$  is the separation distance between the end of the cantilever tip and the bitumen substrate;  $r_s$  is the radius of the spherical cap at the tip end, ~10 nm given by the

manufacturer;  $\alpha$  and  $\beta$  are the geometrical angles for the spherical cap and the conical region with  $\alpha+\beta = 90^\circ$  and  $\beta \sim 10^\circ$  and  $20^\circ$  \*\*\*\* respectively for the tip with a nominal spring constant of 0.12 N/m and that of 0.58 N/m;  $\kappa$  is the inverse Debye length,  $\kappa^{-1} \sim 1.45$  nm;  $\epsilon$  is the permittivity of the SPW electrolyte,  $\sim 6.9415 \times 10^{-10}$  C/(V·m).  $A_{123}$  is the Hamaker constant,  $\sim 2.7 \times 10^{-20}$  J for the system of  $\text{Si}_3\text{N}_4$ -water- bitumen [Drelich et al. 2007].  $\Psi_s$  and  $\Psi_t$  ( $\delta_s$  and  $\delta_t$ ) are the surface potentials (surface charge densities) for the bitumen and the tip respectively. Note that surface potential ( $\Psi$ ) and charge density ( $\delta$ ) in an electrolyte are related with the Grahame equation [Butt et al. 2003]:

$$\delta = \sqrt{8 \epsilon n^0 k_B T} \sinh \left( \frac{ze \psi}{2 k_B T} \right) \quad (\text{C.3})$$

Here,  $z$ , ionic valence, is equivalent to 1 (neglecting the concentration of divalent ions in this study);  $n^0$ , denoting the ionic concentration in the bulk solution, is  $\sim 2.4 \times 10^{25}$  /m<sup>3</sup> (neglecting the concentration of pH-determining ions);  $e$ , elementary charge,  $\sim 1.6 \times 10^{-19}$  C;  $k_B T$ , the thermal energy, is  $4.17 \times 10^{-21}$  J at room temperature;  $\epsilon$  is the permittivity of the SPW electrolyte,  $\sim 6.9415 \times 10^{-10}$  C/(V·m).



**The parameters used in theoretical model:**  $\alpha$  and  $\beta$  are the geometrical angles for the spherical cap and the conical region with  $\alpha+\beta = 90^\circ$ ;  $r_s$  is the radius of the spherical cap at the tip end;  $r$  is the radius of the circle of the tip at given vertical position;  $h$  is the distance between the end of the tip and the substrate;  $l_1$  is the distance between the point connecting cap with cone and the substrate;  $l$  is the distance between a different surface section of the tip and the substrate.

**Figure C-1: Geometry of the system where the cantilever tip interacts with the flat substrate.**

\*\*\*\* The two values are estimated to be in the range of data given by the manufacturer.

## Appendix D: Note on the Ornstein-Uhlenbeck Process

In this short note, we briefly discuss some facts of the most popular Ornstein-Uhlenbeck (OU) process, which is known as a Gaussian random process with exponential correlation function. The OU process plays a very significant role in physics. Historically, this process was critical in mathematically describing the Brownian motion [Ornstein & Uhlenbeck 1930]. Recently, it has been adopted by many researchers to simulate the “colored noise” [Luczka et al. 1995; Castro et al. 1995] and to estimate the mean-reverting process which fluctuates around a ‘stable state’ [Gillespie 1996]. Generally speaking, the OU process,  $y(x)$ , which evolves with a real variable  $x$  (location displacement or time), at discrete variable interval  $\Delta x$  (distance steps of interval or time steps of width), can be expressed according to the following equation:

$$y(x + \Delta x) = y(x) + \frac{1}{\lambda}(y_{ave} - y(x))\Delta x + \sigma dW_x \quad (D.1)$$

In this equation,  $y_{ave}$ ,  $\sigma$ , and  $\lambda$  are the mean value, standard deviation, and correlation constant (length or time) of the process;  $W_x$  is a Brownian motion (Gaussian white noise), so  $dW_x$  is a completely uncorrelated normal random variable with zero mean and variance  $\Delta x$ .

It should be paid attention that the equation (D.1) is only sound on the condition that the discrete  $\Delta x$  is adequately small [Gillespie 1996]. The exact formula which applies for any size of interval  $\Delta x$  is

$$y(x + \Delta x) = e^{-\Delta x / \lambda} y(x) + (1 - e^{-\Delta x / \lambda}) y_{ave} + \sigma \sqrt{\frac{\lambda}{2} (1 - e^{-\Delta x / \lambda})} dW_x \quad (D.2)$$